FABIO TINAZZI

SMART AND EFFICIENT ELECTRIC DRIVES FOR MECHATRONIC APPLICATIONS

Fabio Tinazzi:
Smart and efficient electric drives for mechatronic applications ,

SUPERVISOR:
Mauro Zigliotto

LOCATION:
Vicenza

TIME FRAME:
February 2016

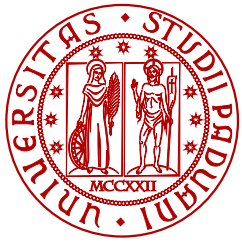

UNIVERSITÀ
DEGLI STUDI
DI PADOVA

Sede amministrativa: Università degli Studi di Padova

Dipartimento di Tecnica e Gestione dei Sistemi Industriali

SCUOLA DI DOTTORATO IN INGEGNERIA MECCATRONICA
E DELL'INNOVAZIONE MECCANICA DEL PRODOTTO

CICLO XXVIII

SMART AND EFFICIENT ELECTRIC DRIVES FOR MECHATRONIC APPLICATIONS

Direttore della scuola: Ch.mo Prof. Alessandro Persona

Supervisore: Ch.mo Prof. Mauro Zigliotto

Dottorando: Fabio Tinazzi

Ai miei nonni Gioconda e Bruna, Guglielmo e Costante

ABSTRACT

The call for the reduction of energy consumption has manifolds reflections on the mechatronics applications. Electric motors represent one of the biggest electric energy consumers in the world, due to their wide utilisation both in industrial and domestic applications. There is, in turn, a need of more efficient drives that implement energy efficient control techniques for all kind of electric motors. The mechanical sensor for the rotor position represents both an additional cost and a source of faults, although the position information is crucial for energy efficient controls. The removal of the position sensor is acceptable provided that a precise position information is still guaranteed, for instance by a position estimator.

The research presented in this thesis concerns the development of a complete drive from the control point of view. Advanced control methodologies were considered together with new and specifically designed equipments for improving the overall performances of synchronous permanent magnet motor drives. Efficiency and applicability on mechatronics systems are the main targets of this work. The development of a complete sensorless drive for synchronous permanent magnet motors was the goal chosen to hit the latter targets. Sensorless drives, i.e. without the mechanical position sensors, increases the reliability of the drive, meanwhile reducing costs. In order to guarantee efficiency, advanced control for the minimisation of losses are implemented, though they strongly rely on the rotor position information. Great accuracy, i.e. small errors, must be guaranteed by the sensorless algorithm, which is determined by the following elements: accuracy of the electrical quantities measurements, knowledge of the motor parameters and stability of the sensorless drive. Three chapter of this thesis cope with the latter three crucial elements.

While current measurements are reliable and with almost no implementation issues, voltage measurements are quite difficult to deal with. Usually, voltage references are used, provided that a proper compensation of the inverter non idealities is implemented. This thesis discusses the development and use of a new equipment for measuring the output voltage. The latter equipment was used to develop both more precise parameter estimation techniques and new sensorless algorithms. A new inverter non idealities identification was developed, too, for applications where no additional equipments are desired.

The development of precise motor models has to cope with the difficulties on gathering significant informations. The improvement of the voltage acquisition increases the reliability on the obtained

results. Additional informations are obtained by taking advantage of the mathematical description of the maximum torque-per-ampere MTPA control algorithm, which is widely used in synchronous permanent magnet motor applications. The latter algorithm can be obtained regardless of the motor parameter knowledge. In this thesis, a new method to obtain a parameter estimation of the motor is presented based on the MTPA informations.

Finally, motors with different rotor structures, and thus with different parameter-to-current relationship, are considered for the robust design of sensorless algorithm . In certain cases, the motor observer is unstable due to particular rotor configurations combined with severe working conditions. An analytical study was carried out to describe such conditions and remedies are proposed in the second part of this work. The last chapter presents also the benefits deriving from the voltage measurement system. The latter benefits are quite considerable in all regions of work, which justify the additional costs of the equipment.

This thesis was typeset adopting the typographical *classichthesis* style developed by André Miede

SOMMARIO

Il problema del consumo energetico ha molteplici riflessi sulle applicazioni meccatroniche ed in particolare sui motori elettrici. Quest'ultimi infatti rappresentano i maggiori consumatori di energia elettrica nel mondo, a causa del loro utilizzo sia in ambito industriale che domestico. É necessario quindi che gli azionamenti elettrici utilizzino delle tecniche di controllo avanzate che consentano un risparmio di energia elettrica. Il sensore meccanico di posizione rappresenta sia un costo addizionale che una possibile fonte di guasto, ma è tuttavia necessario poichè la posizione del rotore è indispensabile per il controllo del motore. Azionamenti privi di tale sensore, chiamati *sensorless*, devono perciò garantire una elevata stima della posizione.

Il lavoro presentato in questa tesi riguarda lo sviluppo di un azionamento sensorless completo. Durante questo lavoro sono state applicate metodologie di controllo avanzate, congiuntamente allo sviluppo di nuove attrezzature elettroniche per migliorare l'efficienza del controllo di motori sincroni a magneti permanenti. In particolare, l'efficienza energetica e l'applicabilità ad applicazioni meccatroniche sono elementi chiave per lo studio compiuto in questo lavoro. Lo sviluppo di azionamenti sensorless va affiancato all'utilizzo di tecniche di controllo che minimizzino le perdite elettriche, le quali si basano sulla conoscenza precisa della posizione. La precisione degli algoritmi sensorless dipende pesantemente dall'accuratezza delle misure delle quantità elettriche così come dalla precisione della conoscenza dei parametri del motore. Tre capitoli verranno dedicati a questi aspetti.

La misura delle correnti è universalmente implementata negli azionamenti elettrici e non è generalmente causa di problemi. Ciò non può essere detto per quel che riguarda la misura delle tensioni. Solitamente, si utilizzano i riferimenti di tensione in uscita dal controllo di corrente. Questi riferimenti vengono adeguatamente compensati per tener conto delle non idealità dell'inverter. In questa tesi, una nuova tecnica per l'identificazione delle non idealità dell'inverter viene proposta per ovviare al problema. Tuttavia, un nuovo sistema fisico di misura delle tensioni è stato sviluppato per applicazioni che richiedono elevate prestazioni per gli azionamenti sensorless. Lo stesso sistema si è rivelato molto utile anche nello sviluppo di più raffinate tecniche di stima parametrica.

La misura delle tensioni consente di avere segnali di tensione più accurati. Utilizzando inoltre le informazioni addizionali che si possono ottenere quando il motore è controllato con particolari tecniche di controllo come quella che massimizza il rapporto coppia su corrente (MTPA), è possibile ricavare nuove tecniche di stima dei para-

metri del motore. Le tecniche di controllo MTPA basate sull'iniezioni di segnali non richiedono la conoscenza dei parametri del motore, ma la condizione di lavoro è descritta da una ben precisa formulazione matematica che è funzione dei parametri stessi. Tali informazioni, dunque, possono essere intelligentemente utilizzate per ricavare una stima dei parametri.

Infine, la progettazione di azionamenti sensorless dipende anche dalla tipologia di motore a magneti permanenti utilizzato. L'osservatore della posizione elettromeccanica risulta instabile in alcune condizioni operative. Tali condizioni verranno analizzate e descritte mediante uno studio analitico completo del problema che consentirà di delineare le linee guida per un progetto di un azionamento sensorless robusto, basato anche sui parametri stimati con le tecniche sviluppate in questa tesi. Verrà inoltre evidenziato come il sistema di misura delle tensioni sviluppato porti effettivi benefici in termini di prestazioni dell'algoritmo sensorless.

PUBLICATIONS

[1] R. Antonello, F. Tinazzi, and M. Zigliotto. "Benefits of Direct Phase Voltage Measurement in the Rotor Initial Position Detection for Permanent-Magnet Motor Drives." In: *Industrial Electronics, IEEE Transactions on* 62.11 (Nov. 2015), pp. 6719–6726. ISSN: 0278-0046. DOI: 10.1109/TIE.2015.2448514.

[2] M. Carraro, F. Tinazzi, and M. Zigliotto. "A novel approach to torque estimation in IPM synchronous motor drives." In: *IECON 2012 - 38th Annual Conference on IEEE Industrial Electronics Society*. Oct. 2012, pp. 4637–4641. DOI: 10.1109/IECON.2012.6389499.

[3] M. Carraro, F. Tinazzi, and M. Zigliotto. "Estimation of the direct-axis inductance in PM synchronous motor drives at standstill." In: *Industrial Technology (ICIT), 2013 IEEE International Conference on*. Feb. 2013, pp. 313–318. DOI: 10.1109/ICIT.2013.6505691.

[4] A. Gaeta et al. "Advanced self-commissioning and feed-forward compensation of inverter non-linearities." In: *Industrial Technology (ICIT), 2015 IEEE International Conference on*. Mar. 2015, pp. 610–616. DOI: 10.1109/ICIT.2015.7125067.

[5] F. Tinazzi and M. Zigliotto. "Torque Estimation in High-Efficency IPM Synchronous Motor Drives." In: *Energy Conversion, IEEE Transactions on* 30.3 (Sept. 2015), pp. 983–990. ISSN: 0885-8969. DOI: 10.1109/TEC.2015.2408214.

"Non ti crucciare, don Camillo" sussurrò il Cristo. "Lo so che il vedere uomini che lasciano deperire la grazia di Dio è per te peccato mortale perché sai che sono sceso da cavallo per raccogliere una briciola di pane. Ma bisogna perdonarli perché non lo fanno per offendere Dio. Essi cercano affannosamente la giustizia in terra perché non hanno più fede nella giustizia divina, e ricercano affannosamente i beni della terra perché non hanno fede nella ricompensa divina. E perciò credono soltanto a quello che si tocca e si vede, e le macchine volanti sono per essi gli angeli infernali di questo inferno terrestre che essi tentano invano di fare diventare un Paradiso. E' la troppa cultura che porta all'ignoranza perché, se la cultura non è sorretta dalla fede, a un certo punto l'uomo vede soltanto la matematica delle cose e l'armonia di questa matematica diventa il suo Dio, e dimentica che è Dio che ha creato questa matematica e questa armonia. Ma il tuo Dio non è fatto di numeri, don Camillo, e nel cielo del tuo Paradiso volano gli angeli del bene. Il progresso fa diventare sempre più piccolo il mondo per gli uomini: un giorno quando le macchine correranno a cento miglia al minuto, il mondo sembrerà agli uomini microscopico e allora l'uomo si troverà come un passero sul pomolo di un altissimo pennone e si affaccerà sull'infinito e nell'infinito ritroverà Dio e la fede nella vera vita. E odierà le macchine che hanno ridotto il mondo a una manciata di numeri e le distruggerà con le sue stesse mani. Ma ci vorrà del tempo ancora, don Camillo. Quindi rassicurati: la tua bicicletta e il tuo motorino non corrono per ora nessun pericolo". Il Cristo sorrise e don Camillo lo ringraziò di averlo messo al mondo.

— Tutto don Camillo, volume primo, Giovannino Guareschi

"It is our choices, Harry, that show what we truly are"

— Albus Dumbledore in *Harry Potter and the chamber of secrets*, J.K. Rowling

ACKNOWLEDGMENTS

Thanks to God, whom has given me my family: they are my corner stone! I thank Him for the gift of Benedetta: she means the world to me and brought the sun in my days.

Thanks to prof. Zigliotto, who has guided me during the last years with wisdom and patience. Thanks also to Alberto Gaeta and prof. Pericle Zanchetta for their kindness and help during my stay at Nottingham. A special thank goes to Dr. Riccardo Antonello for his endless patience and for all the support: I value his friendship very much. Many thanks to all the friends I have met during the last years in the Mechatronics Lab, in particular my predecessor Matteo Carraro. Also, I sincerely appreciate the friendship and help of my PhD fellows Antonio D'Andrea, Davide Pilastro, Ilaria Palomba, Michele Vivian, Roberto Ricci and Francesco Giuliani from Parma.

Grazie al Giosaz, Diego, Stefano e tutti gli altri! Tanti sono i momenti che abbiamo passato assieme e che riempiono ampie pagine della mia vita. Vorrei ringraziare molto anche tutti gli amici incontrati grazie alla Scuola della Parola: Francesco, Emanuele e tutti gli altri. É stato fondamentale il supporto della preghiera che tante volte abbiamo fatto assieme. Grazie agli amici di sempre, Ale, Diego e a tutti gli altri! Grazie alla FUCI e a tutti i fucini: sicuramente una delle cose più belle della mia vita universitaria e non solo. Infine, grazie a tutti quelli che in qualche modo hanno fatto parte del mio cammino. Infine un particolare ringraziamento a Benedetta che mi ha aiutato a correggere questa tesi e alla sua pazienza durante questi ultimi mesi.

This research has been supported by
FSU (Fondazioni Studi Universitari) of Vicenza.
I would like to express my sincere gratitude to the Foundation
for having sponsored my PhD throughout these three years.

CONTENTS

LIST OF FIGURES

LIST OF TABLES

ACRONYMS

ADC	analog-to-digital converter
BEMF	back electromotiveforce
DAC	digital-to-analog converter
DFT	discrete Fourier transform
DSP	digital signal processor
DT	dead time
FEA	finite element analysis
FEMM	Finite Element Method Magnetics
FF	feedforward
FPGA	field-programmable gate array
FOC	field oriented control
HV	higher voltage
HF	high frequency
IGBT	insulate gate bipolar transistor
IM	induction motor
IPM	interior permanent magnet
LS	least square
LUT	look-up table
LV	low voltage
MRAS	model reference adaptive system
MTPA	maximum torque per ampere
OLS	ordinary least square
PCB	printed circuit board
PID	proportional integral derivative

PLL	phase-locked loop
PM	permanent magnet
PMARel	permanent magnet assisted reluctance motor
PMSM	permanent magnet synchronous motor
PWM	pulse width modulation
SPM	surface permanent magnet
SRM	synchronous reluctance motor
SVM	space vector modulation
VCO	voltage controlled oscillator
VMS	voltage measurement system
VSI	voltage source inverter

NOMENCLATURE

α_B	Static friction coefficient of a generic system
$\alpha_{B,l}$	Static friction coefficient of the load
$\alpha_{B,m}$	Static friction coefficient of the motor
B	Viscous coefficient of a mechanical system
β	Current phase angle in the dq plane
B_l	Viscous coefficient of the load
B_m	Viscous coefficient of the motor
W'_{fld}	Coenergy of the magnetic field
F_s	PWM sampling frequency
i_a, i_b, i_c	Phase line currents
i_{ref}	Magnitude of the current in the MTPA point
J	Inertia of a mechanical system
J	Inertia of the load
J	Inertia of the motor
J_c	Inertia of the couplings
K_c	Cross-coupling term in d-axis with the MTPA based procedure

λ_d d-axis flux linkage

Λ_{mg} Permanent magnet flux linkage

λ_q q-axis flux linkage

L_d d-axis apparent inductance

L_{eq} Equivalent inductance for initial position identification

L_q q-axis apparent inductance

$\mathcal{L}$ Lagrangian operator

$\mathcal{R}_x$ Reluctance of phase x

ω_m Mechanical angular speed

ω_m Mechanical speed of the rotor

ω_{me} Electromechanical angular speed

R_i Iron losses equivalent resistance

$\mathbf{T}_{abc/\alpha\beta o}$ Matrix transformation from abc to $\alpha\beta o$ reference frame

$\mathbf{T}_{\alpha\beta/dq}$ Matrix transformation from $\alpha\beta$ to dq reference frame

τ Electromechanical torque

τ_L Load torque

ϑ_m Mechanical position

ϑ_{me} Electromechanical position

T_s PWM sampling time

u_a, u_b, u_c Phase line voltages

u_{dist} Voltage distortion due to inverter non idealities

W_{elec} Electrical energy

W_{fld} Energy in the magnetic field

W_{mech} Mechanical energy

ξ Motor saliency

B Viscous friction coefficient

J Moment of inertia

L_σ Leakage inductance

L_{app} Apparent inductance

L_a, L_b, L_c Auto-inductances of each motor phase

L_{incr} Incremental or tangential inductance

M_{ab}, M_{bc}, M_{ac} Mutual inductances

p Pole pairs

u_o Homopolar voltage

(i_d, i_q) Currents in dq reference frame

(u_d, u_q) Voltages in dq reference frame

REMARKS ABOUT NOTATION

Scientific documents often use different notation with mathematical operators as well as physical quantities. For the sake of clarity, the following section aims at listing the most used notation adopted in this work.

Matricies and Vectorial quantities

Matrices and vectorial quantities will be specified by means of *bold* letters. For instance:

$$\mathbf{g} = Ge^{j\vartheta}$$

where $\mathbf{g}$ is a vector of magnitude G and phase ϑ.

Mathematical notation

DIFFERENTIATION The derivative of a dependent variable is indicated with a dot over its symbol. In this work it is used only to indicate

- *speed*:

$$\frac{d\vartheta}{dt} = \dot{\vartheta}$$

- *acceleration*:

$$\frac{d\omega}{dt} = \dot{\omega}$$

Part I

PERMANENT MAGNET SYNCHRONOUS MOTORS

1

PMSM

Permanent magnets have not been used for electrical machines for a long time because the development of permanent magnet materials was not mature until mid 20^{th} century. The improvement of the quality of permanent magnet materials and the technical advances of the control methods have allowed the grow of permanent magnet machines implementation in many industrial areas. In the last three decades, permanent magnet synchronous motor (PMSM)s have experienced a huge boost on their implementation thanks to their higher performances compared to DC and induction motor (IM)s. Furthermore, PMSMs provide the best torque/power density, allowing a sensible reduction of space compared to IM, which have allowed their surprisingly implementation even in home appliances products. Furthermore, the high torque to volume ratio makes PMSM motors ideal for vehicular applications. The application range of PMSM has increased thanks to the development of different motor topologies as well as the advances in construction technologies.

However, PMSMs have some drawbacks due to their own permanent magnets. The magnetic field produced by the permanent magnet (PM) is constant and cannot be controlled as easily as, for example, in an IM, by changing the field current. Furthermore, to allow the proper exploitation of the PMSM torque, it is necessary to know the exact position of the rotor. The latter information is usually obtained by means of mechanical sensors such as encoders or resolvers. Another issue is the necessary implementation of an advanced control system on fast processors such as digital signal processor (DSP)s, field-programmable gate array (FPGA) and so on. For operations above the nominal speed, the permanent magnets produce a significant back electromotive force (EMF) that must be controlled. Finally, the permanent magnets are sensible to the temperature and this might preclude their use in some applications [66].

PMSM topologies are influenced by the amount and position of PMs in the motor. They span from the pure isotropic motors, known as surface permanent magnet (SPM)s, to the extreme case of pure reluctance motors, synchronous reluctance motor (SRM)s, which deliver reluctance torque only and PM are not used any more. In between the two ends, there are topologies that differentiate from each other by the PM placement in the rotor frame [14]. In particular, the intermediate solutions are referred to as:

- interior permanent magnet (IPM);
- permanent magnet assisted reluctance motor (PMARel).

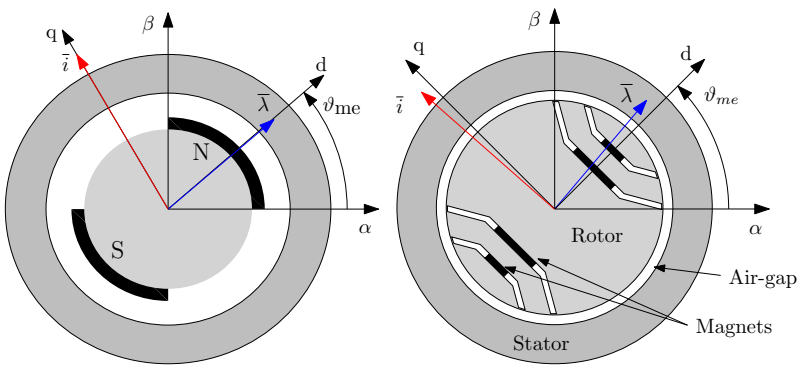

(a) SPM (b) IPM

Figure 1.1: Cross sectional view of SPM and IPM

Both structures perform the torque production with a combination of electromagnetic and reluctance principles. The former show a predominant electromagnetic torque output compared to the reluctance one, while the reluctance torque is the major output contribution in PMARel motors.

This thesis focuses in particular on SPM and IPM motors, whose cross sectional views are reported in Figure 1.1. In Figure 1.1b it is shown that the magnetic flux induced by the magnets defines the rotor direct axis d. The rotor quadrature axis q is situated at 90 electrical degrees counterclockwise from the d-axis. As shown in Figure 1.1b, the d- and q-axes have different magnetic paths: the d-axis air-gap is virtually greater than the q-axis air-gap, since the PM relative permeability is close to unity. On the contrary, the q-axis magnetic path is mostly on iron. This means that the d- and q-axes reluctances are different, allowing the production of reluctance torque.

In industrial applications, most of the energy consumption process involves motors and drives [38, 85]: besides the system cost, energy saving has become a more important aspect to take into consideration in the development of electrical drives. For instance, to lessen the pollution problem of the urban area, the electric vehicles are drawing more and more attention. The limited energy storage capability calls for efficient electric motors. As it will discussed at length in the body of this work, IPMs have some interesting aspects regarding the energy consumption.

Nowadays, IPMs are widely used in many mechatronics application fields like automotive, locomotive traction drives, air conditioning, heat pump compressors [85]. Even home domestic products, such as washing machines and dryers, represent possible applications due to the increasing performance standards required by both institution and customers.

1.1 MATHEMATICAL MODEL OF PMSM

In order to obtain the mathematical model of a PMSM, the following assumptions are made:

- the stator windings generate a sinusoidal space distribution of flux in the air gap;
- the air gap is uniform;
- the saturation is negligible;
- the motor is a balanced three phase load.

1.1.1 *Parameter based model*

The inductances of an electric motor can be written like[1]:

$$\begin{aligned} L_a &= L_\sigma + L_0 - L_2 \cos(2\vartheta_{me}) \\ L_b &= L_\sigma + L_0 - L_2 \cos(2\vartheta_{me} - \frac{4\pi}{3}) \\ L_c &= L_\sigma + L_0 - L_2 \cos(2\vartheta_{me} - \frac{2\pi}{3}) \end{aligned} \tag{1.1}$$

where L_σ is the leakage inductance. By assuming $\mathcal{R}_d$ and $\mathcal{R}_q$ as d- and q-axis reluctances respectively and N the equivalent number of turns for each phase, the following inductances are defined:

$$\begin{aligned} L_0 &= N^2 \frac{1/\mathcal{R}_d + 1/\mathcal{R}_q}{2} \\ L_2 &= N^2 \frac{1/\mathcal{R}_d - 1/\mathcal{R}_q}{2} \end{aligned} \tag{1.2}$$

It is possible to define also the mutual inductances between stator phases:

$$\begin{aligned} M_{ab} &= -\frac{1}{2} L_0 - L_2 \cos(2\vartheta_{me} - \frac{2\pi}{3}) \\ M_{bc} &= -\frac{1}{2} L_0 - L_2 \cos(2\vartheta_{me}) \\ M_{ac} &= -\frac{1}{2} L_0 - L_2 \cos(2\vartheta_{me} - \frac{4\pi}{3}) \end{aligned} \tag{1.3}$$

The voltage balance can be written as follows:

$$\begin{aligned} u_a = R i_a + L_a \frac{di_a}{dt} + M_{ab} \frac{di_b}{dt} + M_{ac} \frac{di_c}{dt} + \frac{dL_a}{dt} i_a \\ + \frac{dM_{ab}}{dt} i_b + \frac{dM_{ac}}{dt} i_c + e_a \end{aligned}$$

1 The inductance equations can be obtained from [59] at pag.174 or [41] from pag.249.

$$u_b = Ri_b + L_b\frac{di_b}{dt} + M_{ab}\frac{di_a}{dt} + M_{bc}\frac{di_c}{dt} + \frac{dM_{ab}}{dt}i_a + \frac{dL_b}{dt}i_b + \frac{dM_{bc}}{dt}i_c + e_b \quad (1.4)$$

$$u_c = Ri_c + L_c\frac{di_c}{dt} + M_{ac}\frac{di_a}{dt} + M_{bc}\frac{di_b}{dt} + \frac{dM_{ac}}{dt}i_a + \frac{dM_{bc}}{dt}i_b + \frac{dL_c}{dt}i_c + e_c$$

The voltages equation in matrix form is:

$$\mathbf{u}_{abc} = \mathbf{R}\mathbf{i}_{abc} + \frac{d\mathbf{L}_{abc}\mathbf{i}_{abc}}{dt} + \mathbf{e}_{abc} \quad (1.5)$$

where:

$$\mathbf{u}_{abc} = \begin{bmatrix} u_a \\ u_b \\ u_c \end{bmatrix} \qquad \mathbf{i}_{abc} = \begin{bmatrix} i_a \\ i_b \\ i_c \end{bmatrix} \qquad \mathbf{e}_{abc} = \begin{bmatrix} e_a \\ e_b \\ e_c \end{bmatrix}$$

and $\mathbf{R}$, $\mathbf{L}_{abc}$ are the matrix of resistance and inductance respectively:

$$\mathbf{R} = \begin{bmatrix} R & 0 & 0 \\ 0 & R & 0 \\ 0 & 0 & R \end{bmatrix} \quad (1.6)$$

$$\mathbf{L}_{abc} = \begin{bmatrix} L_a & M_{ab} & M_{ac} \\ M_{ab} & L_b & M_{bc} \\ M_{ac} & M_{bc} & L_c \end{bmatrix} \quad (1.7)$$

In a three phase system, the $\alpha\beta o$ reference frame is often used, for its compactness and meaningful representation even of unbalanced systems [40]. The matrix transformation $\mathbf{T}_{abc/\alpha\beta o}$ is defined as follows:

$$\mathbf{T}_{abc/\alpha\beta o} = \begin{bmatrix} 1 & 0 & 1/\sqrt{2} \\ -1/2 & \sqrt{3}/2 & 1/\sqrt{2} \\ -1/2 & -\sqrt{3}/2 & 1/\sqrt{2} \end{bmatrix} \quad (1.8)$$

and it goes under the name of *Clarke transformation*, in honour of Edith Clarke [40]. In compact notation, it stands:

$$\mathbf{g}_{\alpha\beta o} = \mathbf{T}_{abc/\alpha\beta o}\mathbf{g}_{abc} \quad (1.9)$$

By applying (1.9) on (1.5), the $\alpha\beta o$ matrix model of the motor is:

$$\mathbf{u}_{\alpha\beta o} = \mathbf{R}\mathbf{i}_{\alpha\beta o} + \mathbf{L}_{\alpha\beta o}\frac{d\mathbf{i}_{\alpha\beta o}}{dt} + \mathbf{e}_{\alpha\beta o} \quad (1.10)$$

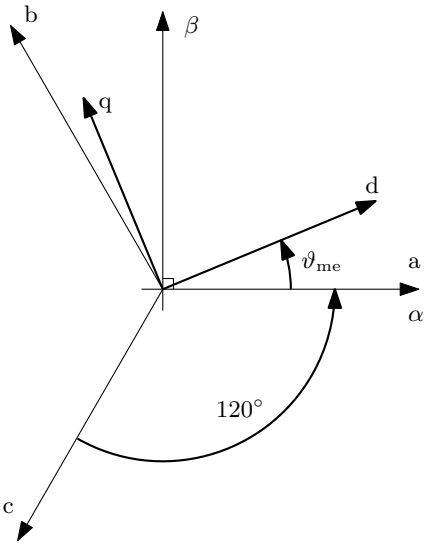

Figure 1.2: Graphic representation of a three phase system, αβ and dq reference frames.

The inductance matrix $\mathbf{L}_{\alpha\beta o}$ is obtained by applying (1.9) on (1.8).

In general, electric motors can be considered as a balanced three phase system. The *hompolar component* g_o in both currents and voltages can be thus considered null. Equation (1.10) can be simplified by omitting the subscript "o". Based on the initial assumptions [2], and on the absence of the neutral wire, it is possible to neglect this term. However, the homopolar component has no effect on the torque production. In turn, the αβ components only are considered in the following. Equation (1.10) without the homopolar component is equal to:

$$\mathbf{u}_{\alpha\beta} = \mathbf{R}\mathbf{i}_{\alpha\beta} + \mathbf{L}_{\alpha\beta}\frac{d\mathbf{i}_{\alpha\beta}}{dt} + \mathbf{e}_{\alpha\beta} \tag{1.11}$$

where all quantities are 2×1.

The transformation from the stationary reference frame αβ to the synchronous dq fixed to the rotor flux, is:

$$\mathbf{g}_{dq} = \mathbf{T}_{\alpha\beta/dq}\mathbf{g}_{\alpha\beta} \tag{1.12}$$

where

$$\mathbf{T}_{\alpha\beta/dq} = \begin{bmatrix} \cos(\vartheta_{me}) & \sin(\vartheta_{me}) \\ -\sin(\vartheta_{me}) & \cos(\vartheta_{me}) \end{bmatrix} \tag{1.13}$$

Since the PMs are placed on the rotor, the dq reference frame rotates synchronously with the rotor by means of a factor p, i.e. the number of pole pairs of the rotor [42]. The electromechanical angle ϑ_{me} is

2 i.e. the stator windings generates a sinusoidal magnetic field, the air gap is uniform and the saturation is negligible.

defined as the multiplication of the mechanical angle ϑ_m by the motor pole pairs p.

The mathematical model of the PMSM motor in dq reference frame is obtained by applying (1.12) on each vectorial quantity of (1.11). Omitting the homopolar component, the dq motor model is:

$$\mathbf{u}_{dq} = \mathbf{R}\mathbf{i}_{dq} + \mathbf{L}_{dq}\frac{d\mathbf{i}_{dq}}{dt} + \mathbf{e}_{dq} \tag{1.14}$$

where:

$$\begin{aligned} \mathbf{u}_{dq} &= [u_d \; u_q]; \\ \mathbf{i}_{dq} &= [i_d \; i_q]; \\ \mathbf{e}_{dq} &= [0 \; \omega_{me}\Lambda_{mg}]. \end{aligned} \tag{1.15}$$

and $\omega_{me} = p\omega_m$ is the electromechanical angular speed obtained by ω_m and the mechanical angular speed of the rotor.

The resistance matrix has the parameter R on its diagonal, (1.6), since the system is supposed to be balanced. The inductances matrix (1.7) becomes constant, because with the new reference frame, it loses the position dependency, and then the time dependency:

$$\mathbf{L}_{dq} = \begin{bmatrix} L_d & 0 \\ 0 & L_q \end{bmatrix}$$

where L_d and L_q are d- and q-axis magnetizing inductance respectively and are equal to:

$$\begin{aligned} L_d &= L_\sigma + \frac{3}{2}(L_0 - L_2) \\ L_q &= L_\sigma + \frac{3}{2}(L_0 + L_2) \end{aligned} \tag{1.16}$$

The matrix equation 1.14 can be split into the dq axes as follows:

$$u_d = Ri_d + L_d\frac{di_d}{dt} - \omega_{me}L_q i_q \tag{1.17}$$

$$u_q = Ri_q + L_q\frac{di_q}{dt} + \omega_{me}L_d i_d + \omega_{me}\Lambda_{mg} \tag{1.18}$$

For the sake of completeness, the block scheme of the motor is reported in Figure 1.3. It is valid for both isotropic and anisotropic motor with PM. In fact, isotropic motors present no saliency, i.e. $L_d = L_q$, thus the reluctance torque term disappears.

For the sake of discussion, the anisotropy level of an electric motor is called *saliency* and it is defined as:

$$\xi = \frac{L_q}{L_d} \tag{1.19}$$

On one hand, the saliency of an SPM is 1 by definition. On the other hand, the saliency of anisotropic motors varies with the rotor structure [17]. In particular, for a motor like the one in Figure 1.1b, the saliency is between 2 and 5. High saliency values are expected for SRM, between 6 and 9 [14].

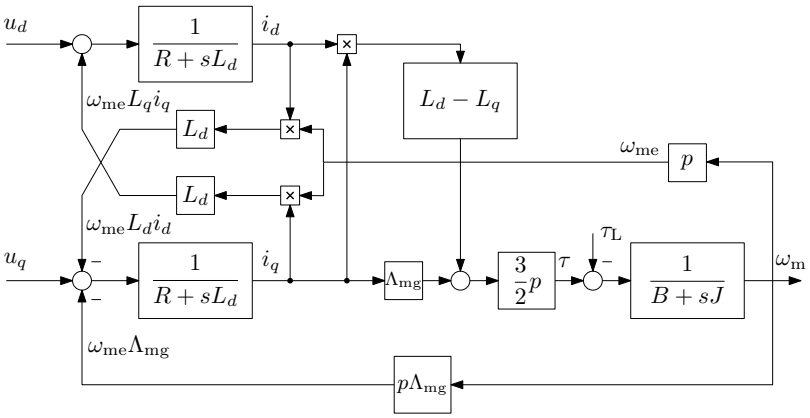

Figure 1.3: Block scheme of a linear PMSM

1.1.2 *Flux linkage model*

In Sect. 1.1.1, the PMSM mathematical model was obtained under the hypothesis of linearity of all the model parameters, i.e. resistance and inductances. However, due to the iron magnetic saturation, the rotor magnetic saliency and the armature reaction effects, the values of the inductances change with the current magnitude. The higher the saliency, the greater the inductance variation. From Figure 1.1b, it appears quite evident that d and q-axis magnetic paths have different behaviours when current is flowing in the stator windings. Saturation mostly affects L_q, due to the presence of PM on the d-axis magnetic path.

A mathematical model for PMSM considering magnetic saturation is:

$$\begin{aligned} u_d &= Ri_d + \frac{d\lambda_d(i_d, i_q)}{dt} - \omega_{me}\lambda_q(i_d, i_q) \\ u_q &= Ri_q + \frac{d\lambda_q(i_d, i_q)}{dt} + \omega_{me}\lambda_d(i_d, i_q) \end{aligned} \tag{1.20}$$

where $\lambda_d(i_d, i_q)$ and $\lambda_q(i_d, i_q)$ are the flux linkages on the d- and q-axis, and $\lambda_d(i_d, i_q)$ takes into account the PM flux linkage Λ_{mg} as well. In particular, λ_d and λ_q are non-linear functions of currents i_d and i_q. Usually, λ_d and λ_q can be calculated by means of finite element analysis (FEA), Sect. 1.2, or estimated from measurements obtained on dedicated test rigs [6].

In this work, λ_d and λ_q were calculated by means of FEA analysis and their relation with the currents i_d and i_q are indicated with functions $f_1(i_d, i_q)$ and $f_2(i_d, i_q)$ respectively. The linear motor model in Figure 1.3 can be reconsidered as a simplified one of Figure 1.4.

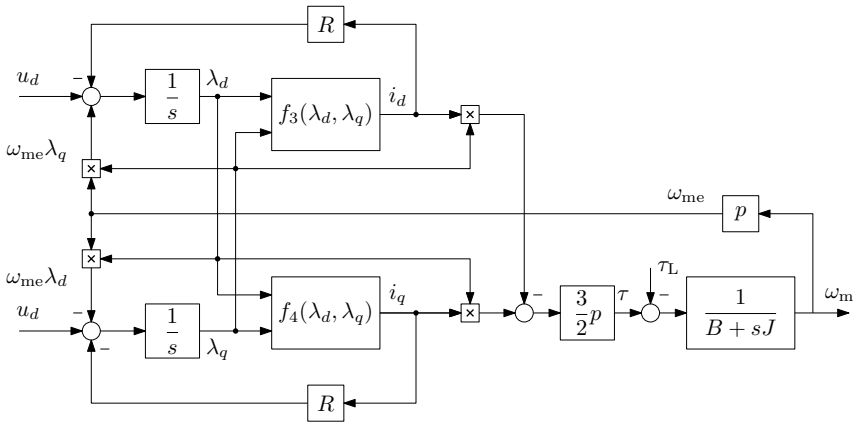

Figure 1.4: Block scheme of a non-linear PMSM. Functions f_3 and f_4 are described in Sect. 1.2.1.

1.1.3 *Torque equation*

1.1.3.1 *Energy formulation*

In order to obtain a general torque equation, a magnetic energy approach is considered. The following equations are obtained from [41, pp 113-...]. With the hypothesis that the system has no losses and it is single excited, the time rate of change of the energy in the magnetic field W_{fld} is equal to:

$$\frac{dW_{fld}}{dt} = ui - f_{fld}\frac{dx}{dt} \tag{1.21}$$

where u is the voltage at the terminals of the the lossless windings, i the current, f_{fld} the force due to the magnetic field on a mechanical body and x is the position. The voltage u is equal to:

$$u = \frac{d\lambda}{dt} \tag{1.22}$$

where λ represents the winding flux linkages. From (1.21) and (1.22) one gets:

$$dW_{fld} = id\lambda - f_{fld}dx \tag{1.23}$$

From the first law of thermodynamics it is:

$$dW_{elec} = uidt = dW_{mech} + dW_{fld} \tag{1.24}$$

The hypothesis are:

- the system is conservative;
- W_{fld} is uniquely specified by the values of λ and x.

Both λ and x are, thus, *state variables*. Being a conservative system, the integration of W_{fld} is independent from the integration path. Thus, it stands:

$$W_{fld}(\lambda_0, x_0) = \int_0^{\lambda_0} i(\lambda, x_0) d\lambda \tag{1.25}$$

For a linear system, the flux λ is proportional to the current i, thus:

$$W_{fld}(\lambda, x) = \int_0^{\lambda} i(\lambda', x) d\lambda' = \int_0^{\lambda} \frac{\lambda'}{L(x)} d\lambda' = \frac{1}{2} \frac{\lambda^2}{L(x)} \tag{1.26}$$

where $L(x)$ is the inductance.

In case of AC motors, the mechanical terminal variables are the angular position ϑ and the torque due to the magnetic field T_{fld}. Equation (1.21) is rewritten as:

$$dW_{fld}(\lambda, \vartheta) = i d\lambda - T_{fld} d\vartheta \tag{1.27}$$

The torque can be found from the negative of the partial derivative of W_{fld} respect to ϑ, holding λ constant:

$$T_{fld} = -\frac{\partial W_{fld}(\lambda, \vartheta)}{\partial \vartheta}\Big|_{\lambda} \tag{1.28}$$

For linear systems:

$$\lambda = L(\vartheta) i \qquad \rightarrow \qquad W_{fld}(\lambda, \vartheta) = \frac{1}{2} \frac{\lambda^2}{L(\vartheta)} \tag{1.29}$$

Finally, from (1.28) and (1.29):

$$T_{fld} = \frac{1}{2} \frac{\lambda^2}{L(\vartheta)^2} \frac{dL(\vartheta)}{d\vartheta} = \frac{1}{2} i^2 \frac{dL(\vartheta)}{d\vartheta} \tag{1.30}$$

1.1.3.2 *Coenergy formulation*

The torque expression can be equally obtained from the *coenergy*, which is defined as:

$$W'_{fld}(i, \vartheta) = i\lambda - W_{fld}(\lambda, \vartheta) \tag{1.31}$$

It is worth to note that coenergy is function of current, while energy is function of flux. In the same fashion as for the energy expression, the torque expressed with the coenergy is equal to:

$$T_{fld} = \frac{\partial W'_{fld}(i, \vartheta)}{\partial \vartheta}\Big|_{i} \tag{1.32}$$

Under the hypothesis of magnetic linear system, it holds:

$$W'_{fld}(i, \vartheta) = \frac{1}{2} L(\vartheta) i^2 \tag{1.33}$$

Finally, one get:

$$T_{fld} = \frac{1}{2} i^2 \frac{dL(\vartheta)}{d\vartheta} \tag{1.34}$$

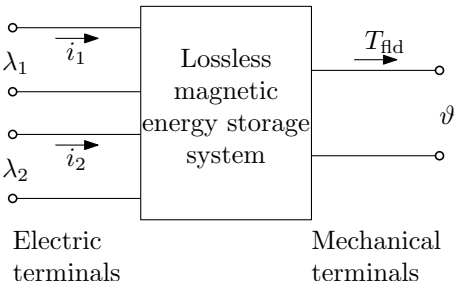

Figure 1.5: Scketch of a double excited system

1.1.3.3 *Multiple-excited magnetic field system*

In Sect. 1.1.3.1 and 1.1.3.2, the system under consideration was single excited. For the sake of simplicity, a double excitation is considered in this section as sketched in Figure 1.5,although the considerations can be extended to n excitation sources. The variation of the magnetic energy is equal to:

$$dW_{fld}(\lambda_1, \lambda_2, \vartheta) = i_1\, d\lambda_1 + i_2\, d\lambda_2 - T_{fld}\, d\vartheta \tag{1.35}$$

The variation of coenergy is equal to:

$$dW'_{fld}(i_1, i_2, \vartheta) = \lambda_1\, di_1 + \lambda_2\, di_2 - T_{fld}\, d\vartheta \tag{1.36}$$

From (1.36), it is possible to work out the fluxes:

$$\begin{aligned} \lambda_1 &= \frac{\partial W'_{fld}(i_1, i_2, \vartheta)}{\partial i_1}\Big|_{i_2,\vartheta} \\ \lambda_2 &= \frac{\partial W'_{fld}(i_1, i_2, \vartheta)}{\partial i_2}\Big|_{i_1,\vartheta} \end{aligned} \tag{1.37}$$

The torque expression as function of the currents is obtained from the coenergy formulation:

$$T_{fld} = \frac{\partial W'_{fld}(i_1, i_2, \vartheta)}{\partial \vartheta}\Big|_{i_1,i_2} \tag{1.38}$$

In a linear magnetic system, it holds that:

$$\begin{aligned} \lambda_1 &= L_{11} i_1 + L_{12} i_2 \\ \lambda_2 &= L_{21} i_1 + L_{22} i_2 \end{aligned} \tag{1.39}$$

where $L_{12} = L_{21}$ are the mutual inductances. The magnetic coenergy is equal to:

$$W'_{fld}(i_1, i_2, \vartheta) = \frac{1}{2} L_{11}(\vartheta) i_1^2 + \frac{1}{2} L_{22}(\vartheta) i_2^2 + \frac{1}{2} L_{12}(\vartheta) i_1 i_2 \tag{1.40}$$

Finally, the torque equation for a magnetic linear system is equal to:

$$T_{fld} = \frac{1}{2} i_1^2 \frac{dL_{11}(\vartheta)}{d\vartheta} + \frac{1}{2} i_2^2 \frac{dL_{22}(\vartheta)}{d\vartheta} + i_1 i_2 \frac{dL_{12}(\vartheta)}{d\vartheta} \tag{1.41}$$

It is worth to report that in a non linear system, λ and i do not vary in a proportional way. However, the following equation is general:

$$W_{fld} + W'_{fld} = \lambda i \tag{1.42}$$

Similar equations have been obtained in [7], too.

1.1.3.4 *Electric quantities formulation*

In case of linearity and under the hypothesis of conservative system [7], the torque expression is equal to:

$$\tau = \frac{3}{2} p \left(\Lambda_{mg} i_q + (L_d - L_q) i_d i_q \right) \tag{1.43}$$

Equation (1.43) identifies the two torque components. The term $\Lambda_{mg} i_q$ is the *electromagnetic torque component*, which is present in both SPM and IPM. The term $(L_d - L_q) i_d i_q$ is the *reluctance torque component* and it is due to the anisotropy of the IPM.

As stated in Sect. 1.1, L_d is smaller than L_q. In order to obtain torque from (1.43) in accordance with the desired one, coming for instance from a torque controller, i_d has to be negative. The two currents (i_d, i_q) give a degree of freedom that can be used to minimise a selected quantity, such as the magnitude of the current. The latter case corresponds to the maximum torque per ampere (MTPA) control, which will be explained in Sect. 1.3.

If fluxes (λ_d, λ_q) are considered, the electromechanical torque produced by the motor is:

$$\tau = \frac{3}{2} p (\lambda_d i_q - \lambda_q i_d) \tag{1.44}$$

Equation (1.44) is appropriate to describe the torque production even in presence of magnetic saturation. A better torque description is obtained by considering the variations of coenergy as well:

$$\tau = \frac{3}{2} p (\lambda_d i_q - \lambda_q i_d) + \frac{\partial W'_{fld}}{\partial \vartheta_m} \tag{1.45}$$

It is worth to note that the variation of coenergy accounts for all those effects which are usually neglected, such as the cogging torque. For integral-slot windings[3] [7] the approximation in (1.44) is quite accurate.

1.1.4 *Mechanical load*

According with (1.17),(1.18) and (1.43), the load mathematical expression is:

$$\tau = \tau_L + B\omega_m + J\frac{d\omega_m}{dt} \tag{1.46}$$

3 Only integral-slot windings motor are considered in this thesis. Fractional-slot windings will be considered for future activities.

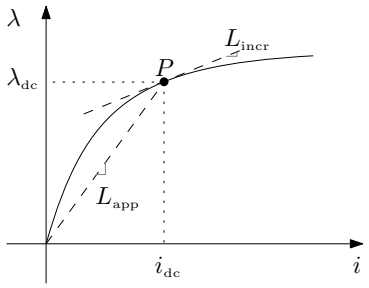

Figure 1.6: Illustration of the apparent and incremental inductance

where B and J are the viscous friction coefficient and the moment of inertia of the whole system respectively, whilst τ_L is the load torque part that is not linear dependent from position and speed. Sect. 3.2 reports a test based procedure to identify the parameter contained in (1.46). Other procedures, in particular on-line techniques, could be found in literature [62, 113].

1.1.5 *Incremental inductance*

The generic equation of an inductor is:

$$u(t) = \frac{d\lambda(i(t))}{dt} \tag{1.47}$$

where $u(t)$ and $i(t)$ are the voltage and the current respectively, while $\lambda(i(t))$ is the magnetic flux linkage. Whilst all the quantities are function of time, the magnetic flux is function of the current as well.

By assuming $\lambda(i(t)) = L_{app}(i(t))i(t)$, i.e. L_{app} is function of current only, it holds:

$$\begin{aligned} u(t) = \frac{d\lambda(i(t))}{dt} &= \frac{d(L_{app}(i(t))i(t))}{dt} \\ &= L_{app}(i(t))\frac{di(t)}{dt} + i(t)\frac{L_{app}(i(t))}{di} \cdot \frac{di(t)}{dt} \\ &= \left[L_{app}(i(t)) + i(t)\frac{L_{app}(i(t))}{di}\right]\frac{di(t)}{dt} \\ &= L_{incr}(i(t))\frac{i(t)}{dt} \end{aligned} \tag{1.48}$$

where L_{app} is the *apparent* inductance, also known as *chord-slope* inductance, and L_{incr} comes up straight forward and it is known as *incremental* or *tangential* inductance. A graphic interpretation is sketched in Figure 1.6. It is worth to highlight that both L_{app} and L_{incr} are defined for a working point P which is described by the couple (i_{dc}, λ_{dc}).

1.2 FEA ANALYSIS

A useful instrument to analyse the magnetic behaviour of the motor is the FEA. The results allow to determine the distribution of the elec-

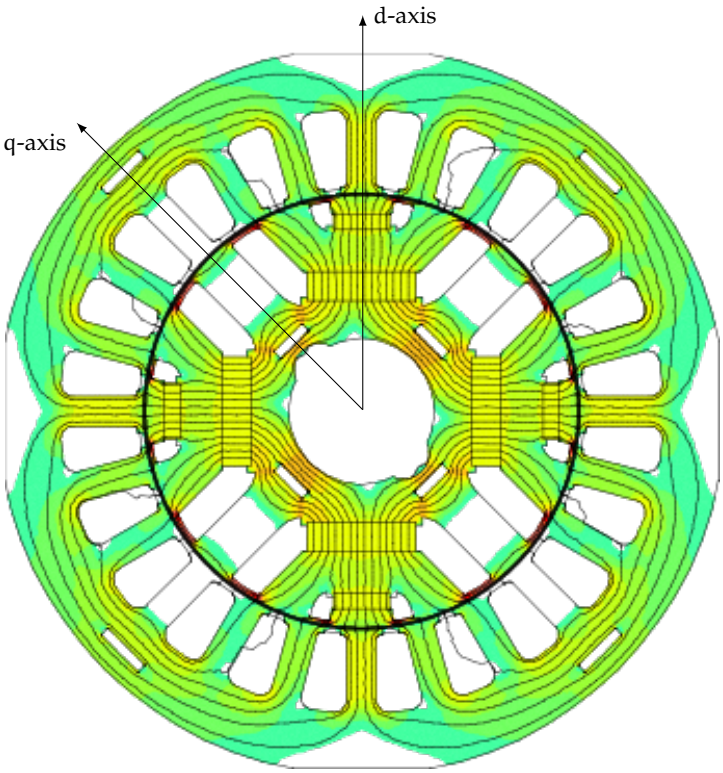

Figure 1.7: No load test of the IPM machine

tromagnetic fields inside the machine, by means of the solution of the Maxwell's equations. However, the FEA tool is used in this work only for understanding some phenomena inside the machine (for instance the iron bridges saturation) and obtaining a precise magnetic model of the motor. The model, under the form of look-up table (LUT)s, is important during the simulation analysis of advanced control algorithms.

In this work, the Finite Element Method Magnetics (FEMM) software [65] was used to carry out the simulations. The FEMM software performs only bi-dimension and static simulations, but it is sufficient to get a reliable magnetic model of the motor [13]. In fact, it is possible to take advantage of the electric motor symmetries to reduce the problem dimension from 3-D to 2-D in the solution of magnetostatic problems. The magnetic behaviour is supposed to be identical along the longitudinal axis of the motor and the end-windings are not considered.

The geometry of an IPM machine is reported in Figure 1.7, obtained under no load conditions. There is no evident magnetic saturation, except in the iron bridges of the rotors. The motor of Figure 1.7 is considered as a significant motor model in this thesis and all considerations can be extended to other PMSM rotor structure.

The magnetic fluxes are the most interesting FEA results from the AC drives designer point of view. The fluxes of the dq motor model

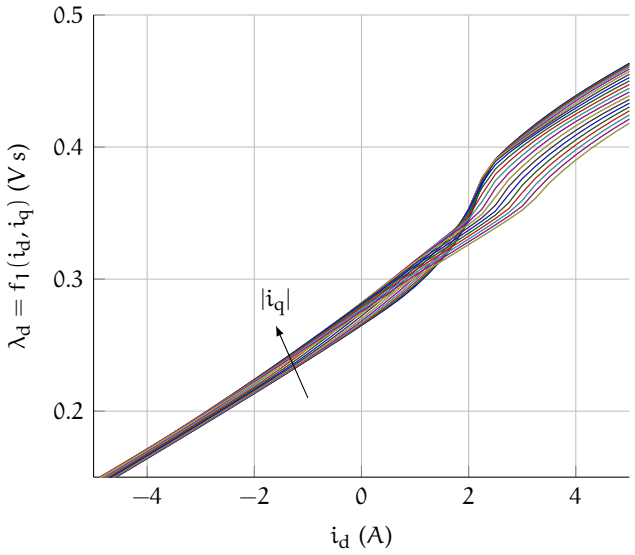

(a) d-axis flux linkage

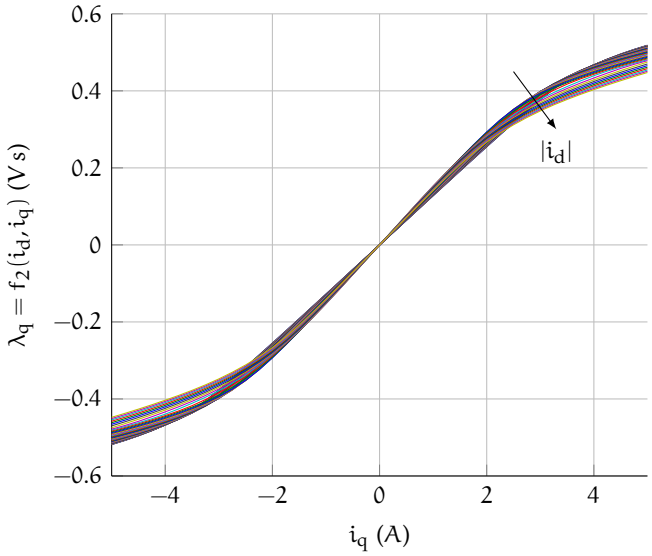

(b) q-axis flux linkage

Figure 1.8: Flux linkages of the IPM machine

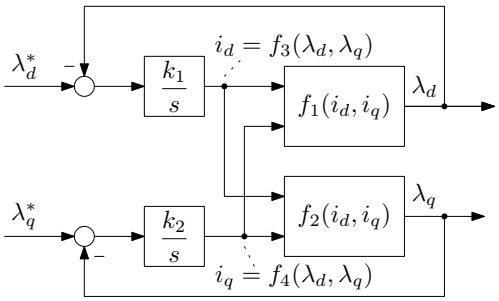

Figure 1.9: Off-line procedure scheme to calculate f_3 and f_4.

are reported in Figure 1.8. It is interesting to note that λ_d is not zero at null i_d, due to the presence of the PM. Another interesting aspect is the behaviour of the d-flux with positive i_d. The reason of that has to be pointed to the iron bridges desaturation, as discussed in Sect. 1.2.2.

1.2.1 *Magnetic model for motor simulation*

The family of curves in Figure 1.8 indicates how the flux on one axis is influenced by both currents i_d and i_q. The magnetic flux dependence of one axis from the current in the other axis is called *cross-coupling* [46, 96]. The magnetic fluxes function of (i_d, i_q) are defined as $\lambda_d = f_1(i_d, i_q)$ and $\lambda_q = f_2(i_d, i_q)$. The function $f_1(i_d, i_q)$ and $f_2(i_d, i_q)$ can be stored into LUTs (the most common choice) or approximated by means of polynomial functions. In order to use the FEA results in simulation model, though, the f_1-f_2 function are of difficult implementation. On the contrary, fluxes can be calculated from (1.20), from which the currents can be obtained by reversing[4] the f_1-f_2 functions into the $f_3(\lambda_d, \lambda_q) = f_1^{-1}$ and $f_4(\lambda_d, \lambda_q) = f_2^{-1}$. The calculation of f_3 and f_4 can be carried out only numerically. A method to calculate the latter two functions is reported in [21].

In this work, f_3 and f_4 have been calculated by means of the algorithm sketched out in Figure 1.9. The value of λ_d^* and λ_q^* are decided a priori by defining the minimum and maximum of each flux respectively and the desired quantisation. For each couple of $(\lambda_d^*, \lambda_d^*)$, the output at steady state of the integral blocks are the couple (i_d, i_q) which minimise the estimation error. Hence, the outputs of the blocks are indeed the functions f_3 and f_4. The gains k_1 and k_2 can be used to speed up the convergence of the algorithm. Finally, it is worth to highlight that the procedure is performed off-line and the computational efforts do not undermine the algorithm implementation.

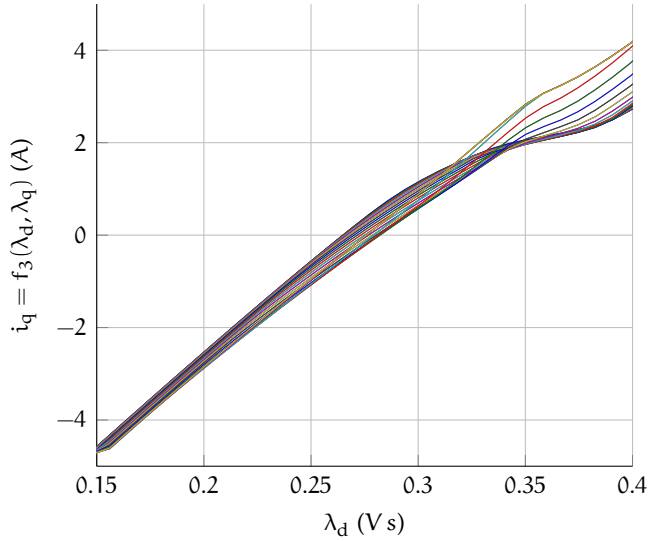

(a) d-axis flux linkage

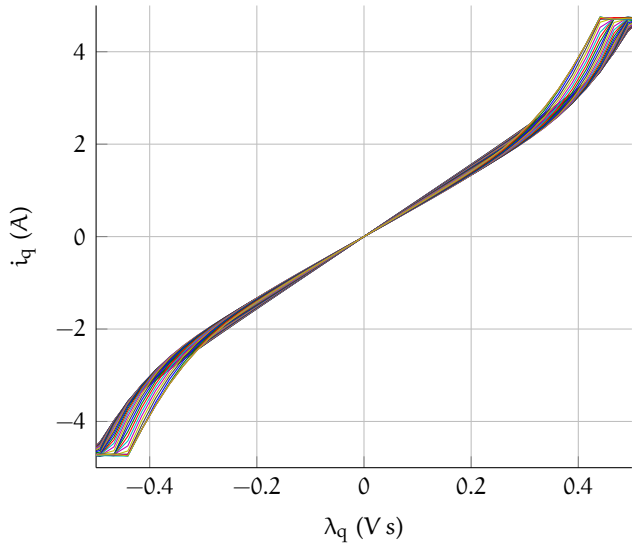

(b) q-axis flux linkage

Figure 1.10: $f_3(\lambda_d, \lambda_q)$ and $f_4(\lambda_d, \lambda_d)$ obtained from Figure 1.8 with Figure 1.9.

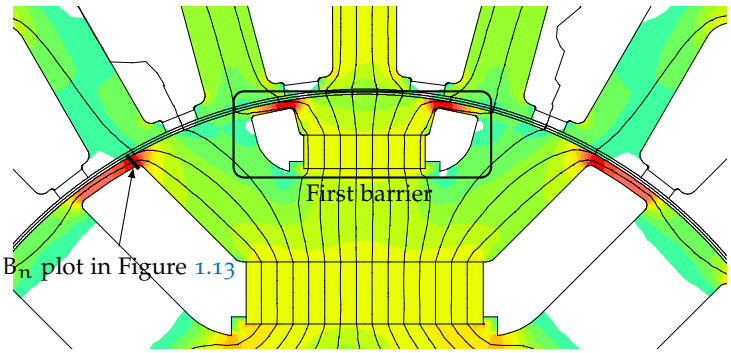

Figure 1.11: Particular of one pole of the machine at no load

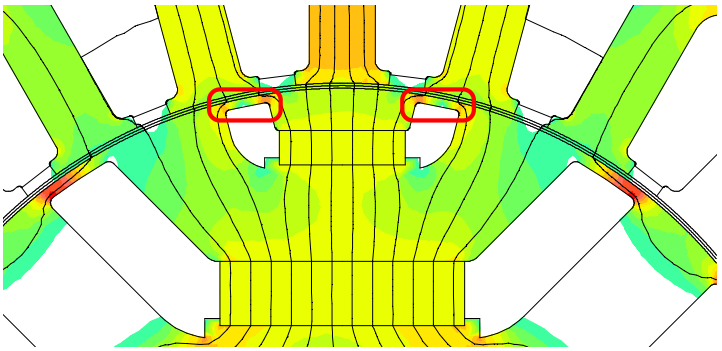

Figure 1.12: Desaturated iron bridges (thick red rectangles) at $i_d = 3\,A$

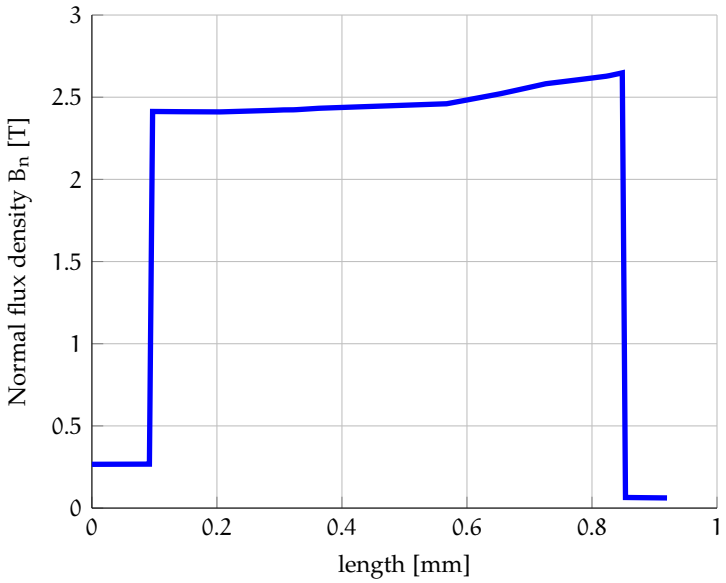

Figure 1.13: Normal flux density in the iron bridge

1.2.2 *Iron bridges saturation*

To ease the analysis, the Figure 1.7 is enlarged into the Figure 1.11. In theory, the iron bridges represent a magnetic short circuit to the magnetic flux. However, they are of basic importance since they guarantee the mechanical strength of the laminated rotor. The magnetic flux produced by the PM saturates the iron bridges even without stator currents. The normal flux density B_n in the iron bridge is reported in Figure 1.13: the flux density is around 2 T, which is almost equal to the iron saturation level[5] and it gets close to 2.5 T in the most saturated region.

However, the iron bridge saturation effect is influenced by the load condition, i.e. it depends on both d- and q-axis currents. By applying

4 It is worth to highlight that both $f_1(i_d, i_q)$ and $f_2(i_d, i_q)$ are monotone increasing, Figure 1.8.

5 In case of high permeability iron, such as the one used in the electrical machine, the saturation value is between 1.6 and 2.2 T.

a negative d-axis current i_d, the magnetic flux induced by the current enhances the iron bridge saturation. On the other hand, a positive i_d produces a magnetic flux opposite to the PM's one, so the iron bridges are driven towards the linear region [74]. A particular of the motor with $i_d = 3\,A$ is reported in Figure 1.12. The iron bridges of the first barrier are desaturated and that makes the d-axis magnetic inductance grow.

On the one hand, this effect in [74] is fruitfully used to detect the initial position of the rotor. On the other hand, it deteriorates the operations of the drive.

The iron bridges are influenced by the q-axis current as well. This is due to the cross-coupling effect, which means that the q-axis current value has effects on the d-axis flux behaviour and vice-versa. The cross-saturation also affects sensorless performances [46], HF sensorless [88] and its relationship with the rotor structure [15]. An accurate model of the IPM motor is presented also in [5].

1.3 MAXIMUM TORQUE-PER-AMPERE TECHNIQUES

The expression of the torque produced by the motor in (1.43) suggests the most suitable control in case of SPM. In fact, isotropic motors present the same inductances on both d- and q-axis, which means a null reluctance torque in (1.43). Hence, the electromechanical torque for an SPM is:

$$\tau = \frac{3}{2} p \Lambda_{mg} i_q \tag{1.49}$$

Therefore, i_q is the only producing torque current in SPM motors. The i_d current is controlled to zero. Such kind of control is called field oriented control (FOC), since the current vector is always $\pi/2$ leading (or lagging in case of braking operation) the permanent magnet flux vector, as sketched in Figure 1.1a.

In case of IPM motors, equation (1.43) shows that there is a further degree of freedom in the torque production. In order to obtain the maximum torque for a given current magnitude, the current vector phase has to be properly selected. The optimal current phase angle control is called MTPA.

1.3.1 *Theory of MTPA*

The MTPA control aims at finding the optimal operating point by minimizing the current magnitude in every operative condition. The optimal point is obtained when the following condition is verified:

$$\frac{\partial \tau}{\partial |i|} = \frac{\partial \tau}{\partial i_d} \left(\frac{\partial |i|}{\partial i_d} \right)^{-1} = 0 \tag{1.50}$$

The application of (1.50) to (1.43) yields:

$$i_d = \frac{\Lambda_{mg} \pm \sqrt{\Lambda_{mg}^2 + 8(L_d - L_q)^2 i_{ref}^2}}{-4(L_d - L_q)} \tag{1.51}$$

where $i_{ref} = \sqrt{i_d^2 + i_q^2}$ is the minimum current magnitude for a specific torque. As mentioned in Sect. 1.1.3, i_d must be negative to produce torque in accordance with the i_q sign. i_{ref} definition also allows to calculate i_q once i_d is obtained from (1.51).

It is worth noticing that (1.51) is based on constant parameters. It does not take magnetic saturation into account. By using the torque formula in (1.44), the MTPA condition can be obtained in two different ways, i.e. considering the minimisation of the current magnitude with constrained torque or the torque maximisation with constrained current magnitude. Sect. 1.3.2 and 1.3.3 aim at demonstrating the equality of both approaches.

1.3.2 *Current magnitude minimisation with constrained torque*

The MTPA point is obtained as the solution of the following constrained minimisation problem:

$$\min_{(i_d, i_q)} \sqrt{i_d^2 + i_q^2} \qquad \text{subject to} \qquad \tau(i_d, i_q) = \tau_{ref} \tag{1.52}$$

where $\tau(i_d, i_q)$ is (1.43) and τ_{ref} is a specific constant torque demand. The solution of (1.52) can be searched among the stationary points of the Lagrangian

$$\mathcal{L}(i_d, i_q, \lambda) = \sqrt{i_d^2 + i_q^2} + \lambda\big(\tau(i_d, i_q) - \tau_{ref}\big) \tag{1.53}$$

i.e. the solutions of the following set of equations:

$$\frac{\partial \mathcal{L}}{\partial i_d} = \frac{i_d}{\sqrt{i_d^2 + i_q^2}} + \lambda \frac{\partial \tau}{i_d} = 0 \tag{1.54}$$

$$\frac{\partial \mathcal{L}}{\partial i_q} = \frac{i_q}{\sqrt{i_d^2 + i_q^2}} + \lambda \frac{\partial \tau}{i_q} = 0 \tag{1.55}$$

$$\frac{\partial \mathcal{L}}{\partial \lambda} = \tau(i_d, i_q) - \tau_{ref} = 0 \tag{1.56}$$

Assume that $\partial\tau/\partial i_d \neq 0$: then, solving (1.54) for λ yields

$$\lambda = -\frac{i_d}{\sqrt{i_d^2 + i_q^2}} \left(\frac{\partial \tau}{\partial i_d}\right)^{-1} \tag{1.57}$$

that can be replaced into (1.55) to get the following mathematical condition for the MTPA operating point

$$i_q \frac{\partial \tau}{\partial i_d} - i_d \frac{\partial \tau}{\partial i_q} = 0 \tag{1.58}$$

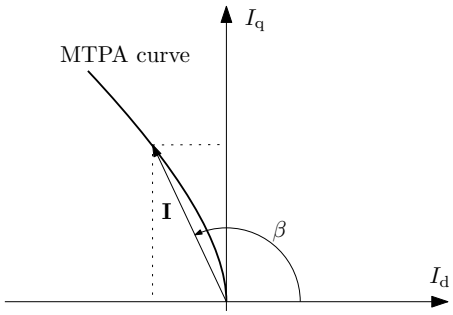

Figure 1.14: MTPA curve example and definition of load angle β of current vector $\mathbf{I}$ in the dq current plane.

1.3.3 *Torque maximisation with constrained current magnitude*

The MTPA operating condition is obtained as the solution of the following constrained maximisation problem:

$$\max_{(i_d,i_q)} \tau(i_d,i_q) \qquad \text{subject to} \qquad \sqrt{i_d^2+i_q^2} = i_{ref} \tag{1.59}$$

where $\tau(i_d,i_q)$ is (1.43) and i_{ref} is the imposed constant current magnitude. The solution of (1.59) can be searched among the stationary points of the Lagrangian

$$\mathcal{L}(i_d,i_q,\lambda) = -\tau(i_d,i_q) + \lambda\left(\sqrt{i_d^2+i_q^2} - i_{ref}\right) \tag{1.60}$$

i.e. the solutions of the following set of equations:

$$\frac{\partial\mathcal{L}}{\partial i_d} = -\frac{\partial\tau}{\partial i_d} + \lambda\frac{i_d}{\sqrt{i_d^2+i_q^2}} = 0 \tag{1.61}$$

$$\frac{\partial\mathcal{L}}{\partial i_q} = -\frac{\partial\tau}{\partial i_q} + \lambda\frac{i_q}{\sqrt{i_d^2+i_q^2}} = 0 \tag{1.62}$$

$$\frac{\partial\mathcal{L}}{\partial\lambda} = \sqrt{i_d^2+i_q^2} - i_{ref} = 0 \tag{1.63}$$

Assume $i_d \neq 0$: then, solving (1.61) for λ yields

$$\lambda = -\frac{\sqrt{i_d^2+i_q^2}}{i_d}\frac{\partial\tau}{\partial i_d} \tag{1.64}$$

that can be replaced into (1.62) to get the following mathematical condition for the MTPA operating point

$$i_q\frac{\partial\tau}{\partial i_d} - i_d\frac{\partial\tau}{\partial i_q} = 0 \tag{1.65}$$

Note that condition (1.58) coincides with (1.65) obtained in Sect. 1.3.2.

The MTPA condition is reached when:

- i_d and i_q null (that is an insignificant solution);
- derivative terms $\partial\tau/\partial i_q$ and $\partial\tau/\partial i_d$ null.

The MTPA condition in (1.50) still holds even with the torque formulation (1.44). It is interesting to note that the MTPA condition can be expressed in terms of dq currents. The same dq currents are the component of a current vector as in Figure 1.14. Therefore, the MTPA condition (1.50) can be expressed even in terms of current phase angle β, i.e. considering the current vector in polar coordinates. With the definition of i_{ref} in (1.59) and considering the phase angle β, it stands:

$$i_q = i_{ref}\cos(\beta) \qquad i_d = i_{ref}\sin(\beta) \tag{1.66}$$

Substituting (1.66) into (1.43), for instance, the torque is function of the current magnitude $|i(\beta)|$ and phase β, from which the MTPA equation can be drawn by means of the following optimisation problem:

$$\min_{\beta}(|i(\beta)|) \qquad \text{subject to} \qquad \tau(|i(\beta)|,\beta) = \tau_{ref} \tag{1.67}$$

It is worth to highlight the similarities of (1.67) with (1.52).

1.3.4 *MTPA algorithms*

There are several viable ways to obtain the MTPA curve of a PMSM motor. In particular:

- parameter based;
- FEA analysis based;
- model-free based.

The former one relies on the precise knowledge of the machine parameters, whose can be estimated by several methods [79, 84]. The FEA based technique requires the design parameters of the machine, whose are not usually available. The latter group is the most interesting one, since it does not depends on the motor parameters, but it is only a matter of control. Some model-free, mostly perturbation-and-observe methods based on extremum seeking control working principle, MTPA techniques are [3, 25, 57, 97].

Another model-free technique is the actual measurement of the MTPA by means of experiments to be carried out in laboratory premises. The test rig is reported in Figure 1.15. The PMSM motor is driven by another motor at constant speed. Meanwhile, just i_d and i_q currents of the PMSM motor drive are controlled and modified in order to map the whole region of work of the machine. In other words, the

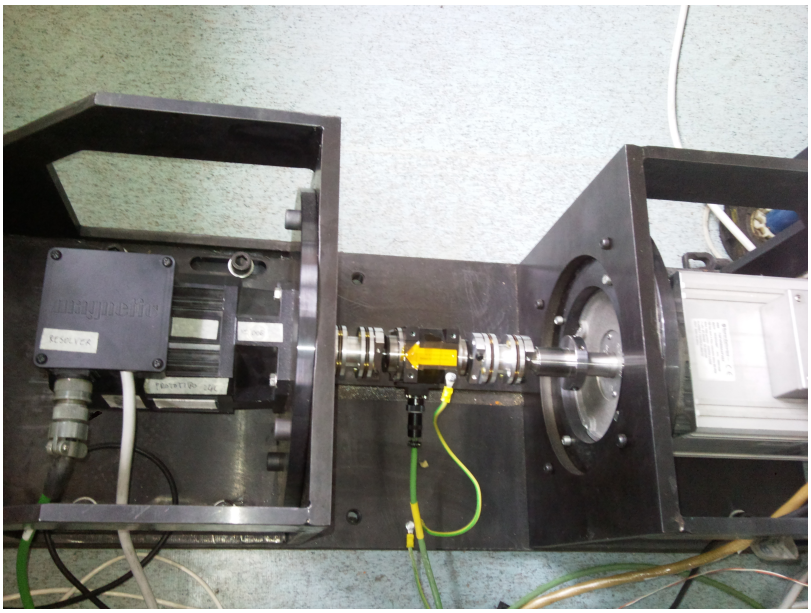

Figure 1.15: Experimental rig with two back-to-back motors and a torquemeter.

nominal region of work of the machine is split in a bunch of current magnitude values. Then, by keeping the magnitude constant, the currents i_d and i_q are changed and the output torque is measured by means of a torsiometer. The latter values are stored together with the corresponding values of i_d and i_q, which they will be used to find out the MTPA point at a specific current magnitude. The measured MTPA of the motor under test is reported in Appendix B.

2

INVERTER VOLTAGE MEASUREMENT

The pulse width modulation (PWM) voltage source inverter (VSI)s are affected by several non-idealities whose consequences on the output voltages may become unacceptable not only for open-loop drives [69] but also for closed-loop controlled drives especially when an accurate knowledge of the output voltages is required for sensorless control [45], parameters estimation [105] or predictive current control [49]. Although the additional cost and complexity of a voltage measurement system [4] could be largely acceptable thanks to the advantages that such instrument implies, a precise compensation of inverter non-idealities remains an obliged choice at least for the near future. Several on-line solutions have been proposed for compensating the effects of inverter non-idealities, such as those based on observers [55, 56, 102] waveform analysis [37, 76, 77, 114], repetitive control [10, 24]. Such techniques can be computationally intensive and do not provide adequate compensation during current transients due to their slow dynamic response. On the contrary, off-line identification procedures [22, 24, 36, 48, 78, 107] provide a good compensation also during transients and can also account for ageing effects, provided the procedure is repeated over time. The result of the off-line technique is a LUT or a polynomial used to calculate the compensation term. The latter term is added in feedforward to the calculated voltage reference for compensating the inverter non-idealities.

2.1 INVERTER NON-IDEALITIES

By introducing several simplifications and approximations, the non-linear behaviour of each inverter leg can be described by an equivalent threshold voltage [36, 48] or distortion time [22, 24] which varies according to the sign of the leg current. Power devices are considered equivalent to the series of a constant voltage source and a resistance; rise/fall times of the inverter output voltages are not included in the theoretical analysis; differences between the characteristics of power switches and free-wheeling diodes are neglected; voltage drops on power devices and turn on/off delays are supposed constant and independent from the phase current amplitudes. Although correction factors or ad-hoc profiles could be used for introducing a dependence from the phase currents [22], their choice is typically made by experience and may not match the real profiles even over time. Moreover, due to the simplicity of the obtained equations, the effects of DC bus

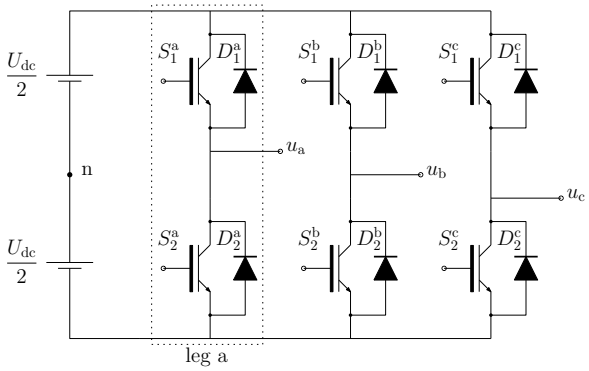

Figure 2.1: Two-level inverter scheme

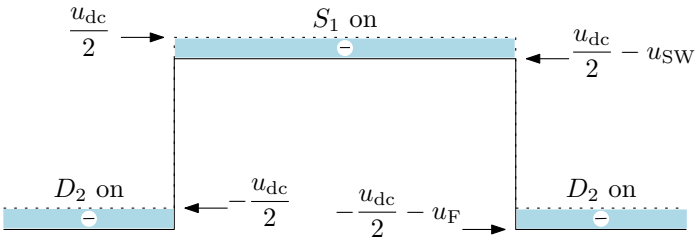

Figure 2.2: Ideal (dotted) and effective (solid) voltage u_{jn} when considering only power device voltage drops.

voltage variations on the self-commissioning procedure and on the feed-forward compensation are not considered or lost in the analysis.

Inverter non-idealities can be studied by considering the typical inverter leg j of Figure 2.1 and its output voltage u_{jn} in a sampling period T_s. In the following, only the case of two output voltage transitions per sampling period (continuous PWM) is considered. The leg current i_j is assumed positive when flowing out of the inverter and it is supposed almost constant during a T_s due to the mainly inductive nature and large electrical time constant of the load. In this section the different causes of inverter non-idealities and their effects on the output voltage will be analysed in detail. Multiple causes will be examined in the same sub-section when leading to similar effects in order to emphasize each contribute to the overall output voltage distortion.

The figures in this section report the positive current case only, where positive current is outgoing from the VSI to the load. However, the same results are obtained for negative current as well. In the description of the inverter non idealities, S_1 and S_2 are the top and bottom switches of one inverter leg respectively, Figure 2.1.

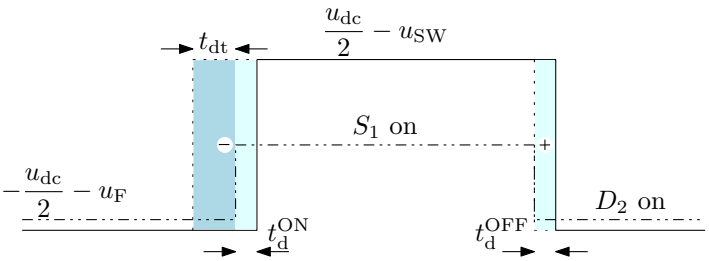

Figure 2.3: Comparison between u_{jn} as from Figure 2.2 (dotted) and effective (solid) u_{jn} when also dead time and turn on/off delays are considered. The gate signal (dashed-dotted) of the power switch taking part to current conduction is represented too.

2.1.1 *Effects of power devices voltage drops on inverter voltage levels*

Voltage drops $u_{SW}(|i_j|)$ and $u_F(|i_j|)$ shift the inverter voltage levels, as described by Figure 2.2 and by the following equation for both current directions:

$$u_{jn} = s_j \left(\frac{U_{dc}}{2} + u_{dm} \right) - \text{sign}(i_j) u_{cm} \tag{2.1}$$

where

$$u_{dm} = \frac{(u_F - u_{SW})}{2} \qquad u_{cm} = \frac{(u_F + u_{SW})}{2} \tag{2.2}$$

and $s_j = \pm 1$ depending whether S_1 or S_2 is on. It is evident from (2.1) that u_{dm} can be seen as an increment of the DC bus voltage while u_{cm} as an offset for the output voltage whose sign depends on the current direction.

2.1.2 *Effects of dead time and turn on/off delays on duty cycle*

Due to *turn on/off delays* and being $t_d^{OFF}(|i_j|) > t_d^{ON}(|i_j|)$, rising edges of each gate signal are delayed by the *dead time* T_{dt} to avoid a leg shoot-through. Figure 2.3 shows the effects of T_{dt}, t_d^{ON} and t_d^{OFF} on the output voltage. The corresponding duty cycle error can be expressed by:

$$\tilde{d}_j^{T_{dt}} = -\text{sign}(i_j) \frac{T_{dt} - (t_d^{OFF} - t_d^{ON})}{T_s} \tag{2.3}$$

Considering that $T_{dt} > t_d^{OFF} - t_d^{ON}$, a duty cycle loss happens when $i_j > 0$ and a gain when $i_j < 0$.

2.1.3 *Effects of parasitic capacitance on rise/fall times*

Parasitic capacitance $C_{par}(|i_j|)$ affects rise/fall times of u_{jn}, with the worst case occurring when a power switch is turned off at low current

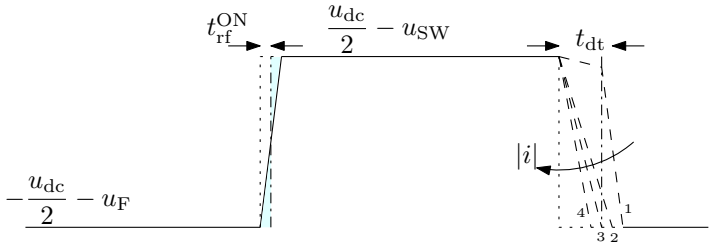

Figure 2.4: Comparison between u_{jn} as from Figure 2.3 (dotted) and distorted (solid) inverter leg output voltages due to parasitic capacitance. Four different current level cases are sketched and numbered.

levels [45, 109], as represented in Figure 2.4. At very low i_j amplitudes, the voltage transient may not be extinguished at the dead time expiration as happens in Figure 2.4c for curves 1 and 2. In this case C_{par} is then suddenly charged/discharged by the complementary switch being turned on. In case of transients caused by a power switch turn on, the resultant rise/fall time is very short and almost constant since C_{par} is charged/discharged by the large surge current provided by the switch at turn on. Despite the simplicity of Figure 2.4, real waveforms might be more complex due to other phenomena, such as the Miller effect or the diode reverse recovery time. Those phenomena have no consequences on the following mathematical description, because an equivalent area approach is used to model even such phenomena. Real u_{jn} waveforms can be replaced by area-equivalent ones whose sharp edges are opportunely delayed by $t_{rf}^{ON}(|i_j|)$ or $t_{rf}^{OFF}(|i_j|)$, depending whether the edge is caused by a power switch turn on or turn off respectively. In this way the duty cycle error due to the C_{par} is:

$$\tilde{d}_j^{C_{par}} = \text{sign}(i_j)\frac{t_{rf}^{OFF} - t_{rf}^{ON}}{T_s} \tag{2.4}$$

Considering that $t_{rf}^{OFF} > t_{rf}^{ON}$, a duty cycle loss happens when $i_j < 0$ and a gain when $i_j > 0$, a behaviour exactly opposite to the one described by (2.3). Since t_{rf}^{OFF} increases for decreasing i_j, the effect of $\tilde{d}_j^{C_{par}}$ may partially/fully compensate that of $\tilde{d}_j^{T_{dt}}$ at low current levels.

The effects of all non-idealities, in particular the parasitic capacitances, were measured on a real inverter at different current magnitude. Figure 2.5 reports the voltage outputs of one inverter leg respect to the negative rail of the DC bus. The inverter was connected to a PMSM motor. At low current magnitudes, in particular at 0.1 and 0.3 A, the voltage is still above zero even after the dead time. Then, the other switch of the leg is fired on and the voltage is suddenly dragged to zero. It is worth to highlight that the voltages in Figure 2.5 take into account all the effects described in the previous sections.

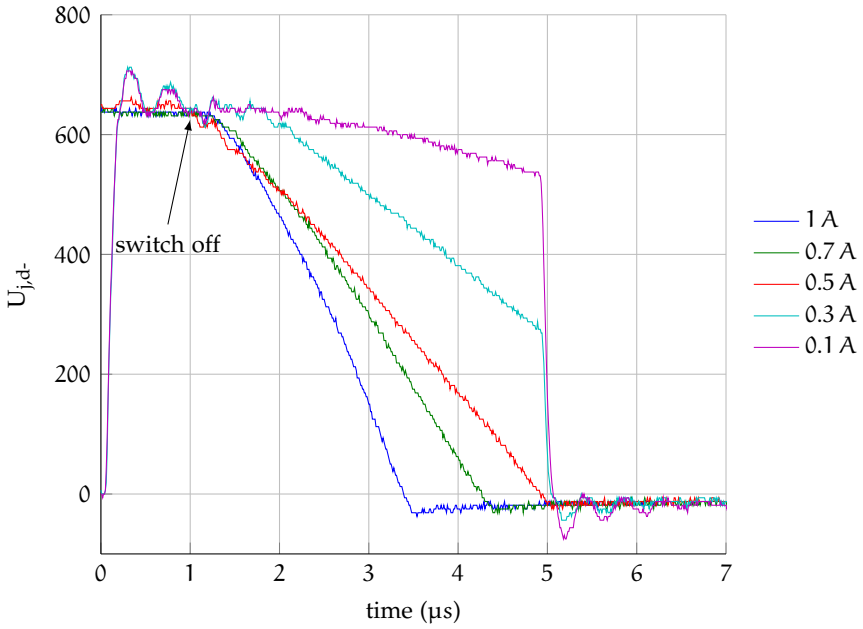

Figure 2.5: Measured output voltages of leg j respect to the negative DC rail of the inverter at different current magnitudes: $T_{dt} = 4\,\mu s$. Nominal current of the inverter is 12 A.

2.1.4 *Considerations on inverter non-idealities*

The inverter non-idealities have different effects on the voltage production depending on the current magnitude. The cross point between low and high currents is almost impossible to identify, since it depends from the inverter devices, motor resistance, cables, and so forth. Many techniques illustrated in Sect. 2.2 depend on this value, which, in turn, is found by means of empirical methods. However, it is important to draw the most salient aspects of both current regions with respect to the inverter non-idealities.

2.1.4.1 *Low current magnitude*

The low current magnitude region is the most critical one when it comes to inverter non-idealities description and, in turn, compensation. The more the current magnitude gets lower, the higher are the parasitic capacitance effects on the voltage output waveform. It is difficult to represent the inverter leg with an equivalent circuit, due to the non linearity of the involved phenomena. It is the most crucial point for a proper compensation, especially for sensorless applications [45].

2.1.4.2 *High current magnitude*

The actual values of t_d^{ON} and t_d^{OFF} are still current dependent. This means no sharp voltage output edges, but more similar to the ones in Figure 2.5. Still, most of the proposed techniques in the scientific

literature are based on the equivalent resistance representation of the term $T_{dt} - (t_d^{ON} - tdoff)$. The equivalent representation has little effects when the voltage is high. However, the equivalent representation may not be acceptable at low speeds, where the introduced error are not negligible. Thus, electric drives based on the voltage references are very affected by inverter non idealities even at high current, but at low speeds.

2.2 COMPENSATION TECHNIQUES

The choice of a suitable identification procedure plays also an important role on improving the accuracy of the resultant compensation. A commonly used procedure consists in the application of current steps along the alpha axis [22, 36, 78]. Since the non-linear behaviour of power devices strongly depends on the phase currents and because the alpha current is not equally shared among the phases, such techniques result in mixing distortions at different current levels, which are then associated to the test current level. Other techniques [31, 78, 107] allow to determine an overall V-I characteristic for inverter and load, but are unable to perfectly separate the two contributes. Usually the behaviour at high current amplitudes is supposed purely resistive and it is removed from the overall characteristic. An equivalent threshold voltage for the inverter is thus obtained. Since the real characteristic of power devices is not linear and depending on the estimated value for the equivalent series resistance, the resultant threshold voltage may exhibit not ideal behaviours such as a decreasing trend at higher current levels [78].

The average value of u_{jn} is obtained by averaging equation (2.1) over a sampling period T_s:

$$V_{jo} = \left(d_j - \frac{1}{2}\right)(U_{dc} + 2u_{dm}) - \text{sign}(i_j)u_{cm} \tag{2.5}$$

Note that d_j is the effective duty-cycle of u_{jn} as defined by:

$$d_j = d_j^* + \tilde{d}_j \tag{2.6}$$

d_j^* is the reference duty cycle and $\tilde{d}_j$ is the overall duty cycle error obtainable by summing up equations (2.3) and (2.4):

$$\tilde{d}_j = -\text{sign}(i_j)\frac{T_{dist}}{T_s} \tag{2.7}$$

where

$$T_{dist}(|i_j|) = \Delta - (t_d^{OFF} - t_d^{ON}) - (t_{rf}^{OFF} - t_{rf}^{ON}). \tag{2.8}$$

By considering (2.7) and (2.6), (2.5) becomes:

$$V_{jo} = \left[\left(d_j^* - \text{sign}(i_j)\frac{T_{dist}}{T_s}\right) - \frac{1}{2}\right](U_{dc} + 2u_{dm}) - \text{sign}(i_j)u_{cm} \tag{2.9}$$

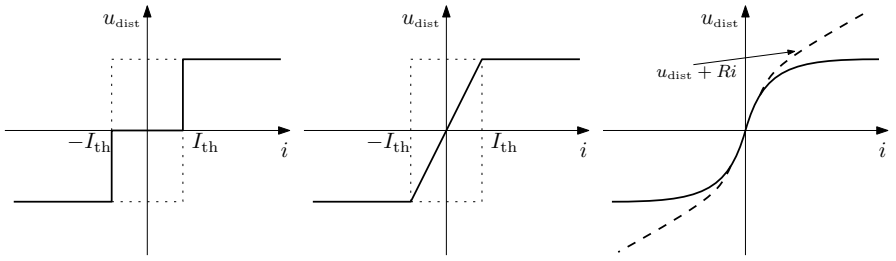

(a) Step compensation (b) Ramp compensation (c) LUT compensation

Figure 2.6: Inverter compensation techniques

It is worth noticing that T_{dist}/T_s is equivalent to an offset for the reference duty cycle, which is current sign dependent and whose effect increases with the switching frequency (smaller T_s) or when slower switches are used (larger T_{dist}). The previous equation is the one used for compensation: the desired reference phase voltage value v^*_{jn} as generated by the control is firstly assigned to the average pole voltage V_{jo} and the reference duty cycle d^*_j is then calculated and sent to the modulator.

If the compensation works properly, $V_{jo} = v^*_{jn}$ and

$$v_{no} = \frac{1}{3}\sum_j V_{jo} = \frac{1}{3}\sum_j v^*_{jn} = 0 \tag{2.10}$$

since the load is supposed wye connected, balanced and the sum of phase voltages applied to it must be always zero. In this way $v_{jn} = V_{jo} - v_{no} = v^*_{jn}$ and there is no need for any approximation when passing from pole voltages to phase voltages as in [36].

2.2.1 *Feedforward compensation techniques*

2.2.1.1 *Step compensation*

Dead time T_{dt} accounts for the biggest voltage deviation from the ideal value, since it is usually chosen considerably larger than the difference $t_d^{ON} - t_d^{OFF}$ for the sake of avoiding leg shot through. In theory, by compensating in feedforward the term $T_{dt} - (t_d^{ON} - t_d^{OFF})$ only, the equality between reference and actual voltages is re-established. The parasitic capacitance, though, strongly affects the inverter devices behaviour as the phase current gets lower. As it is shown in Sect. 2.1.3, the effect of the parasitic capacitance is to ideally compensate the average loss voltage due to dead time. Thus, a rough compensation of dead time effects is to compensate in feedforward the quantity:

$$u_{comp} = T_{dt} - (t_d^{ON} - t_d^{OFF}), \tag{2.11}$$

depending on the phase current sign and the current magnitude. That is, below a certain current level in magnitude, the compensation is

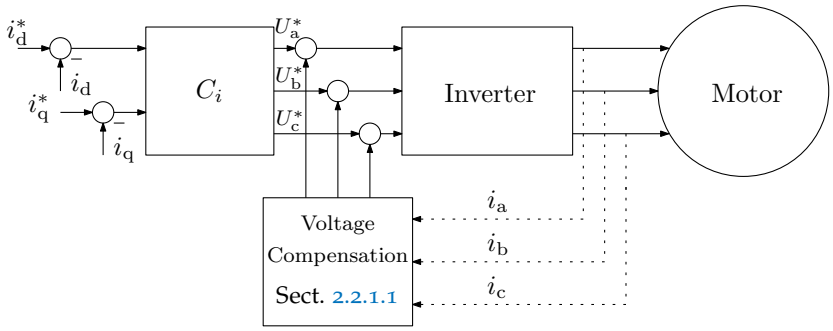

Figure 2.7: Feedforward based compensation scheme

switched off. The compensation strategy, called *step compensation*, is sketched out in Figure 2.6a, while a simple scheme of feedforaward based compensation techniques is reported in Figure 2.7. The current I_{th} represents the current level at which the compensation is switched off. Its magnitude is determined by trial and error tests.

2.2.1.2 *Ramp compensation*

An improvement of the step compensation technique is the *ramp compensation* presented in [50]. The parasitic capacitance do not entirely compensate for the dead time at small current magnitude. Thus, there is no proper compensation at low current magnitude. A representation of the compensation strategy is reported in Figure 2.6b. The ramp compensation simply adds a term proportional to the actual current magnitude. The current magnitude I_{th} is decided by means of trial and error tests, as for the step compensation. The results reported in [50] show the superior benefits for sensorless drives applications.

2.2.1.3 *LUT based compensation*

The third technique, reported in Figure 2.6c, is based on an identification procedure which is carried out off-line. The same procedure allows to estimate the stator resistance too. The technique is reported, in various forms, in many pubblications [9, 78, 82]. The following assumptions are made before going into details of the identification procedure:

- only DC current are considered;
- the load is a three phase balanced motor;
- at high current magnitude, inverter non-idealities are resistance like;
- the estimated stator resistance accounts for connections and cables too.

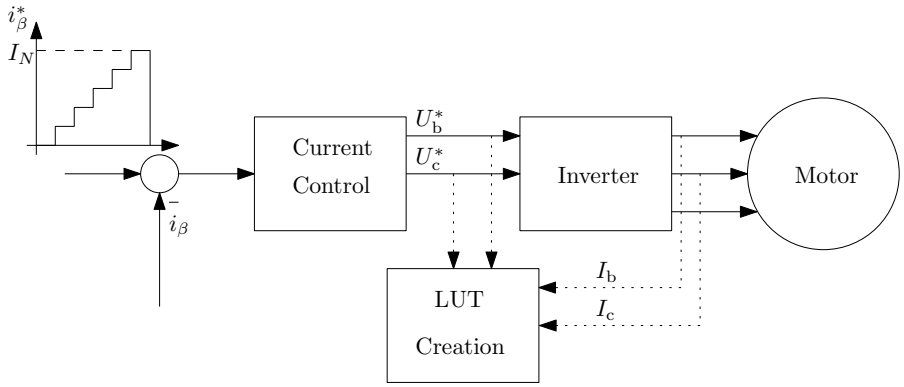

Figure 2.8: Experiment scheme for inverter non-idealities identification procedure

A step decreasing/increasing current vector $\mathbf{i} = Ie^{j\vartheta}$ is applied to the connected motor. The angle ϑ should be set such that only two phases are conducting. In this way, the inverter non idealities effects are the same on both inverter legs and the procedure encompasses homogeneous voltage distortion quantities. For instance, by imposing only i_β such condition is satisfied. The current control can be roughly tuned, since only the steady state condition is important in the procedure. Once the correct current vector amplitude is settled, the voltage reference U^*_β is stored into a LUT. At the end of the procedure, the LUT of the voltage references contains the actual voltage references U^*_β necessary to obtain the desired current steps.

A result from an experimental test is reported in Figure 2.9. It is worth to note that at high current the voltage behaviour is linear, typical of a pure resistive load, whereas at low current the behaviour is far from linear. A magnification of the low current region is reported in Figure 2.10. It is interesting to note that from left to right, from point *A* on, the voltage reference U^*_β differs of a constant value from the ideal one RI_β. The difference is due only to the term $T_{dt} - (t_d^{ON} - t_d^{OFF})$, which is supposed to be constant. Therefore, it is possible to estimate the resistance R which encompasses the stator resistance and all connections. The estimation problem can be solved with an ordinary least square (OLS) algorithm. The relationship $U^*_\beta = RI_\beta$ is supposed linear from i_{th} till the nominal current value and it is used as a regression model. The parameter R is the unknown coefficient[1]. The estimation problem is solved by the following equation:

$$R = \frac{\sum_{k=1}^{N} (U^*_\beta(k) - U^*_{avg})(I_\beta(k) - I_{avg})}{\sum_{k=1}^{N} (I_\beta(k) - I_{avg})^2} \tag{2.12}$$

1 The accent ˆ is omitted in this case since there is no chance of mixing up parameters with estimates.

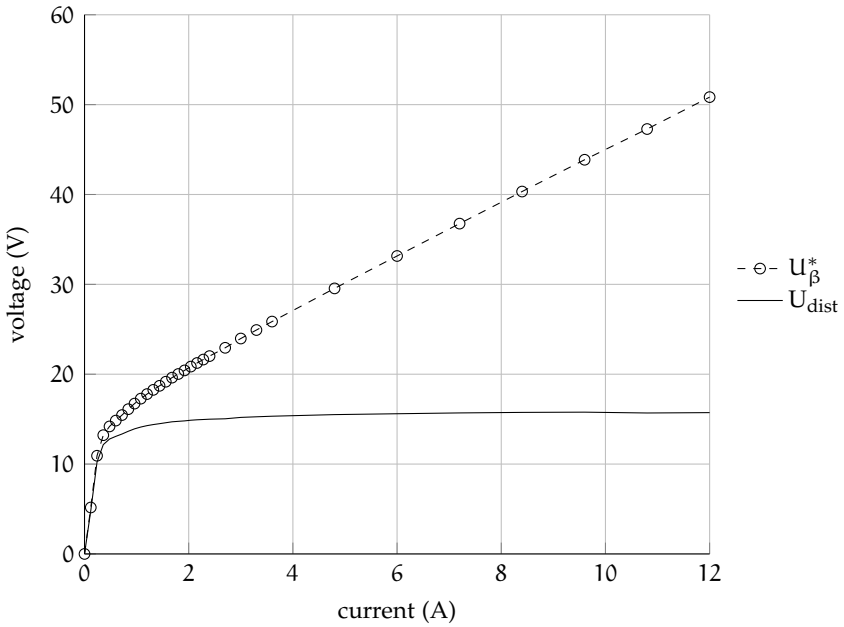

Figure 2.9: Voltage u^*_β recorded from the identification experiment of Figure 2.8 and the calculated voltage distortion u_{dist} due to inverter non-idealities used for the LUT compensation

where $U^*_{avg} = \frac{1}{N}\sum_{k=1}^{N} U^*_\beta(k)$ and $I_{avg} = \frac{1}{N}\sum_{k=1}^{N} I_\beta(k)$ are the average of the last N samples of voltage and current respectively.

The differences between the ideal resistive voltage drop RI_β and the actual voltage reference curve (dashed curve) of Figure 2.10 can be calculated and used to compensate the inverter non-idealities voltage distortion. The result is the solid curve U_{dist} in Figure 2.9.

2.2.2 *An innovative technique*

In this thesis, a new identification technique is proposed. The aim of the identification procedure described in the following subsections is to estimate T_{dist} in (2.8), u_{dm} and u_{cm} in (2.2) at various DC current levels for generating LUTs. Alternatively, the estimated values can be used for calculating the coefficients of a polynomial approximation suitable for the particular non-linear characteristic. However the first approach has been preferred since it is less computationally intensive. A PI regulator, whose output is in the form of a reference duty cycle d^*, is used to establish the flow of the desired DC current from leg j to leg k while the gate signals of the remaining leg are kept inactive to prevent any flow of current through it. In this way legs j and k, their power devices and free-wheeling diodes carry the same current and so only distortions at the same current level are measured.

In order to make the procedure independent from the load resistance and insensitive to DC bus voltage variations, T_{dist}, u_{dm} and u_{cm} are obtained by comparing the results of two different tests per-

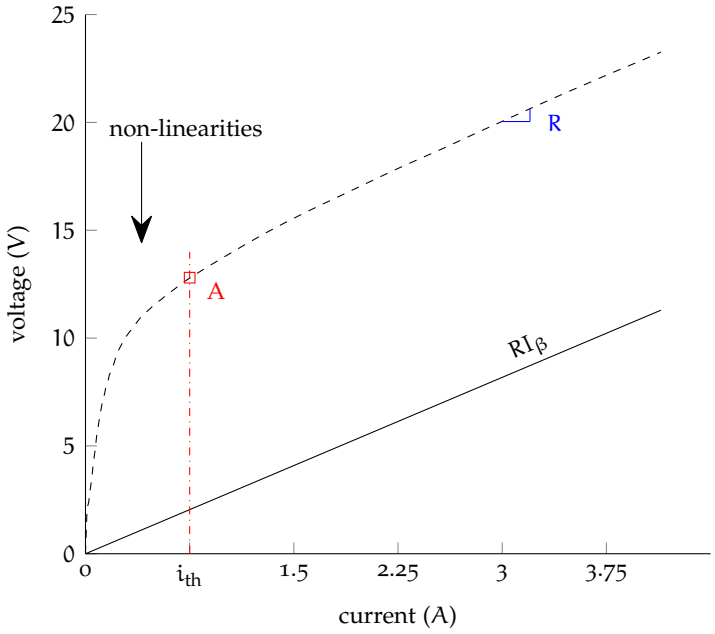

Figure 2.10: Magnification of the low current magnitude region of Figure 2.9

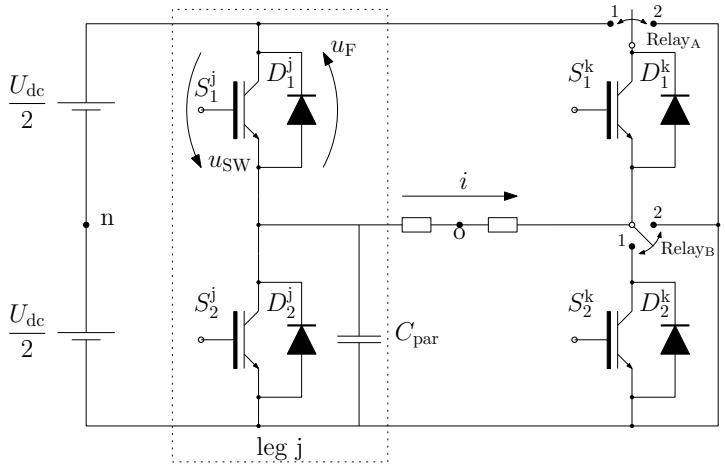

Figure 2.11: Typical inverter leg j connected to a wye-connected load and modified leg k as required by the proposed identification procedure.

Table 2.1: Relays and legs gate status during the tests

$Relay_A$	$Relay_B$	d_j^*	d_k^*	Test
1	1	$0.5 + 0.5d^*$	$0.5 - 0.5d^*$	Test 1
1	1	d^*	0	Test 2
2	1	d^*	-1[a]	Test 3
1	2	d^*	-1[a]	Test 4

[a] Both switches of the leg are disabled.

formed at the same current level. Since an inverter in its typical configuration cannot perform the required four linearly independent tests, two relays are added only to leg k as shown in Figure 2.11. The reference duty cycles applied to leg j and k and the state of the two relays during the four tests are listed in Table 2.1. For understanding the correspondence between the state of each relay and its contact configuration, refer to Figure 2.11. Configuration of leg k is modified only at zero leg current and in any case never during the normal operation of the drive. Therefore the relay switching specifications are not demanding so that, whilst they must be rated for the rated inverted current and DC link voltage, the additional cost is low. Moreover relays are usually cheaper and reliable than a voltage measurement system, at least for small currents (order of few decades). This solution is applicable not only in case of VSIs made of discrete components, but also when power devices are integrated and packaged in modules since versions with low-side devices not connected to the DC bus rail are widely available in the market for allowing the use of shunt resistors in place of the costly effect-hall current sensors.

2.2.2.1 *Determination of* T_{dist}

Test 1 and Test 2 of Table 2.1 are required to measure T_{dist} at a given current level. During Test 1, both legs j and k are modulated while during Test 2 only leg j is modulated since the power switch S_4 of leg k is continuously kept on. Leg k is maintained in its typical configuration by leaving the relays unexcited in position 1 of Figure 2.11. From (2.9), applied to legs j and k, it is easy to calculate the voltage applied to the load during each test:

$$V_{jk}^{(1)} = \left(d_j^{*(1)} - d_k^{*(1)} - 2\frac{T_{dist}}{T_s} \right) (U_{dc} + 2u_{dm}) - 2u_{cm} \tag{2.13}$$

$$V_{jk}^{(2)} = \left(d_j^{*(2)} - \frac{T_{dist}}{T_s} - \frac{1}{2} \right) (U_{dc} + 2u_{dm}) - u_{cm} - u_{SW} + \frac{U_{dc}}{2} \tag{2.14}$$

Assuming the load resistance and the DC bus voltage constant during the two tests, the voltage applied to the load should be the same for the same current level. By equating the above equations, it is possible to obtain without neglecting any term:

$$\frac{T_{dist}}{T_s} = d_j^{*(1)} - d_k^{*(1)} - d_j^{*(2)} = d^{*(1)} - d^{*(2)} \tag{2.15}$$

where quantities of Table 2.1 have been used.

2.2.2.2 *Determination of* u_{dm}

Test 2 and Test 3 are used in this case. During Test 3, leg k is disabled by keeping its gate signal inactive and diode D_3 is disconnected from the upper DC bus rail and connected to the lower one by moving the contact of $Relay_A$ to position 2. In this way it is possible to obtain a continuous current flow through D_3 (not possible otherwise). Equations (2.9) and (2.1) cannot be applied in this case to leg k since its configuration has been changed. In this configuration, leg k degenerates to D_3 connected to the lower DC bus rail and from Figure 2.11 it is easy to deduce that:

$$V_{ko}^{(3)} = -\frac{U_{dc}}{2} + u_F \tag{2.16}$$

Hence, from (2.9) applied to leg j and from (2.16), the voltage applied to the load during Test 3 is:

$$V_{jk}^{(3)} = \left(d_j^{*(3)} - \frac{T_{dist}}{T_s} - \frac{1}{2}\right)(U_{dc} + 2u_{dm}) - u_{cm} - u_F + \frac{U_{dc}}{2} \tag{2.17}$$

Again, by equating (2.14) with (2.17):

$$u_{dm} = \frac{d_j^{*(3)} - d_j^{*(2)}}{1 - \left(d_j^{*(3)} - d_j^{*(2)}\right)} \frac{U_{dc}}{2} \tag{2.18}$$

2.2.2.3 *Determination of* u_{cm}

Test 3 and Test 4 are required in this case. During Test 4, leg k is kept disabled and its output is connected to the lower DC bus rail by means of $Relay_B$, whose contact is moved to position 2. In this way it is possible to bypass any voltage drop due to power devices. In this configuration, leg k degenerates to a direct connection with the lower DC bus rail and so it is easy to deduce that the output voltage of leg k is:

$$U_{ko}^{(4)} = -\frac{U_{dc}}{2} \tag{2.19}$$

Applying (2.9) to leg j and from (2.19), the voltage applied to the load during Test 4 is:

$$U_{jk}^{(4)} = \left(d_j^{*(4)} - \frac{T_{dist}}{T_s} - \frac{1}{2}\right)(U_{dc} + 2u_{dm}) - u_{cm} + \frac{U_{dc}}{2} \tag{2.20}$$

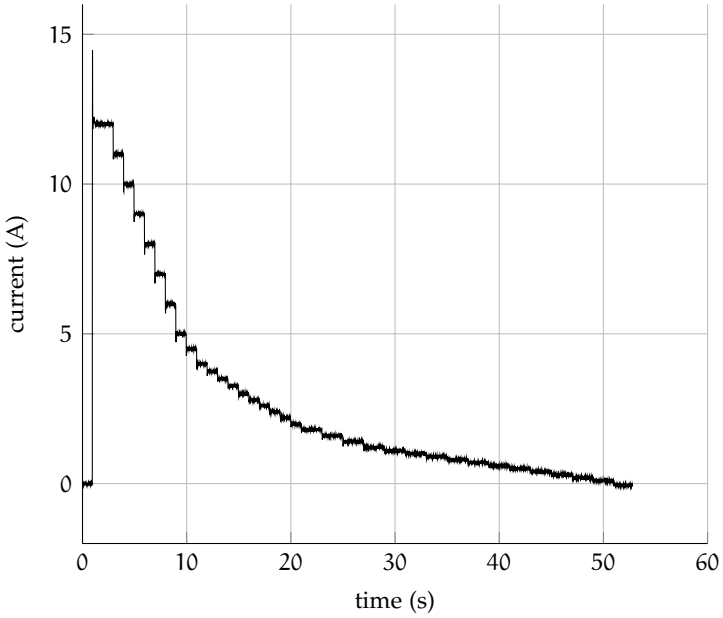

Figure 2.12: Staircase current ramp used for LUTs generation.

By equating (2.17) with (2.20) and by using (2.18) it results:

$$u_{cm} = \frac{(d_j^{*(3)} - d_j^{*(4)}) - \frac{1}{2}(d_j^{*(3)} - d_j^{*(2)})}{1 - (d_j^{*(3)} - d_j^{*(2)})} U_{dc} \tag{2.21}$$

2.2.2.4 *Experimental Results*

The proposed identification procedure was tested on an experimental three-phase system composed by a Semikron SemiTeach insulate gate bipolar transistor (IGBT) inverter, modified for the purpose, and by an asynchronous motor whose stator resistance and inductance are $R = 1.3\,\Omega$ and $L = 33\,mH$. Algorithms were implemented on a TMS320C6713 floating-point DSP while PWM, phase current acquisition and other auxiliary services on an A3P400 FPGA.

All the tests for the identification procedure were executed at a sampling frequency $F_s = 1\,kHz$ for reasons explained later in Sect. 2.2.2.5. In order to minimise the number of required configuration changes, tests of Table 2.1 were executed sequentially at every current level of the staircase current ramp represented in Figure 2.12. Current range was limited to 0-12 A and step sizes have been reduced for current below 2 A to obtain more steps and so more estimates for T_{dist}, u_{dm} and u_{cm} where the inverter behaviour is expected to be highly non-linear.

Experimental characteristics of T_{dist}, for dead-times equal to 2, 3 and 4 µs, are reported in Figure 2.13. The variation of T_{dist} when different DC bus voltages are used during the identification procedure is represented in Figure 2.14 for $\Delta = 2\,\mu s$. Differences are concentrated at low current levels, indicating that the parasitic capacitance and so

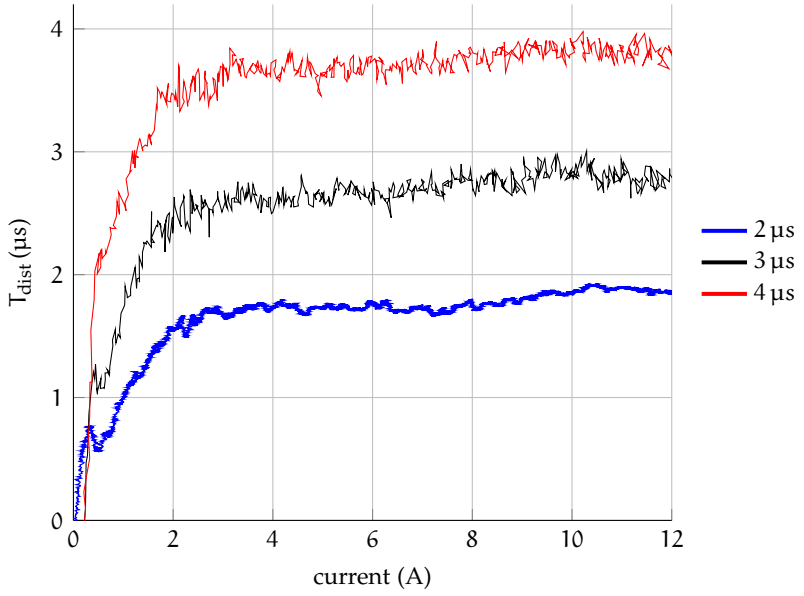

Figure 2.13: T_{dist} obtained with linear current ramps for different dead times T_{dt}.

t_{rf}^{OFF} and t_{rf}^{ON} are more affected than t_d^{ON} and t_d^{OFF}. From the same figure it can be also noticed that variations of the DC bus voltage within a few tens of Volts, as expected during the normal operation of a typical drive, have negligible effects on T_{dist}. If robustness to large DC bus voltage variations is desired, the proposed identification procedure must be repeated at different DC bus voltages in order to generate LUTs covering the expected DC bus voltage operating range. It can be easily done in applications with a regulated DC bus voltage. Alternatively, in case of applications with an unregulated DC bus, the LUTs can be saved in the non-volatile memory of the drive during production even though in this last case the end user would not be able to repeat the identification.

Experimental results show that characteristics for u_{SW} and u_F, Figure 2.15, u_{dm} and u_{cm}, Figure 2.16, are insensitive to dead time and DC bus voltage variations, as theoretically expected. In particular, the u_{SW} and u_F characteristics can be derived from (2.18) and (2.21) considering their definition in (2.2).

In order to evaluate the effectiveness of the proposed identification procedure, a test in the $\alpha\beta$ reference frame was carried out by imposing a rotating reference current vector at a very low frequency, $f = 0.1$ Hz. Under these conditions, the motor behaviour is purely resistive and the quality of the resultant compensation is indicated by how the reference voltages u_α^* and u_β^* are similar to sinusoidal signals. The results obtained for a sinusoidal current reference of 10 A peak amplitude, and a sampling frequency F_s equal to 8 and 10 kHz, are shown in Figure 2.17 and 2.18 respectively. The residual visible

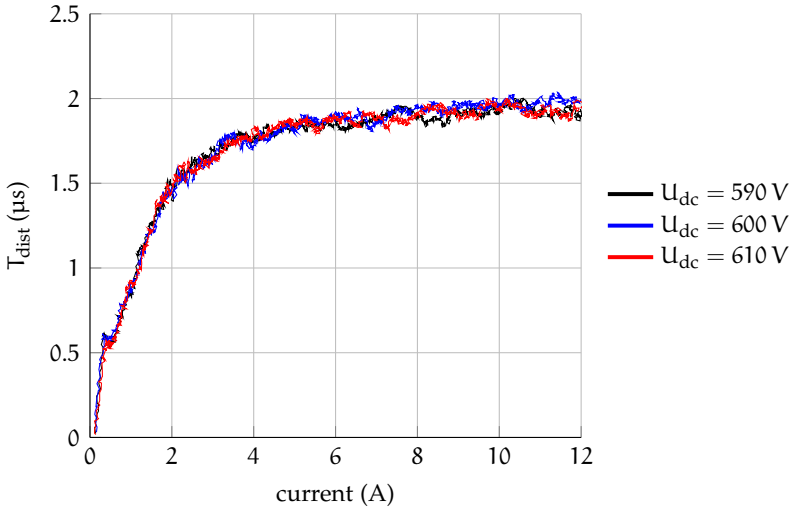

Figure 2.14: T_{dist} obtained with linear current ramps at different U_{dc}.

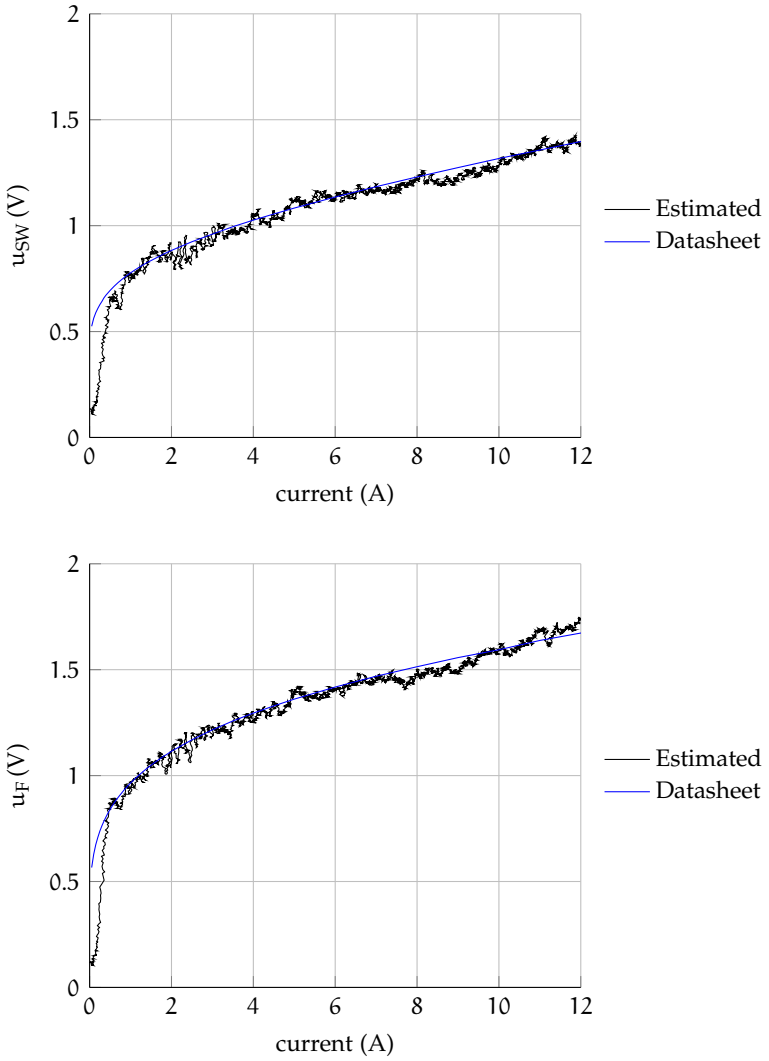

Figure 2.15: Experimental components characteristics u_{SW} and u_F obtained with linear current ramp.

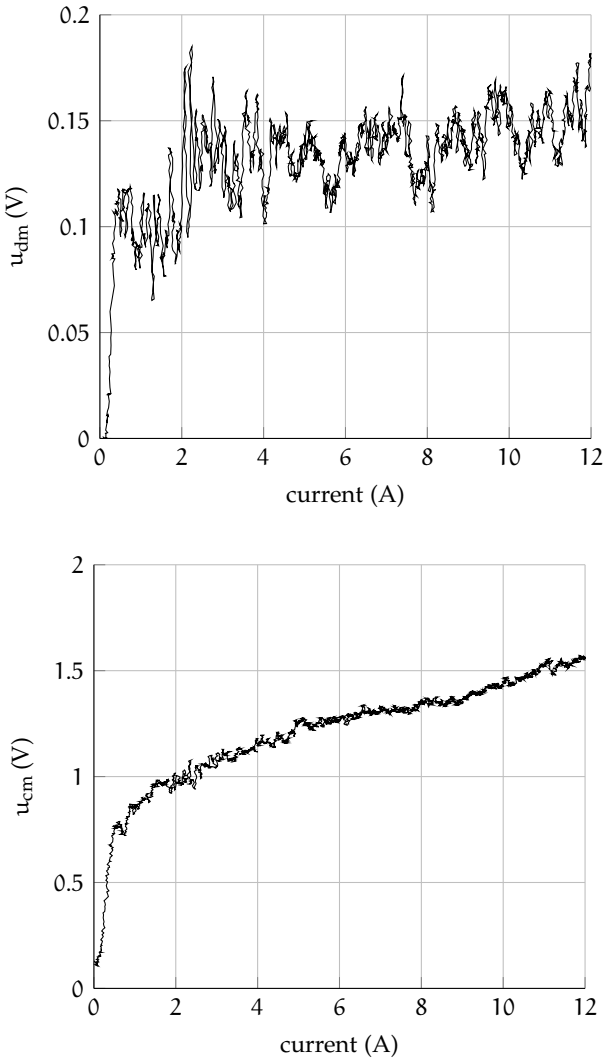

Figure 2.16: Experimental results of u_{dm} and u_{cm} obtained with linear current ramp.

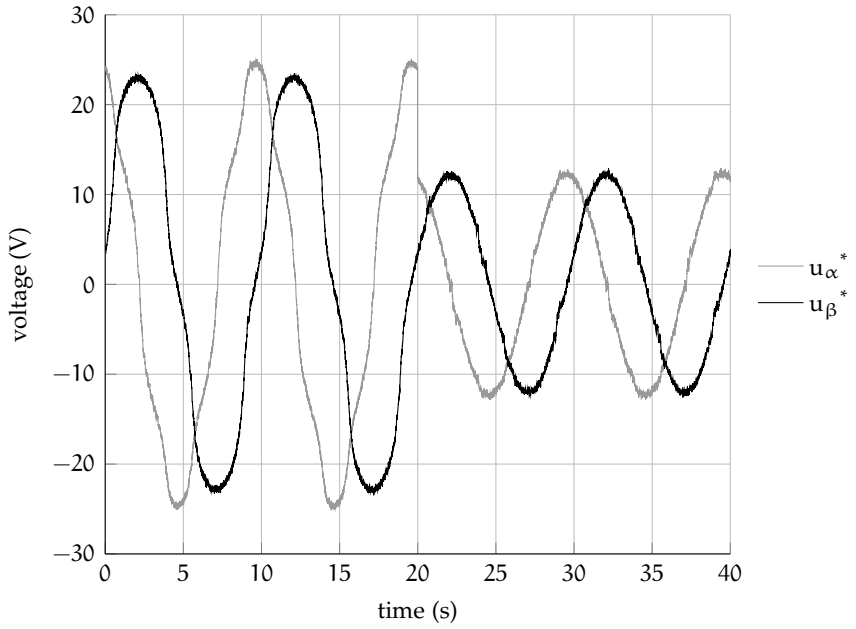

Figure 2.17: Reference voltages u_α^* and u_β^* before and after activation of the proposed compensation for a 0.1 Hz rotating reference current vector at 8 kHz of PWM

distortions are mainly due to the zero-current clamping and to the difficulties on performing an accurate identification at low current levels described in Sect. 2.2.2.5. The higher distortion in the test performed with F_s = 10 kHz is explained by the fact that the zero-current clamping is more effective at higher switching frequencies due to the higher ratio between T_{dt} and T_s.

2.2.2.5 *Pulse dropping at low current amplitudes*

During the second, third and fourth tests of Table 2.1, the output of leg k is connected to the lower DC bus rail by means of S_4, D_3 or $Relay_B$. Being the procedure executed at stand-still, the reference duty cycle applied to leg j is very small. In fact, according to (2.5), d^* accounts for only the voltage drops due to T_{dist}, u_{dm} and u_{cm} as well as the voltage drop over the load resistance which is usually kept low by design. For current amplitudes below a specific threshold, which depends on T_{dt}, T_s and the power devices voltage drops, d_j^* may become less than $\frac{\Delta}{T_s}$. When the previous condition is satisfied, pulses are dropped. Whenever $d_j^* > 1 - \frac{T_{dt}}{T_s}$ or $d_j^* < \frac{\Delta}{T_s}$, d_j^* is saturated to $d_j^* = 1$ or $d_j^* = 0$ to prevent pulses shorter than T_{dt} from appearing at the inverter output [108]. So this distortion occurs when operating at the limits of the inverter voltage capability. It can be compensated by adding a suitable zero component to all reference duty cycles when one of them approaches the previously described boundaries. This approach is automatically used by the space vector modulation (SVM).

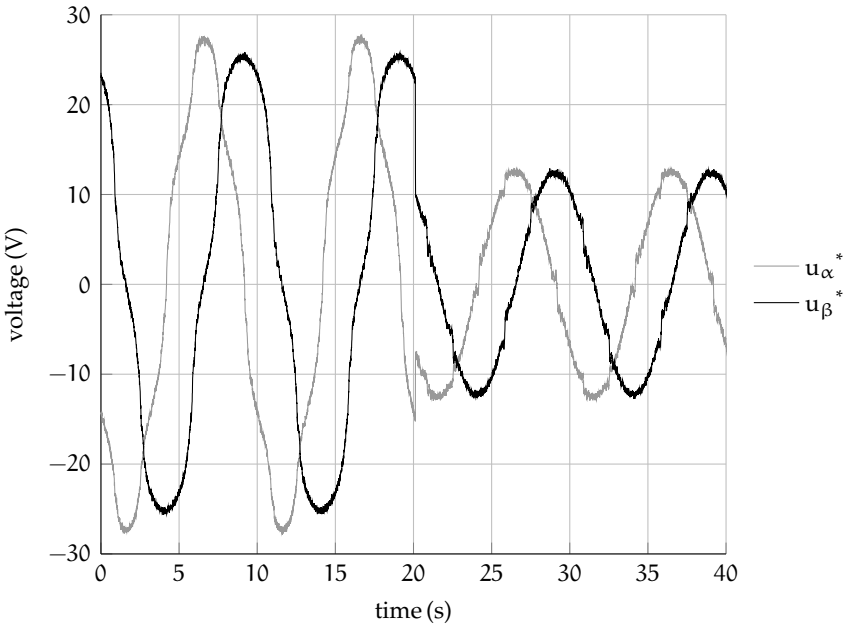

Figure 2.18: Reference voltages u_α^* and u_β^* before and after activation of the proposed compensation for a 0.1 Hz rotating reference current vector at 10 kHz of PWM

With the described experimental setup, F_s = 10 kHz and $\Delta = 2\,\mu s$, pulse dropping is effective for currents below 2 A. By taking into consideration that the T_{dist}, u_{dm} and u_{cm} do not depend on F_s, the tests have been carried out at $F_s = 1$ kHz to overcome the aforementioned problem. At $F_s = 1$ kHz, pulse dropping starts at around 0.2 A. On the other hand, reducing the DC bus voltage during the identification procedure to increase d^* is an impracticable solution because it would modify t_d^{OFF}, t_d^{ON}, t_{rf}^{OFF}, t_{rf}^{ON} and hence T_{dist} in a non-linear way, making the obtained results of no practical use when the nominal DC bus voltage is restored.

2.3 VOLTAGE MEASUREMENT IN AC DRIVES

Position and speed estimation in modern sensorless drives is typically performed with a state observer, driven by the measurements of the phase currents and voltages that actually feed the electric machine. For an accurate estimation, high quality measurements are obviously required. Unfortunately, conventional drives are traditionally equipped only with current sensors, that are used for current control and failure detection purposes. In principle, in a perfectly compensated inverter, the lack of a direct phase voltage measurement can be circumvented by simply using the phase voltage references in place of their measurements. In practice, however, the inverter non-idealities are various and highly device-dependent, Sect. 2.2, and compensa-

tion techniques show their weakness especially at low phase currents and voltages [35], Sect. 2.2.2.4.

Accuracy can be undoubtedly enhanced by resorting to a direct measurement scheme. The main challenge in such approach is the extraction of the average voltages out of the PWM voltages applied to the motor phases. Low pass filtering of the PWM signals can be potentially exploited for the purpose, but this introduces a phase lag that could affect the measurement accuracy of any non-constant signal. The phase lag issue can be overcome by computing the average voltage directly within each PWM period, by using either analog [8, 95] or digital methods [81]. In the former ones, the average value of the pulse voltage within each PWM period is determined with an analog integrator, which is reset at the end of each period; in the latter methods, instead, the average voltages are obtained by oversampling the PWM signals with A/D converters, whose outputs are integrated by a FPGA-based integrator. An analog measurement system can be easier to implement, but its operation is affected by components tolerance and ageing; on the contrary, digital methods are inherently more accurate, linear and less sensitive to components variations.

The architecture of a digital measurement system invariably includes an attenuation stage, typically based on a passive voltage divider, followed by an analog-to-digital converter (ADC) and an FPGA unit for fast digital processing. Either the inverter phase (i.e. phase-to-neutral) or line (i.e. phase-to-phase) voltages can be measured. For a Y-connected load, the former option allows to determine the neutral voltage displacement in a balanced load; on the other hand, for a Δ-connected load, with the latter option it is possible to measure the actual voltages applied to each leg of the connection. An undisputed advantage of the phase-to-phase measurement is that only two voltages need to be measured, since the third is obtained as the opposite of the sum of the first twos. This aspect obviously enables the reduction of both costs and complexity of the circuit implementation, thus making the solution more attractive from an industrial perspective. Unless the determination of the neutral voltage displacement in a (balanced) Y load is of utmost importance for a specific application, the solution based on the measurement of the phase-to-phase voltages is usually preferred.

A possible implementation of an FPGA-based system for the phase-to-phase voltages measurement of a three-phase inverter has been initially proposed in [81]. The implementation is presented in Sect. 2.3.1. The measurement accuracy is considered in Sect. 2.3.2.

2.3.1 *Voltage measurement board*

The block schematic of the voltage measurement system is reported in Figure 2.19. Only one voltage measurement is reported in Figure 2.19

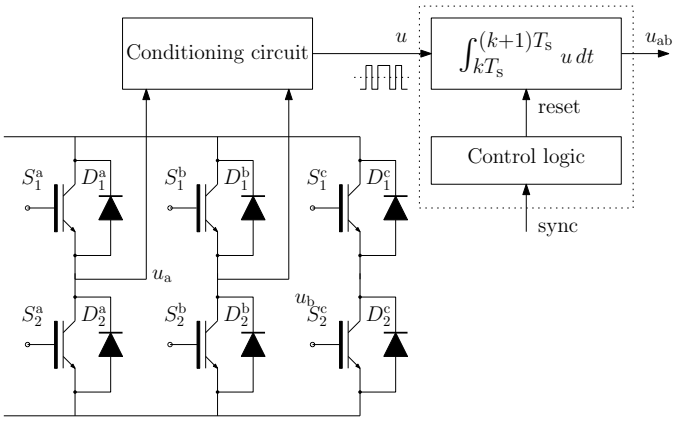

Figure 2.19: Block schematic of the u_{ab} voltage measurement

for the sake of better explanation. In the following, only one voltage measurement is considered. The voltage measurement board is divided in three parts:

- conditioning circuit;
- integral block;
- control logic.

The integral block and the control logic can be either analog or digital. In this thesis, the digital solution was selected and implemented. This section aims at highlighting the most important choices in the voltage measurement board design. The schematic design and implementation aspects are out of scope in this work. The final prototype was printed on a 4 layer printed circuit board (PCB), Figure 2.20.

The conditioning circuit is, in turn, an attenuation stage, which has to be carefully designed. An insight of its structure is reported in Figure 2.21. The attenuation stage has no active stage and, thus, it can be made of only resistance. In order to reduce voltage measurement errors, the resistances should have a very little tolerance[2]. The ratio $1 : n$ should be selected considering the worst case scenario, i.e. the highest voltage magnitude for the desired application. An operational amplifier is used to calculate the phase-to-phase voltage, whose output is single ended. The following block, i.e. the differential stage, is necessary to get a differential signal which is required by the implemented ADC for better signal-to-noise ratio. The latter also provides a voltage reference for the differential signal generation.

The integral computation is carried out by software. For very fast computation, an FPGA was adopted. The FPGA gathers the samples from the ADC with a selected sampling frequency F_m. The sampling frequency value directly affects the measurement accuracy, as discussed later in Sect. 2.3.2. The FPGA software is actually rather simple,

2 Resistances with tolerance of 0.1% are implemented in the laboratory prototype

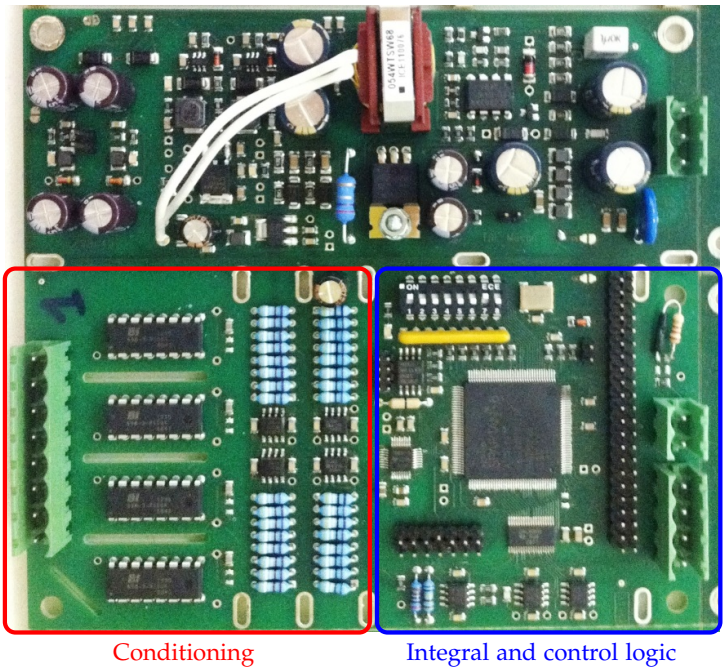

Figure 2.20: Voltage measurement board prototype

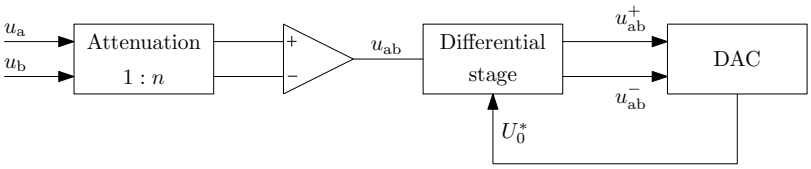

Figure 2.21: Block scheme of the conditioning circuit

since the necessary operations to emulate the integrator are N_s accumulation over a PWM period and a division at the end of each period. It is worth to highlight that whether a fixed PWM frequency is considered, the last division can be substituted by a multiplication for a constant term, gaining in speed computation. For the sake of generality, the software can be easily written considering a wide span of PWM frequency ranges. The accumulator buffers are designed considering a fixed F_m and the lowest PWM frequency. The accumulators are reset by a proper synch signal. The synch is generated by the built-in PWM generator inside the voltage inverter. The division algorithm should be designed as soon as the synch signals fires up. For instance, an algorithm suitable for FPGA implementation is the *long-hand division*, which needs N_s FPGA cycles to work out the operation.

The control logic is a complete software block. It is the part of the software which masters all operations:

- readings from the ADC;
- integral algorith start and stop;
- handling the sync signal;
- output of the final results on digital-to-analog converter (DAC) or other peripherals.

Its description is out of the scope of this section, since it is just a designer choice.

2.3.2 *Measurement accuracy*

In a digital measurement system, the accuracy depends mainly on the components tolerance, the sampling process and the A/D conversion. When measuring a PWM signal, the largest contribution to the overall measurement uncertainty is typically due to the sampling process. In fact, suppose to measure the average voltage $U = U_{dc} \cdot D$ of a PWM pulse with amplitude U_{dc} and duty cycle $D = T_{ON}/T_s$ by collecting N_s samples over a PWM period. The largest measurement error occurs either when a sample is acquired immediately before the pulse rising edge, Figure 2.22a, or immediately after the falling edge, Figure 2.22b. In both cases, the absolute measurement error is equal to

$$\Delta V = U_{dc} \times \left(\frac{T_m}{T_s}\right) = \frac{U_{dc}}{N_s} \tag{2.22}$$

where $T_m = T_s/N_s$ represents the sampling period. It is indeed an error below the actual average voltage $V = U_{dc} \times D$ in the former case, and vice versa in the latter case. Note that the absolute error increases with the pulse amplitude U_{dc} (i.e. the DC bus voltage), and decreases with the oversampling factor N_s.

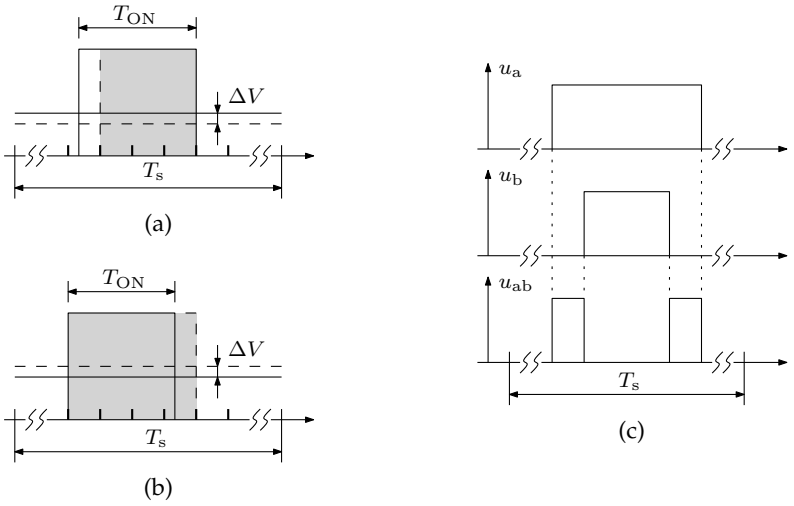

Figure 2.22: Average voltage measurement of a PWM pulse with a digital method. (a) Measurement error from below. (b) Measurement error from above. (c) Measurement of a phase-to-phase PWM voltage.

From the expression of the relative error

$$\frac{\Delta V}{V} = \frac{1}{D \times N_s} \tag{2.23}$$

it can be noticed that the measurement accuracy deteriorates as the duty cycle D tends to zero, i.e. when the average value to be measured is low, compared to the DC bus voltage. This is the main drawback of the digital measurement approach. The measurement accuracy is even worst when measuring a phase-to-phase voltage, Figure 2.22c. In fact, in this case the signal to be measured may have twice the edges of a single PWM pulse, which implies a doubling of both the absolute and relative measurement errors (2.22)-(2.23). The only way to improve the measurement accuracy of a PWM signal remains that of increasing the oversampling factor N_s, but this inevitably requires the use of faster, and hence more expensive, A/D converters. As a final note, it is worth to point out that when the voltage to be measured is a constant, instead of a PWM signal, the sampling process does not introduce any uncertainty, and the measurement accuracy is only limited by the component tolerances and the A/D conversion.

3

PARAMETER IDENTIFICATION OF PMSM

Several motor models of the synchronous PM machine have been reported in Chapter 1. Evidences in the scientific literature have shown that the magnetic motor model is of utmost importance for the drive performances [12, 15, 20, 46]. Therefore, researchers have put a lot of emphasis on elaborating complex and meaningful models for electric drives. The reasons for that are manifold. Accurate motor models enable to get:

- accurate real-time torque estimation;
- check of the machine sensorless capability;
- fine design of observers for position estimation, predictive control and so forth;
- MTPA accurate detection.

It is not seldom to find tailor made applications in which the PM motor has been specifically designed. For instance, washing machines as well as automotive applications need motors with wide operating range, guaranteeing high torque at low speeds and enhanced operations in flux weakening region.

Electrical and magnetic parameter identification can be grouped into two categories:

- off-line techniques [72, 83, 104];
- on-line techniques [70, 110–112].

The magnetic fluxes characteristics are usually *static*, i.e. they do not change so much during motor operations due to temperature or other effects. For the latter reason, magnetic fluxes characteristics are estimated with techniques that belongs to the former group. Other parameters, in particular the stator resistance, are estimated off-line just to have at least an initial value. The latter group is made up by estimation techniques for parameters that changes with the motor operations, such as stator resistance and PM flux linkage. Some parameters, such as the mechanical ones, are preferable to get estimated on-line, especially in presence of variable loads.

3.1 ELECTRICAL PARAMETERS

The electrical parameters that characterise the motor model are defined in (1.14). They are:

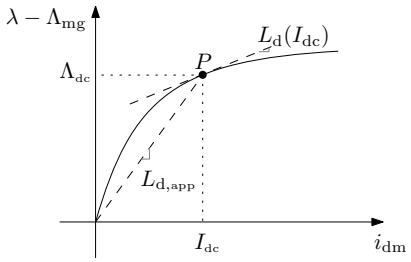

Figure 3.1: Graphical interpretation of L_d and L_{app}.

- stator resistance R;
- inductances L_d and L_q;
- PM flux linkage Λ_{mg}.

The inductances values vary with the motor type, i.e. with the rotor structure. For anisotropic motors, magnetic saturation must be taken into account, for instance by means of the incremental inductance in Sect. 1.1.5, or by accurate FEA analysis, Sect. 1.2.

3.1.1 *Direct-axis inductance estimation*

The direct-axis inductance L_d can be estimated by considering it as an incremental inductance [33]. The measurements are performed at standstill, which implies that dq reference frame coincides with the stationary α-β one. The general PM synchronous motor voltage balance equation for the d-axis, at null speed, is the first of (1.20). In the following, the saturation is ascribed to the *flux-producing* current i_{dm}, which is a part of the d-axis current, as it will be clearer later on. The cross-saturation will be neglected, because of the experimental evidences of its little influence within the operating range of the IPM drive available in the laboratory premises.

A graphical interpretation of the apparent and instantaneous inductances is reported in Figure 3.1. The instantaneous inductance L_d represents the actual inductance around a predefined working point $P = (I_{dc}, \Lambda_{dc})$ and it expresses the derivative $d\lambda_d/di_{dm}$ of the flux linkage with respect to the current in P.

The measurement technique imposes a multi-sinusoidal i_d current, on a prefixed bias current I_{dc}. It is worth to note that the related alternating field induces iron losses that may alter the measurements, if not properly considered. Several proposals for the drives-oriented iron losses models are present in literature [67, 99, 100]. In those studies, iron losses are modelled as the thermal power dissipated on an *iron loss* resistance R_i placed in series, or in parallel, to the conventional PM synchronous motor equivalent circuits. It has been found that there is a substantial equivalence between series and parallel

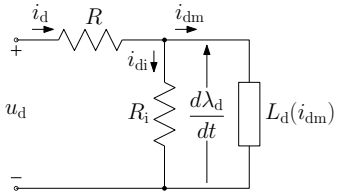

Figure 3.2: d-axis equivalent circuit, including iron losses, at standstill.

types [101]. Hereafter, the latter will be chosen for its better adherence to the physical meaning [101]. The comprehensive equivalent circuit for the d-axis at standstill is reported in Figure 3.2.

The iron losses equivalent resistance R_i is inserted in parallel to the flux-producing branch. Thus, the d-axis current is split into the iron loss current i_{di} and the magnetizing current i_{dm}. Around each working point $P(I_{dc})$, it is assumed that a small sinusoidal signal at fixed frequency Ω_s maintains circuit linearity, so that the differential inductance $L_d(P)$ may be considered as a constant. The total input impedance $\dot{Z}$ of the circuit in Figure 3.2, at the frequency Ω_s is given by

$$\dot{Z} = R_s + \frac{\Omega_s^2 R_i L_d^2(I_{dc})}{R_i^2 + \Omega^2 L_d^2(I_{dc})} + j\frac{\Omega_s^2 R_i^2 L_d(I_{dc})}{R_i^2 + \Omega^2 L_d^2(I_{dc})}. \tag{3.1}$$

Expression (3.1) includes the dependence of L_d from the frequency, whose influence has to be carefully evaluated.

AC small multi-sinusoidal voltage u_d and the relative composite current i_d will be used to compute the inductance L_d as function of the working point I_{dc}. In order to obtain the current component at the injected frequency, the Goertzel algorithm was used. Details of the algorithm implementation are reported in Appendix A. The voltage component can be measured, Sect.2.3, or estimated from references. The latter case requires a precise inverter non idealities compensation Sect. 2.2.

3.1.1.1 *Iron losses evaluation*

The first step regards both the iron losses and the most appropriate choice of the perturbation signals. Two series of measurements have been performed using a single frequency at a time, varying the frequency from 10 Hz up to 100 Hz, and by using both the voltage compensation algorithm and the voltage measurement system, respectively. With reference to Figure 3.2, the circuit is fed by a fixed frequency low-amplitude sinusoidal voltage, superimposed to a DC bias. It is reasonable to fix a frequency equal to the maximum electric angular speed of the motor, and a voltage bias that produces a DC current which is far enough from zero to avoid the effects of the IGBTs. The Goertzel algorithm, illustrated in Appendix A, is applied to both the (compensated) reference voltage signal and the measured

current. It returns the real and imaginary parts, which are used to compute the input impedance Z_d. Afterwards, the iron-losses equivalent resistance R_i is soon obtained by

$$R_i = \frac{(\Re(Z_d) - R_s)^2 + \Im(Z_d)^2}{\Re(Z_d) - R_s}, \tag{3.2}$$

Once R_i is calculated for a given angular frequency Ω_s, L_d can be immediately derived as:

$$L_d = \frac{R_i}{\Omega_s} \frac{\Re(Z_d) - R_s}{\Im(Z_s)}. \tag{3.3}$$

Equation (3.3) represents the real inductance L_d that depends on frequency, as the iron losses do. In details, the effect of the applied voltage was a 0.3 A, 100 Hz sinusoidal current, superimposed to a constant current of about 90% of rated motor current. The amplitude of the applied perturbation was limited by the need of maintaining the current within the rated value, while the DC component was as high as possible, to avoid voltage measurements around zero. Expression (3.2) returned $R_i = 287\,\Omega$, and the corresponding direct inductance, computed using (3.3), was $L_d = 20.32$ mH. On the other hand, the simple computation of the inductance[1], neglecting the iron losses effect, returns a value of $L_d = 19.82$ mH, with a percentage error of about 2.5%. This figure is expected to reduce further, with decreasing motor speed, and therefore it can be reasonably neglected. On the opposite, in case of motors with sensible iron losses, R_i has to be included, for an accurate inductance estimation.

3.1.1.2 *Design hints*

It is now worth to develop some considerations about the design of experiments, especially as regards the choice of the current amplitude. Factors like the power source and the measurements accuracy have to be taken into account, because they play a crucial role into the estimation process. On one hand, the linearity condition has to be guaranteed by a sufficiently small current perturbation, to avoid distortion, and then loss of local linearity, in case of possible *d*-axis magnetic saturation. On the other hand, the voltage produced by the inverter has several important aspects as well. Due to the standstill condition, there are no back electromotive forces, which means that in order to get the desired DC current the applied voltage has to overcome the stator resistance drops only. It follows that the applied voltage is of

1 From the definition of impedence, i.e. $\dot{Z} = R + j\Omega_s L_d(I_{dc})$, the inductance can be calculated as:

$$L_d(I_{dc}) = \frac{\Im(\dot{Z})}{\Omega_s}$$

the same order of magnitude of the inverter non-idealities compensation. This implies that whether the voltage reference signal is close to zero, even though the voltage compensation algorithm is used, the knowledge of the real voltage might be very tricky . Furthermore, the bus voltage is normally much higher than the desired voltage signal, and a very low modulation index increases the random noise due to finite mathematics of the digital modulator. High frequencies of the injected signal are then to be preferred, close to the nominal motor speed. Also a DC bias current far from zero is advisable, since at low current there is no evident saturation, and there is no need of multiple measurements. In this thesis work, half of the rated current was picked as the lowest value of the DC current range offset. Secondly, another simple test can be performed to single out the perturbation current amplitude which represents the best trade off between results richness and linearity condition. A single frequency at 100 Hz was injected at those two working conditions, and the second harmonic of the injected signal has been monitored by means of the Goertzel algorithm. It has been found a discriminant value of 0.3 A, from which the difference between the second harmonics of the signal with the voltage compensation algorithm and the one without the compensation increases sensibly. That value of 0.3 A was chosen to carry out the tests that will be presented in the next sections. It is worth to note that only negative i_ds are applied in both SPM and IPM motors, as they are the most common operating conditions. For instance, it was demonstrated in Sect. 1.3 that MTPA control implies negative i_d. Flux-weakening control is another case where negative i_d is applied to get a reduced BEMF and thus gaining voltage to increase the speed.

3.1.1.3 *Direct inductance estimation with voltage compensation*

A first batch of measurements was carried out using the voltage compensation algorithm described in Sect. 2.2.1.3. Different bias DC currents were imposed, from $I_N/2$ up to I_N, to get the complete map of a possible magnetic saturation. Different frequencies were used, from 10 Hz up to 100 Hz, to study the effects of the different testing signals. The results are reported in Figure 3.3, where the vertical straight lines represent the variance of each batch of measurements. It is worth to note that at low frequencies there is a large variance in the measurements, confirming that the very low applied voltages are really difficult to produce and to compensate. It is then advisable to use the highest frequency, i.e. 100 Hz.

3.1.1.4 *Direct inductance estimation with voltage measurement*

The same tests of 3.1.1.3 were repeated, with direct voltage measurement. The results are reported in Figure 3.4, which shows the inductance as function of the DC current bias, while the frequency acts as

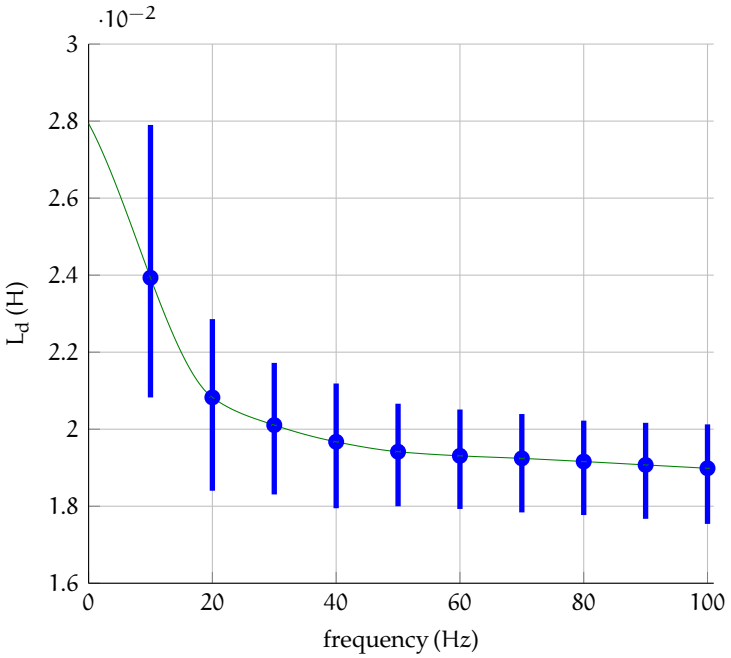

Figure 3.3: Measured L_d using the voltage compensation algorithm, as function of injected frequency. Vertical straight lines represent the variance at different DC current levels.

a parameter. The y-axis dispersion is small, as expected by the theory and the conclusions of Sect. 3.1.1.1, with the exception of the data at 10 Hz and 20 Hz, which are clearly unreliable. It is worth to note that the L_d values are slightly higher than the values of L_d obtained in Sect. 3.1.1.3. This is possibly due to some imprecision in the compensation look-up table, most felt at low voltage amplitude, with a real applied voltage slightly bigger than the reference one.

3.1.1.5 *The multi-sinusoidal signal injection*

The method outlined in Sect. 3.1.1.4 is valid, but necessarily slow, as it requires successive applications of the Goertzel algorithm. The Goertzel algorithm takes up to 2 s for each value to get the phasor component, depending on the desired discrete Fourier transform (DFT) selectivity (Appendix A). It was experienced, though, that the algorithm takes approximatively three complete tone computation to get a stable result. The procedure takes, in turn, about 5-6s for each combination of frequency and DC current. As a matter of fact, with no compromises on accuracy, such method takes up to 30 min. In order to perform the self-commissioning procedure in a faster way, the following multi-sinusoidal signal is proposed:

$$u_d = U^*_{d,0} + \sum_{n=1}^{M} U^*_{d,n} \cos(n\omega_0 t + \phi_n), \tag{3.4}$$

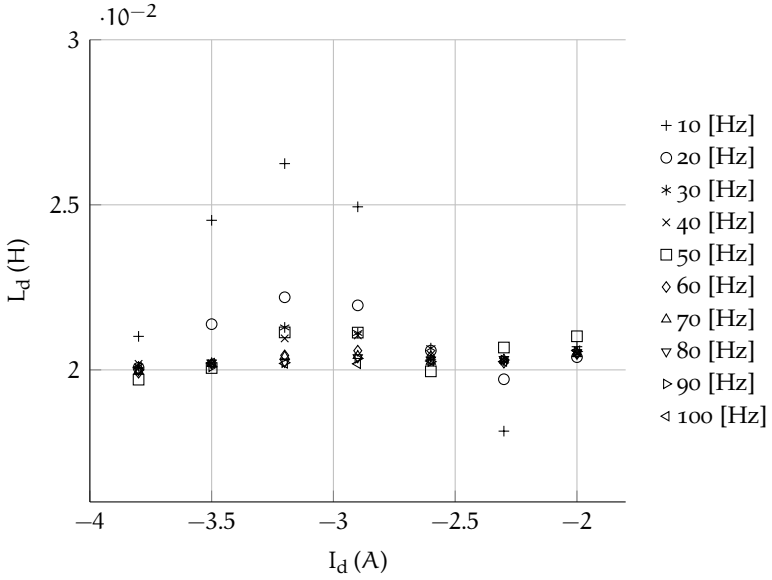

Figure 3.4: Direct inductance measured using the voltage measurement system.

where $U^*_{d,0}$, M, $U^*_{d,n}$, ω_0 and ϕ_n are the parameters of the test signal. These parameters offer many degrees of freedom on the design of the best tailored test signal, but they might be of tricky choice, because at standstill the applied voltage can force the current over the rated limit.

The parameter $U^*_{d,0}$ is used to modify the average *d*-axis current. Parameters like M and $U^*_{d,n}$ have to be selected to keep the peak current value under the rated value. That is possible when both M and $U^*_{d,n}$ are small quantities. In particular, M is linked to ω_0, since M delimits the test signal spectrum. The based speed of the motor under test was 3000 rpm, which corresponds to an electromechanical base frequency of 100 Hz that will be the maximum frequency of the multi-sinusoidal signal. To preserve the linearity, as discussed in Sect. 3.1.1.2, by maintaining a low amplitude of the perturbation signal, an $M = 4$ was selected and the corresponding frequencies have been fixed to 10, 30, 40 and 50 Hz. To get measurements at higher frequency, in particular at 100 Hz, it is sufficient to double the previous set of frequencies, which is very easy to get automatically into the software. For the sake of completeness, the multi-sinusoidal signal were designed and tested as well. All the considerations have been reported in the latter sections as useful hints in cases where the iron losses cannot be neglected.

Based on the work proposed in [103], the phases ϕ_n have been selected by the Schroeder method [92], which guarantees a low peak-to-peak value compared to a constant phase displacement of voltage multi-sinusoidal signal. An example of such a signal is reported in Figure 3.5, where the measured voltage confirms the good quality of

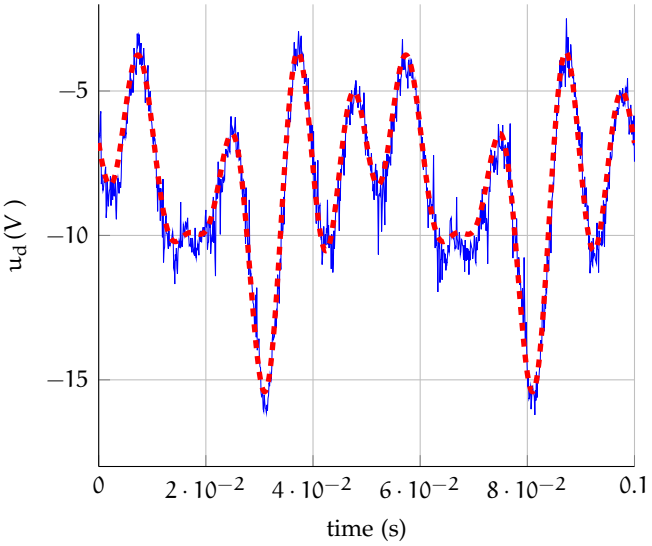

Figure 3.5: Measured voltage signal (with activated inverter non-ideality compensation) and the voltage reference (dashed line).

the voltage compensation algorithm. In the motor case of this thesis work, the iron losses does not affect the L_d estimation and the multi-sinusoidal test might be avoided.

The results obtained with the multi-sinusoidal perturbation are reported in Figure 3.6. It can be noted that the variances remain quite similar to those reported in Figure 3.3, while the execution time drops off to 10 min, with possible further abatement if less accurate measurements are tolerated. Lastly, the results plotted in Figure 3.6 and Figure 3.4 show that there is no evident magnetic saturation in the motor under test.

3.1.2 *Quadrature flux estimation*

The quadrature axis L_q estimation experiences rather important implementation issues compared to L_d in Sect. 3.1.1.4. It is preferable to keep the rotor still during a self-commissioning procedure or rather rotating at a fixed and controlled speed. However, the production of i_q implies an uncontrolled rotation of the rotor. This is unacceptable, and other solutions must be found.

A viable solution is to lock the rotor with a mechanical brake and carry out the procedure reported in Sect. 3.1.1 for the q-axis inductance as well. The current domain for the procedure should span from zero to the desired maximum current, typically the nominal one. The result is a complete map of the differential inductance of the motor. Furthemore, cross coupling can be evaluated, provided the i_d current is changed during the procedure as well.

In this thesis, a new approach to the q-axis flux λ_q estimation has been developed, rather than the differential L_q. The λ_q characteris-

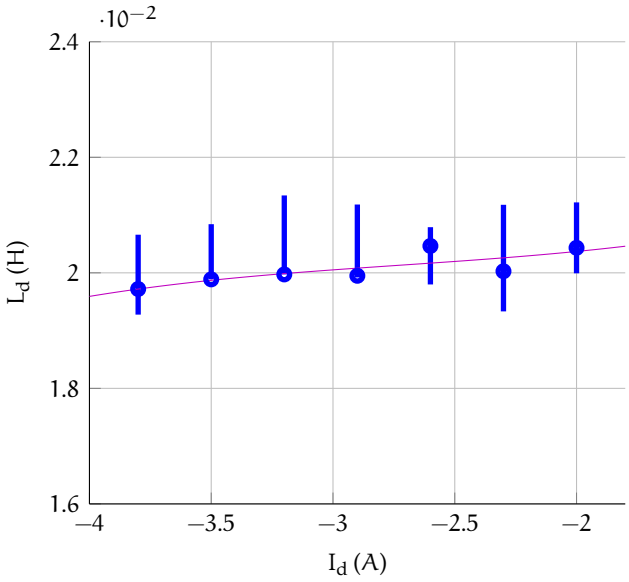

Figure 3.6: Direct inductance measured using the voltage measurement system. Variance is related to different injection frequencies.

tic is estimated considering the information encapsulated into the MTPA information. The MTPA mathematical description is reported in Sect. 1.3.1. It is worth to report that scientific literature offers a large variety of algorithms for the automatic research of the MTPA working point. Some model-free, mostly perturbation-and-observe methods based on extremum seeking control working principle, MTPA techniques are [3, 25, 57, 97]. For the sake of λ_q estimation, it is important to note that the MTPA condition (1.50) is applied to (1.43) assuming constant magnetic parameters. However, the design trend of IPM motors is toward non-linear magnetic structures [39], [19], so that the dependency of the parameters calls for a more precise mathematical description. The straightforward substitution of (1.44) in (1.50) yields a complex nonlinear expression between currents and flux linkages:

$$\frac{\partial \tau}{\partial i_d} = \frac{\partial \lambda_d(i_d, i_q)}{\partial i_d} i_q - \frac{\partial \lambda_q(i_d, i_q)}{\partial i_d} i_d - \lambda_q(i_d, i_q) \tag{3.5}$$

Expression (3.5) still contains the dependency of the flux linkages on the currents, and it is not directly exploitable for the λ_q estimation. Therefore, taking (3.5) as a starting point, a viable alternative was examined and reported in the next paragraphs.

To easy the dissertation, the FEA results reported in Sect. 1.2 are proposed again in this Section with few modifications. Since the estimation technique is based on the MTPA information, only motor operations will be considered. The region corresponds to only negative i_d and positive i_q. The experimental results of the MTPA curve obtained for the motor under test are reported in Appendix B.

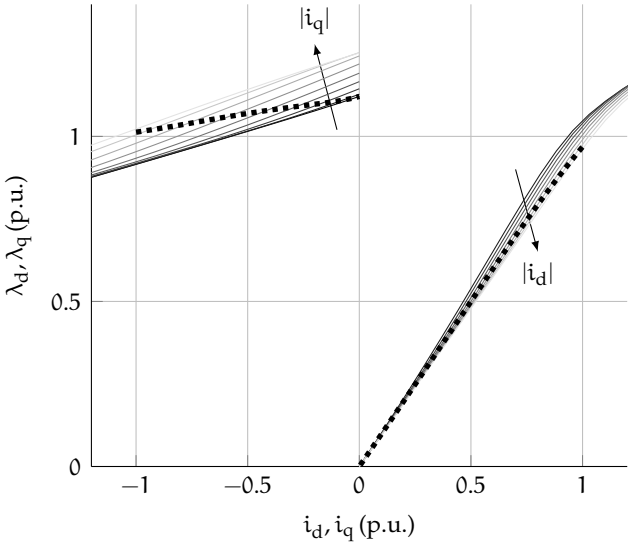

Figure 3.7: Cross-coupling effect in the d- and q-axis flux linkages (continuous-thin lines). The square-dotted lines represent the flux-linkages in the MTPA locus.

3.1.2.1 *Analysis of the cross-coupling effects*

Figure 1.8 shows that, for any given i_d, the flux linkage λ_d grows with i_q. Actually, it has been found that the i_q-related flux lines desaturate the iron ribs close to the d-axis path, lowering its reluctance. This is particularly true when the d-path is not already completely saturated, i.e. for i_d close to zero. In that case, the d-axis flux is only due to the PM (Figure 1.7), and the presence of a (even small) cross-coupling effect leads to an increase of the effective PM flux linkage Λ_{mg} [60].

An opposite effect is induced by highly negative values of i_d, which cause the early saturation of some shared portions of the q-axis flux magnetic path, as depicted in Figure 3.7. In the same figure, the apparently odd reduction of the cross-coupling effect at i_q close or above the nominal value can be explained by the deep saturation of the iron path, which is therefore very little influenced by any further contribution of i_d.

It is worth to note that around the MTPA curve, the combination of high i_q and low i_d currents is not expected. The bold dotted lines in Figure 3.7 are relative to the flux-linkages produced in the MTPA condition, that in the next sections leads to draw some meaningful conclusions.

3.1.2.2 *Polynomial fluxes approximation*

The idea proposed in this thesis is to extend the model definition (1.20), by considering the polynomial approximations of both d- and q-axis flux linkages. In principle, this makes possible the consideration of both the saturation and the cross-coupling effects. For the sake

of technical soundness, a suitable trade-off between the accuracy of the approximation and the complexity of the algorithm is mandatory. With a look at the curves shown in Figure 3.7 and at those of motors of the same type, λ_d can be described as a linear function of i_d. Furthermore, noting that the family of curves is quite regular for even increments of i_q, the cross-coupling effect over λ_d is represented by another linear term, so that:

$$\lambda_d(i_d, i_q) = L_d i_d + \Lambda_{mg} + K_c i_q \tag{3.6}$$

As mentioned, in the MTPA condition small i_d currents also means small i_q currents, as shown in Figure 3.7. Therefore, the PM flux linkage Λ_{mg} can be obtained by an open-terminal voltage measurement, or simply by taking the nameplate value provided by the motor manufacturer. It is also worth to note that the $\lambda_d - i_d$ curve in the MTPA condition (around which the unknown parameters of (3.6) are going to be estimated) intersects the whole λ_d family of curves. As a result, provided that the no-load inductance L_d is otherwise estimated for instance with the method in Sect. 3.1.1, the MTPA curve embeds enough information to return the K_c value with fair approximation.

The q-axis flux linkage family of curves is normally approximated by a third order polynomial of i_q, with odd power terms only, as in [11], [89]. It is worth to note that even though the cited references refer to the saturation effect in the stator flux linkage of induction motor, the same method applies to IPM motor too, trusting on the similarity of stator structures. Thus, an approximation of λ_q is:

$$\lambda_q = b_1 i_q + b_3 i_q^3 \tag{3.7}$$

While it is reasonable to consider almost linear flux variations along the d-axis, due to the presence of permanent magnets as well, it is not on the q-axis, Figure 3.7. However, by considering a non-linear approximation as (3.7), the MTPA curve embeds enough information to account the cross-coupling effects on λ_q too. Such effects are not directly recognizable with a parameter as it does K_c in (3.6), but are encapsulated into the non linear multiplier b_3.

The new flux linkages equations, (3.6) and (3.7), can be included now into the torque equation (1.43):

$$\begin{aligned} \tau &= \frac{3}{2} p \left[(\Lambda_{mg} + L_d i_d + K_c i_q) i_q - (b_1 i_q + b_3 i_q^3) i_d \right] \\ &= \frac{3}{2} p \left[(\Lambda_{mg} i_q + K_d i_d i_q + K_c i_q^2 - b_3 i_q^3 i_d \right] \end{aligned} \tag{3.8}$$

where $K_d = L_d - b_1$. Therefore, the MTPA condition (1.50) is rewritten as:

$$(i_q^2 - i_d^2) K_d - 2 i_d i_q K_c + 3 (i_q^2 i_d^2 - i_q^4) b_3 = \Lambda_{mg} i_d \tag{3.9}$$

It is worth noticing that p and Λ_{mg} are usually known or measurable. In particular, Λ_{mg} can be estimable with on-line techniques [61].

3.1.2.3 *Polynomial parameters estimation*

The leading principle of this technique is to bring the IPM motor drive to work along several points of the MTPA curve, obtaining a batch of equations just like (3.9). Subsequently, the unknown coefficients K_d, K_c and b_3 are extrapolated by a standard least square (LS) algorithm, which fits for overdetermined systems, i.e. where there are more equations than unknowns:

$$A\mathbf{x} = \mathbf{c}, \tag{3.10}$$

where A is a $n \times 3$ matrix originated from (3.9):

$$A = \begin{bmatrix} i_{q1}^2 - i_{d1}^2 & -2i_{d1}i_{q1} & 3i_{q1}^2 i_{d1}^2 - i_{q1}^4 \\ i_{q2}^2 - i_{d2}^2 & -2i_{d2}i_{q2} & \cdots \\ \vdots & \vdots & \ddots \\ i_{qn}^2 - i_{dn}^2 & \cdots & \cdots \end{bmatrix} \tag{3.11}$$

and the vectors $\mathbf{x}$ and $\mathbf{c}$ are defined as:

$$\mathbf{x} = [K_d \; K_c \; b_3]^T, \quad \mathbf{c} = [\Lambda_{mg} i_{d1} \; \Lambda_{mg} i_{d2} \; \ldots \Lambda_{mg} i_{dn}]^T. \tag{3.12}$$

The vector $\mathbf{c}$ is an $n \times 1$ vector, and n is the number of MTPA points gathered as input to the parameter estimation algorithm. The choice of n is discussed later in Sect. 3.1.2.4.

3.1.2.4 *Design hints*

The parameter identification algorithm is clearly correlated to the MTPA information. In other words, the algorithm depends on the MTPA control, since (3.9) is true only if the drive is working in an MTPA condition. Thus, the MTPA control might be a source of uncertainty for each coefficients of the matrix A and $\mathbf{c}$. The number of MTPA points, i.e. n, is relevant to this matter. Although the value of n is an important aspect, a large number of points would not be sufficient to get a correct estimation of the desired parameters in certain cases. Clearly, what does matter is how they are distributed among the drive region of work and how much they are corrupted by disturbances. The latter might be introduced by the MTPA controller chattering around the exact MTPA point as well as from measurements.

The measured MTPA curve has been approximated by a third-order polynomial function, to keep a reasonably low degree of complexity. Anyway, the result was still not satisfactory, since the approximated MTPA curve in Figure 3.8a has multiple inflection points. A closer investigation has revealed that the problem lies in the first part of the MTPA curve, i.e. the part where the current is lower. In fact, at low current magnitude the MTPA controller might slightly fail, even though the error does not represent significant current magnitude variations.

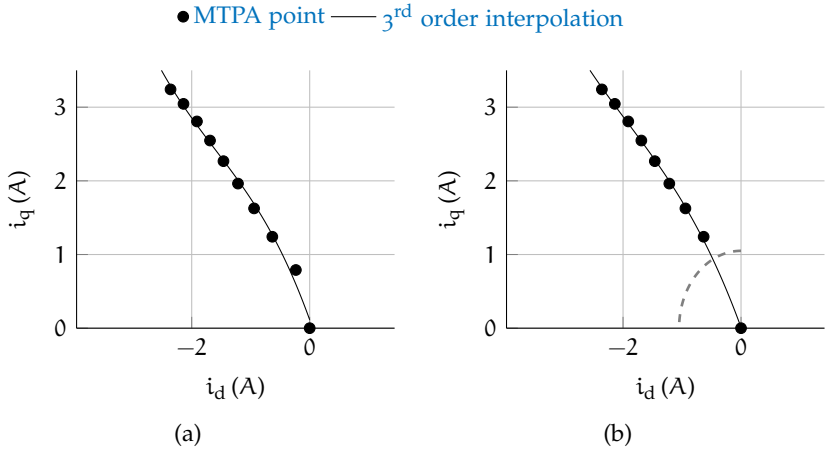

Figure 3.8: MTPA curves: (dots) measured points, (solid line) cubic interpolation. The dashed line corresponds to a magnitude equal to the 25% of I_n.

However, these small errors can influence the whole parameter identification algorithm, [32]. To this aim, it is reasonable to think that the most significant MTPA points are the ones related to the highest current magnitudes, since at low current the motor can still be considered quasi-ideal. At highest current magnitude, though, it is where phenomena such as iron saturation most likely happens. Bearing this in mind, several tests using the simulation analysis have helped to figure out that it is reasonable to skip the first part of the MTPA curve of about 25% the nominal current.

The number of measured MTPA points can be modest. Indeed, it is reasonable to measure points from 25% up to 100% of the nominal current at steps of 10% increment. It reduces the number of experiments with considerable saving of time. The measured MTPA points can then be interpolated by a cubic function as in Figure 3.8b. By means of the interpolating function, a complete set of MTPA points, from zero to the nominal current, can be gathered and used in (3.10) to solve the estimation problem. The use of the interpolating function unburdens the MTPA gathering, since it allows to collect few points, provided that they are well distributed. The latter points should be as precise as it gets. A practical solution is to collect several MTPA point at the same load level and used their average value.

Since L_d is known from Sect. 3.1.1, the b_1 parameter can be estimated from the $d = L_d - b_1$ definition. The estimation procedure returns the last unknown parameter, K_c.

3.1.2.5 *Experimental results*

The K_c, b_1 and b_3 parameters obtained as in Sect. 3.1.2.4 are reported in Table 3.1. They allow to obtain an estimation of the d- and q-axis magnetic fluxes using (3.6) and (3.7), respectively. Both the estimated

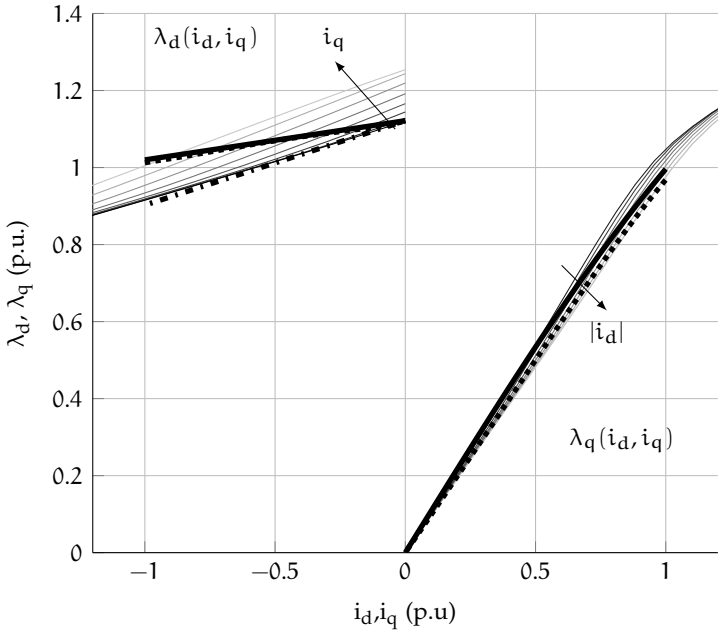

Figure 3.9: Estimated flux-linkages (continuous-thick lines) with the proposed technique. The square-dotted lines represent the flux-linkages in the MTPA locus; the dashed-dotted line represents the λ_d without the cross-coupling effect term K_c.

Table 3.1: Estimated parameters of the λ_q polynomial approximation.

Parameter	Value
K_c	0.0076
b_1	0.114
b_3	-0.0011

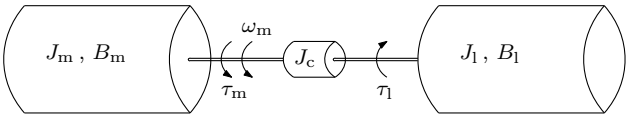

Figure 3.10: Mechanical scheme of a typical electric drive; frictions are reported to motor and load, while the coupling is considered as an inertia.

curves are reported in Figure 3.9, where the estimated flux linkages are compared with $\lambda_d(i_d, i_q)$ and $\lambda_q(i_d, i_q)$ curves obtained using FEA. Furthermore, as in Figure 3.7, the flux linkages in the MTPA locus are reported as well to get a close comparison. The results are accurate, with a maximum error of 2% respect to the MTPA flux linkages curve of Figure 3.7.

The estimated q-axis magnetic flux $\hat{\lambda}_q$ does not track over a single $\lambda_q(i_d, i_q)$ curve. It means that $\hat{\lambda}_q$ does not represent a single curve of $\lambda_q(I_d, i_q)$ for a specific I_d, but it takes into account the i_d cross-coupling term on λ_q during the MTPA operations. As i_q increases, the $\hat{\lambda}_q$ curve crosses the $\lambda_q(i_d, i_q)$ curves. The latter observation leads to the next intuition, that is the estimated q-axis flux linkage using (3.7) is, on average, reasonably close to the real one even out of the MTPA point of work. The drive works out of the MTPA condition during fast current transients, where automatic MTPA algorithm may not be able to track fast enough the actual maximum efficiency curve. With an identical approach, $\hat{\lambda}_d$ can be reasonably considered close to the real one even out of the MTPA point of work.

3.2 MECHANICAL PARAMETERS

A generic and approximated, though still quite realistic, mechanical model of the motor is:

$$\tau = \tau_L + \alpha_B \operatorname{sgn}(\omega_m) + B\omega_m + J\frac{d\omega_m}{dt} \tag{3.13}$$

The parameters α_B, B and J are to be estimated and they represent the total parameters of a typical mechanical system as in Figure 3.10. Therefore, such three parameters are defined as:

$$\alpha_B = \alpha_{B,m} + \alpha_{B,l} \qquad B = B_m + B_l \qquad J = J_m + J_l + J_c \tag{3.14}$$

where all the parameters are defined in Figure 3.10. It is worth noticing that J_c summarizes the couplings inertia, whether they are multiple couplings or just one. This means that the schematic of Figure 3.10 does not include the non idealities[2] of mechanical elements such as gears. The identification of those non idealities is out of the scope of this work.

Coupling inertia approximation

2 For instance, efficiency of mechanical gears and backlash are not considered in the scheme of Figure 3.10

3.2.1 *Least Square approach*

A classic approach for identifying friction and inertia parameters is presented in this section. The principle is sketched out in Figure 3.11. The procedure consists on collecting a batch of measurements with the motor tracking the speed profile as reported in Figure 3.11. The rotor acceleration is thus constant, so the torque necessary to move the inertia is constant. However, speed changes and so does the viscous friction load. Let that latter changes characteristic be linear. Therefore, the motor torque compensates the constant load term of the inertia, the constant friction term and the viscous friction coefficient: the motor torque looks like the one in Figure 3.11.

The minimum number of samples for parameter estimation is the number of parameters itself. However, experimental measurements are affected by measurement noise and errors, so a low number of samples would undermine the correct parameter estimation. For the sake of acceptable estimation, the measurement campaign should gather several ramps as in Figure 3.11. It is important to carry out the same experiments at both positive and negative speed, since the value of α_B depends on the speed sign too. The batch of samples, i.e. speed, acceleration and measured torque, are then used to fill the following expression:

$$\underbrace{\begin{bmatrix} 1 & \operatorname{sgn}(\omega_1) & \omega_1 & \dot{\omega}_1 \\ 1 & \operatorname{sgn}(\omega_2) & \omega_2 & \dot{\omega}_2 \\ \vdots & \vdots & \vdots & \vdots \\ 1 & \operatorname{sgn}(\omega_n) & \omega_n & \dot{\omega}_n \end{bmatrix}}_{\Phi} \underbrace{\begin{bmatrix} \tau_L \\ \alpha_B \\ B \\ J \end{bmatrix}}_{p} = \underbrace{\begin{bmatrix} \tau_1 \\ \tau_2 \\ \vdots \\ \tau_n \end{bmatrix}}_{Y} \tag{3.15}$$

which is already written in canonical form for LS estimation [42], that is:

$$\Phi p = Y \tag{3.16}$$

where p is the vector of the unknown, Φ is the regression matrix coefficients and Y are the measured variables. Then, by applying the LS algorithm to problem (3.15) the parameters p are estimated.

An experimental batch of results is reported in Figure 3.12, taken at no-load. Thus, the mechanical parameters refer to the motor ones. However, results from experiments with the setup of Figure 3.10 would look very similar. The mechanical data used for all motors in this work were obtained with the aforementioned procedure. The friction and inertia coefficients obtained for the motor under test are reported in Table 3.2

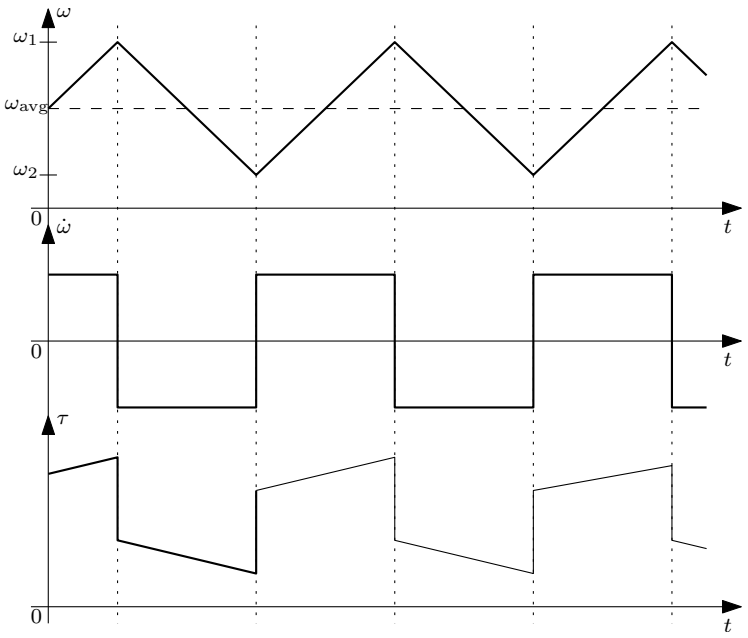

Figure 3.11: Ideal curves for mechanical parameter estimation: speed, acceleration and torque respectively.

Table 3.2: Mechanical parameters obtained with the LS procedure.

Parameter	Value
J	$0.000\,94\,\mathrm{kg\,m^2}$
B	$155\,\mu\mathrm{N\,m\,s\,rad^{-1}}$
α_B	$0.065\,\mathrm{N\,m}$

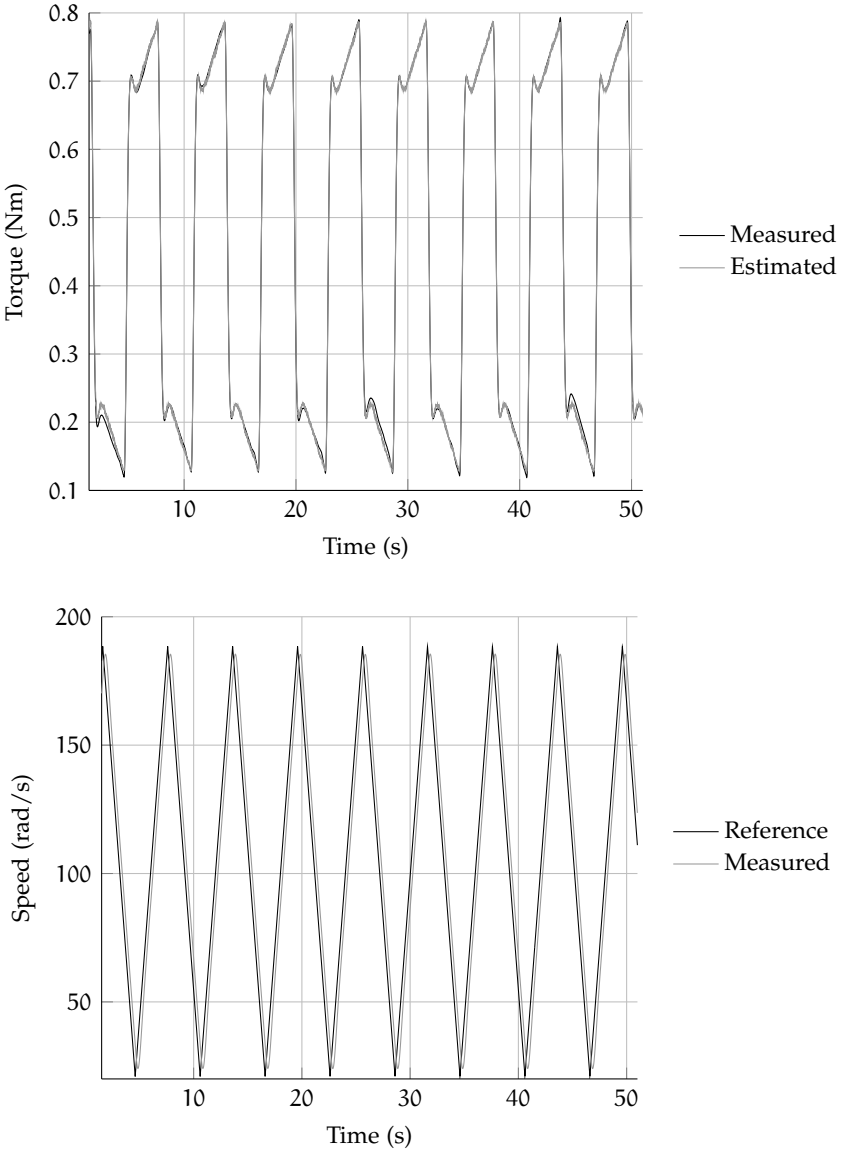

Figure 3.12: Experimental batch of results of a PMSM for mechanical parameter estimation.

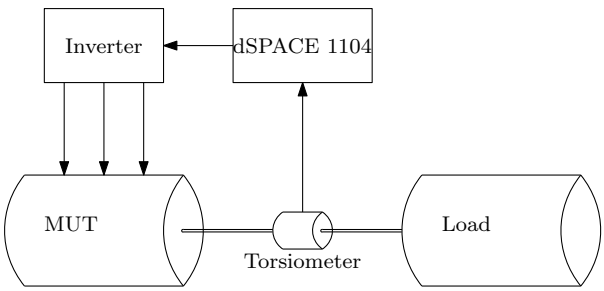

Figure 3.13: Experimental setup

Table 3.3: IPM–PMSM nominal parameters.

Parameter	Symbol	Value
Rated current	I_N	4.2 A
Rated $\lvert i_d \rvert$ (MTPA condition)		2.38 A
Rated i_q (MTPA condition)		3.46 A
Pole pairs	p	2
PM flux linkage	Λ_{mg}	0.245 Wb
Rated torque	τ_N	4.5 N m
Rated speed	Ω_m	3000 rpm

3.2.2 *Electromechanical torque estimation*

The *dq*-axes magnetic flux estimation proposed in Sect. 3.1.2.2 can be used to obtain a fast and easy to use electromechanical torque estimator. The torque estimation is based on (3.8), after that all the parameters have been properly identified. The torque estimation algorithm had been tested on a real test bench. The experimental setup is sketched in Figure 3.13. The main motor parameters are reported in Table 3.3, whereas the load motor consists on an IM motor controlled by a second drive system. The torsiometer is a Magtrol TM300 series.

Bearing in mind that the setup of Figure 3.13 allows to measure the mechanical torque only, the here proposed method gets the electromechanical torque estimation. The mechanical torque at steady state for a positive speed is equal to:

$$T_m = T - B\Omega_m - \alpha_B \tag{3.17}$$

Mechanical parameters of (3.17) are obtained as in Sect. 3.2. The aim is to compare the electromagnetic torque with the one measured by the torsiometer, the setup was slightly modified. In fact, the load motor was locked, i.e. no rotation of the shaft was possible. The electromagnetic torque produced by the IPM motor drive can be then considered equal to the one measured by the torsiometer. In other words, in (3.17) the viscous friction terms, that is function of the speed, becomes zero as well as the dry friction load[3] α_B. The results of this comparison is reported in Figure 3.14, with respect to the nominal torque. It is important to highlight that the torque estimator seems to fail when the current is almost i_d only when i_q is close to zero, because the error gets bigger. The reasons are mainly two:

3 The coefficient α_B is multiplied by the speed sign as in (3.13). A critical point is when the speed changes its rotation direction. A practical solution is to define a sign function with the same characteristics of the inverter non idealities ramp compensation in Sect. 2.2.1.2. Below a certain speed threshold, the sign module decreases from one in a proportional way with the speed.

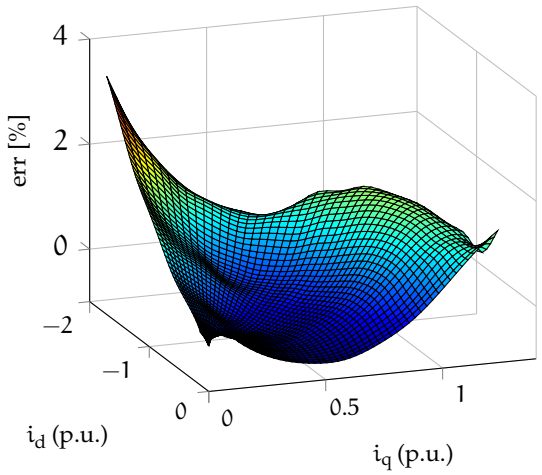

Figure 3.14: Torque estimation error of the experimental tests.

Table 3.4: Torque estimation error in several significant MTPA points.

|i| [A]	err [%]	|i| [A]	err [%]
0.5	-0.15	2.5	0.01
1	-0.41	3	0.46
1.5	-0.415	3.5	1.11
2	-0.24	4	1.533

- when i_q is very small the torque is small, too, no matter i_d;
- the measured torque accuracy is affected by the torsiometer resolution, which is 0.02 N m in this case.

On the other hand, this is a very unlikely situation, so this aspect does not compromise the effectiveness of the proposed algorithm. A very likely situation, though, can be found when the drive works in MTPA condition. For this purpose, some torque estimation errors related to significant values of current are reported in Table 3.4. As a fact, the error stays below the reasonable value of 2%.

Other measurements were executed to test the effectiveness during motor operation. The IPM motor was speed controlled, while the load simulator motor was torque controlled. With the motor running at constant speed, five steps of load torque were applied by the load motor. The result of this test is reported in Figure 3.15, with the error expressed in percentage of the nominal torque. The torque estimator has almost no dynamics, due to the fact that the torque estimator is based only on the current measurements. Furthermore, as stated in Sect. 3.1.2.4, the estimated torque is very close to the real one even though the drive works off the MTPA point. This happens during the transients, where the polynomial approximations of the flux linkages still guarantee excellent results in terms of torque estimations.

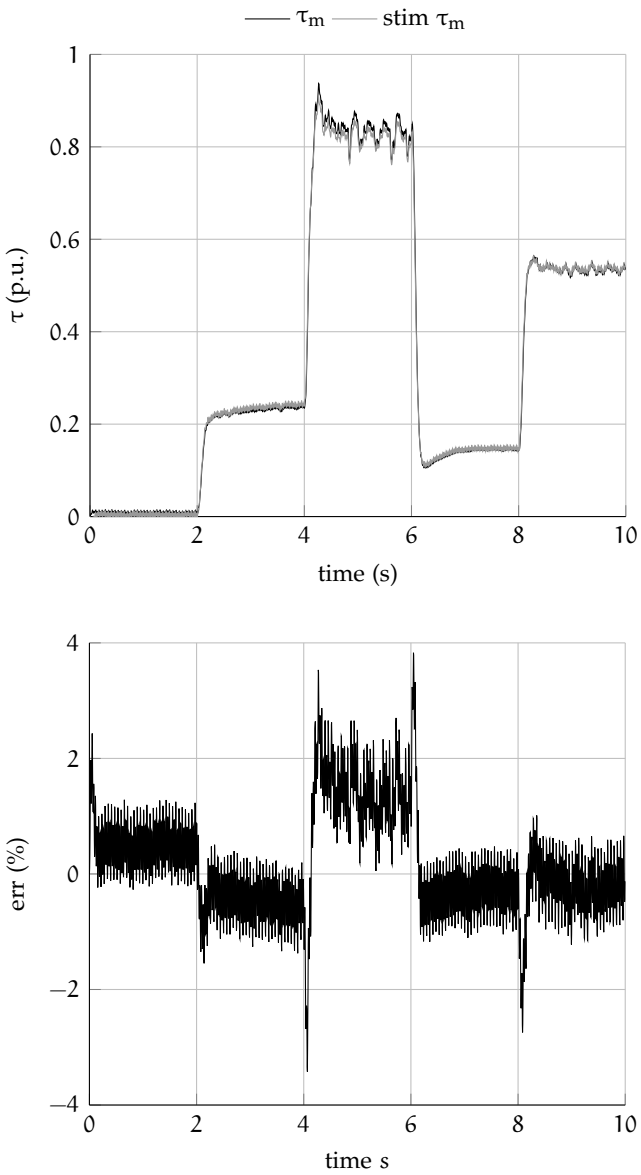

Figure 3.15: Comparison between measured and estimated torque of different load steps at 1000 rpm

Part II

ADVANCED CONTROL OF PMSM

4

SENSORLESS CONTROL

Synchronous PM motors control is unavoidably bounded to the rotor position information. Mechanical position sensors are thus embedded on the drives, resulting in an increase of costs and reduction of reliability. Last decades trend was the use of some estimation techniques in place of any mechanical sensor, resulting in what are called *sensorless drives*. Sensorless drives are still a matter of interest in the scientific community, where scientists aim at making them cheaper, more efficient and reliable..

Position estimation techniques vary considerably on the PMSM characteristics and region of work, in particular the electromechanical speed. Mainly two distinct solutions are established so far:

- zero/low speed based on high frequency signal injection;
- medium/high speed based on fundamental frequency signals.

The former solution takes advantage of the motor anisotropy. The position is usually obtained by the injection of high frequency (HF) voltage signals and by post-processing the related HF currents. SPM motors, featuring little or no saliency, are almost banned from HF signal injection based techniques, although an example could be found in the literature [51]. As soon as the motor speed is high enough to get a sufficient signal-to noise ratio in the voltage signals, observers based on the fundamental frequency signals are employed to estimate the rotor position. Differently from the HF signal injection techniques, fundamental signals observers apply to all sort of motors. For applications where low-speed operations are only transient and repeated few times, a fundamental frequency observer combined with a simple startup procedure represents an effective and low cost solution. This thesis presents, as a case study, a refinement of an existing startup technique [106] (Sect. 4.2) and a thorough investigation of a dq -phase-locked loop (PLL) for extracting the electromechanical position from a BEMF observer(Sect. 4.3). Furthermore, startup techniques require the knowledge of the initial position of the rotor to avoid undesired rotations in the opposite direction. A re-visitation of a well known technique, enhanced by the implementation of a voltage measurement system, is proposed in Sect. 4.1.

The focus is on mechatronics applications that require low cost solutions, for instance washing machines, dryers, pumps and so forth. Due to the large distribution of such commercial devices, their energy efficiency counts considerably on the total energy consumption reduc-

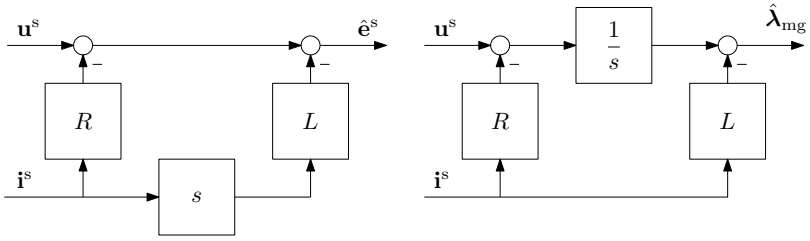

Figure 4.1: Observers for medium/high speed sensorless algorithms.

tion. The precision in the position estimation results in the reduction of current consumption, in any case.

Reviews about sensorless control algorithms have been published lately [2, 20, 28, 90]. Techniques based on the fundamental frequency signals work only at medium/high speed, where voltages have a favourably high signal-to-noise ratio. The lower the speed, the higher the effects of inverter non idealities. Furthermore, fundamental frequency techniques rely on a mathematical motor models where the position is explicated by the presence of the speed. The position estimation is thus impossible at zero speed. Due to the strong link between fundamental frequency techniques and mathematical motor models, the following considerations can be made to assure better performances:

- enhancing the estimation accuracy of motor parameters;
- adopting either inverter non idealities compensation techniques or voltage measurement;
- improving the electrical signal measurements.

Mathematical models for fundamental frequency sensorless drives can be divided into two groups:

- BEMF based;
- PM flux vector based.

A fine distinction is among the observer used to estimate the state variables. Techniques such as model reference adaptive system (MRAS) or PLL rely on an observer to estimate an electric quantity which is supposed to be true. Typical observer schemes are reported in Figure 4.1, where both observers are expressed in the stator reference frame, i.e. $\alpha\beta$. The sensorless technique classification for medium/high speed application is reported in Figure 4.2. In this work, a BEMF observer in the dq reference frame is considered and implemented on several PMSM motors, both isotropic and anisotropic.

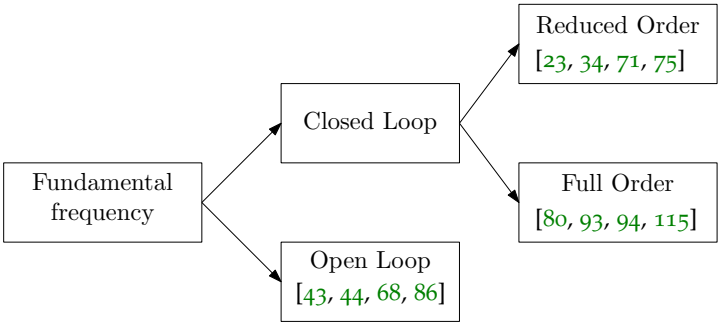

Figure 4.2: Medium/high speed sensorless classification.

4.1 INITIAL POSITION ESTIMATION

In principle, the difficulties due to the lack of knowledge of the initial position can be potentially circumvented by aligning the rotor magnetic axis along the direction (typically, a phase axis) of the magnetic field generated by a fixed stator current vector applied at startup. In practice, however, the presence of unavoidable load and friction torques limits the accuracy of the alignment process. Moreover, some applications – as submerged electric water pumps – require a predetermined sense of rotation, which is not guaranteed by the aforementioned abrupt alignment method. The study and development of effective methods for estimating (rather than imposing) the initial rotor position is then fully legitimised.

With few exceptions, almost all the methods proposed so far in literature exploit the stator inductance variations induced by either the magnetic or geometric anisotropies (saliencies) of the machine to infer the actual position of the rotor. In machines with surface–mounted magnets, a variation in the stator inductance can be noticed whenever the flux produced by the permanent magnets is large enough to saturate the iron in the stator teeth. On the contrary, in machines with buried magnets, the stator inductance variations are mainly due to the different permeability of the magnetic paths along the direct and quadrature axes. Therefore, for PMSMs the smaller inductance is expected along the direction of the d-axis [19]; a reversed situation holds instead for flux–concentrating interior PM motors (PM axis with tangential orientation), where the smaller inductance is that of the quadrature–axis [20]. Moreover, for inset PM motors, the saliency is further increased by the possible saturation of the iron bridges in the rotor [16]. The flux-concentrating IPM and inset motors are not considered in this thesis work.

The detection of inductance variations can be done either by performing a direct estimation of the stator inductance or, more conveniently, by tracking variations of some electrical quantities affected by it [2]. In any case, the machine has to be properly excited to reveal its saliency features: typically, this is performed by injecting either pul-

sating [27, 74, 91, 98] or persistent high–frequency voltage or current signals [18, 47, 58, 64].

Methods for the estimation of the initial rotor position of PM motors abound in literature. Among the most cited and used, especially for its easiness of implementation and reasonable accuracy, is the one initially proposed in [74] for IPM motors, and subsequently adapted in [91] to SPM motors. Basically, the method consists in measuring the magnitude peak of the stator current vector produced by short–pulsed stator voltage vectors applied along different directions in the reference frame fixed to the stator. Since the current growth rate is inversely related to the stator inductance, a larger current peak is expected for a smaller stator inductance. Since the maxima and minima of the current peaks profile over an electromechanical period occur along the rotor magnetic axis and its orthogonal axis, the procedure for estimating the initial rotor position simply reduces to a search for the extremal points of the current peak envelope. The ambiguity regarding the rotor orientation, namely the position of the PM north and south poles, is often tackled by evaluating the effects of the application of two oppositely oriented voltage pulses along the identified direction of the rotor magnetic axis [54].

To be effective, the estimation procedure requires the application of voltage pulses with the same amplitude, regardless of their direction in the fixed frame. This is a difficult condition to guarantee, due to the well-known voltage inverter non-idealities and DC bus fluctuations [63]. Even though dead–times and other detrimental effects can be partially compensated [24, 76, 87], far better operating conditions are obtained by a direct measurement of motor terminal voltages.

With such premises, the work presented in this thesis is aimed at exploring what are the benefits brought by the availability of a direct measurement of the inverter terminal voltages to the detection of the initial position of sensorless PM motors. The voltage measurement has been presented in Sect. 2.3. The proposed technique is a readjustment of the classical method initially proposed in [74], in which the voltage measurements are used as a feedback to regulate the amplitude of the applied voltage pulses. Several experimental results, obtained on two different motors with different saliency properties, are reported in the following.

4.1.1 *Voltage pulses detection method*

In a vector–controlled PMSM, providing that at standstill the electrical behaviour along a specific direction in the stator reference frame can be approximated by a simple RL circuit, the inductance variations due to the machine saliency can be revealed by applying short voltage pulse along different directions, and measuring the corresponding current magnitude peak obtained at the end of the pulse [74]. Let us

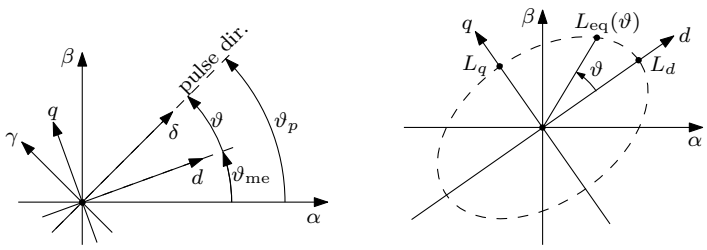

Figure 4.3: (a) Relative orientations of the δ-γ (pulse) and dq (rotor) reference frames in the α-β (stator) reference frame. (b) Equivalent inductance ellipsoid.

consider the generic electrical equations of a PMSM in the dq reference frame (1.14). Defining a new δ–γ reference frame, with the δ axis fixed with the direction of the applied voltage pulse (Fig. 4.3a), the PMSM voltage model becomes

$$u_{\delta\gamma} = \mathbf{R}\, i_{\delta\gamma} + L_{\delta\gamma}\frac{di_{\delta\gamma}}{dt} + e_{\delta\gamma} \tag{4.1}$$

where

$$L_{\delta\gamma} = \begin{bmatrix} L_d \cos^2\vartheta + L_q \sin^2\vartheta & \dfrac{L_q - L_d}{2}\sin 2\vartheta \\ \dfrac{L_q - L_d}{2}\sin 2\vartheta & L_d \sin^2\vartheta + L_q \cos^2\vartheta \end{bmatrix}$$

with ϑ denoting the electrical angle between the dand δ axes. If a short voltage pulse is applied under zero initial current conditions, then the voltage drop due to the resistance term can be neglected, and (4.1) reduces to

$$u_{\delta\gamma} \approx L_{\delta\gamma}\frac{di_{\delta\gamma}}{dt} \quad \Rightarrow \quad i_{\delta\gamma}(t) \approx \int_0^t L_{\delta\gamma}^{-1}\, u_{\delta\gamma}(\tau)\, d\tau \tag{4.2}$$

providing that the machine operates at standstill, i.e. $e_{\delta\gamma} = 0$. Hence, for a short voltage pulse of amplitude U_p and duration T_p applied along the δ axis, it is immediate to verify that the current magnitude at the end of the pulse is equal to

$$\|i_{\delta\gamma}(T_p)\| \approx T_p\, U_p \sqrt{\frac{\cos^2\vartheta}{L_d^2} + \frac{\sin^2\vartheta}{L_q^2}} \tag{4.3}$$

which corresponds to the (approximated) response of a RL circuit with equivalent inductance

$$L_{eq}(\vartheta) = \left(\frac{\cos^2\vartheta}{L_d^2} + \frac{\sin^2\vartheta}{L_q^2}\right)^{-1/2} \tag{4.4}$$

Note that $L_{eq}(\vartheta)$ describes an ellipse in the stator reference frame, whose main axes are aligned with those of the dq (rotor) frame (Figure 4.3b). This implies that the current peak amplitude at the end

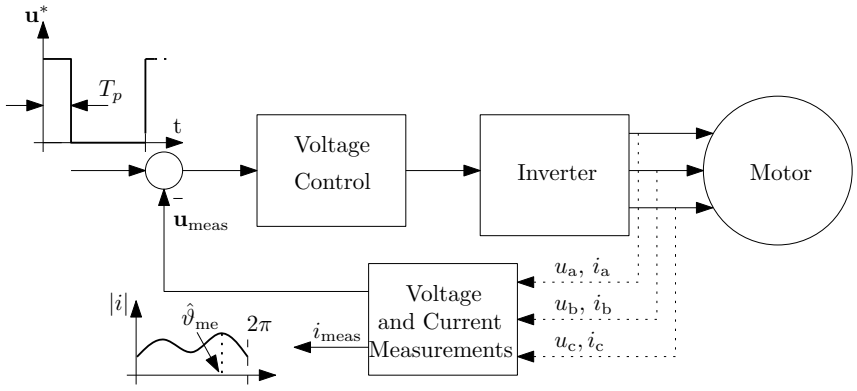

Figure 4.4: Scheme of the initial position estimation algortihm.

of the pulse is periodic with argument 2ϑ, and the local maxima and minima are reached along the direction of the rotor frame axes. Therefore, in a PMSM where $L_d < L_q$, the rotor initial position can be estimated by first seeking for the position of the maxima (or minima, if $L_q < L_d$) over an entire electrical angle ϑ period, which provides the direction of the rotor magnetisation axis (d–axis). Then, the axis orientation can be determined by noticing that for sufficiently large voltage pulses applied along the estimated d–axis direction, the two local maxima may differ because of inductance variations caused by the saturation in the magnetic circuit. The saturation can be forced either with a pulse oriented as the rotor d–axis, or its opposed, depending on whether it occurs in the stator teeth or in the rotor iron bridges. In fact, in the stator teeth, the magnetic field due to the permanent magnet is reinforced by applying a pulse oriented as the rotor d–axis; vice versa, the fraction of the permanent magnet field that closes through the iron bridges is reinforced when the pulse is applied in the opposite direction. Therefore, by knowing what is the prevailing saturation mechanism in the machine, it is possible to infer the orientation of the rotor magnetisation axis from the orientation of the voltage pulse that produces a saturation. The scheme of the initial position estimation procedure is reported in Figure 4.4.

To correctly reveal the inductance variations (4.4), it is important to apply voltage pulses with the same amplitude, regardless of their direction in the stator reference frame. In fact, a dependence of U_p on ϑ in (4.3) could overshadow those induced by the equivalent inductance (4.4), thus making impossible the identification of the rotor position. The generation of regular voltage pulses is accomplished by implementing a closed–loop control of the stator voltage vector, using the direct phase voltage measurement as feedback (Sect. 2.3). The control can be performed directly in the α–β (stator) reference frame, by using two proportional integral derivative (PID) controllers; a simple feedforward compensation of the inverter dead–times, such as the

Table 4.1: Nominal parameters of the experimental motor

	PMSM1
PM arrangement	Surface Mounted
Nominal current (I_N)	9.6 A
Nominal speed ($\omega_{m,N}$)	3000 rpm
Nominal torque (τ_N)	14.1 N m
Pole pairs (p)	3
Stator resistance (R)	0.76 Ω
d–axis inductance (L_d)	2.3 mH
q–axis inductance (L_q)	4.3 mH
PM flux linkage (Λ_{mg})	0.242 V s

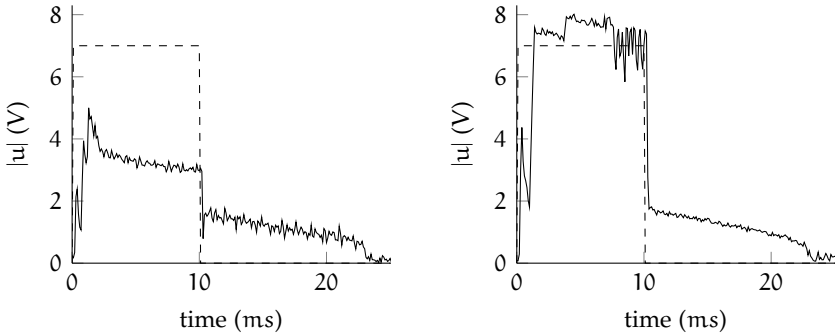

Figure 4.5: Actual voltage pulse shapes generated by the inverter: (a) with no voltage measurement; (b) with direct phase voltage measurement.

step compensation described in Sect. 2.2, can be added to the control scheme, in order to speed up the response.

4.1.2 *Experimental tests*

The experimental tests have been carried out on two different motors, whose nominal data are reported in Table 4.1 and in Table 3.3. The first one is a surface mounted PMSM, namely PMSM1, while the second is an IPM-PMSM with a large saliency, namely PMSM2. All the tests have been performed with a 150 V DC bus, in order to keep the voltage measurement error reasonably small, given the hardware limitations (i.e. 100 samples/PWM cycle) of the measurement system used for the experiments.

The shape of the generic voltage pulse applied during the estimation procedure is shown in Figure 4.5, under different operating conditions. The pulse of Figure 4.5a refers to the open-loop case. To

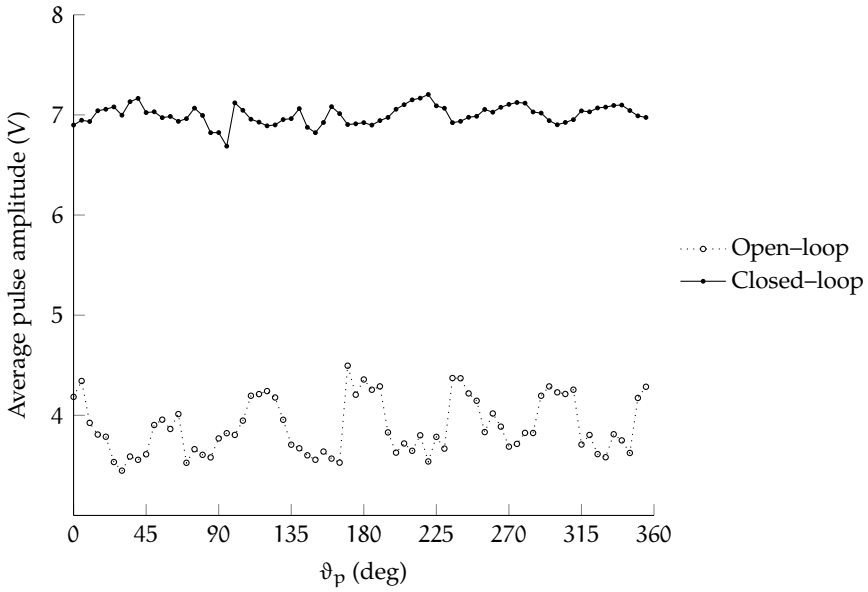

Figure 4.6: Average pulse voltage vs pulse direction (over an electrical period).

guarantee a closer match between the commanded voltage reference (dashed line) and the actual pulse voltage (solid line), a step dead time (DT) compensation procedure was implemented in the inverter. As shown in Figure 4.5b, the quality of the compensated output voltage in closed loop control (continuous line) is drastically improved. Finally, Figure 4.6 reports the superior quality of the closed loop control on the voltage pulse over an entire electrical period of the motor.

In principle, the compensation of the dead–times could be avoided adopting a closed–loop control strategy: however, its inclusion in the control scheme reduces the transient response. An improvement consists in applying the voltage vector reference as a feedforward (FF) term, and use the PID controller only to correct the deviations from the setpoint. Only in case of Figure 4.5b, it can be stated that the pulse is actually applied with the correct amplitude and duration. Moreover, the pulse amplitude becomes almost independent on its direction, as evident in Figure 4.6, so that regular pulses can be applied over the whole electrical period.

In order to better locate the position of the two maxima of the current peak profile, the experimental data were LS fitted with a sinusoidal function of the type

$$f(\vartheta) = A \sin(\vartheta - \vartheta_A) + B \sin(2\vartheta - \vartheta_B) \tag{4.5}$$

where A, B, ϑ_A and ϑ_B are the fitting parameters. A weighted LS procedure was used to increase the fitting accuracy in the neighbourhood of the two maxima. The weights were chosen proportionally to the value of the sensed current peak at each position ϑ_p.

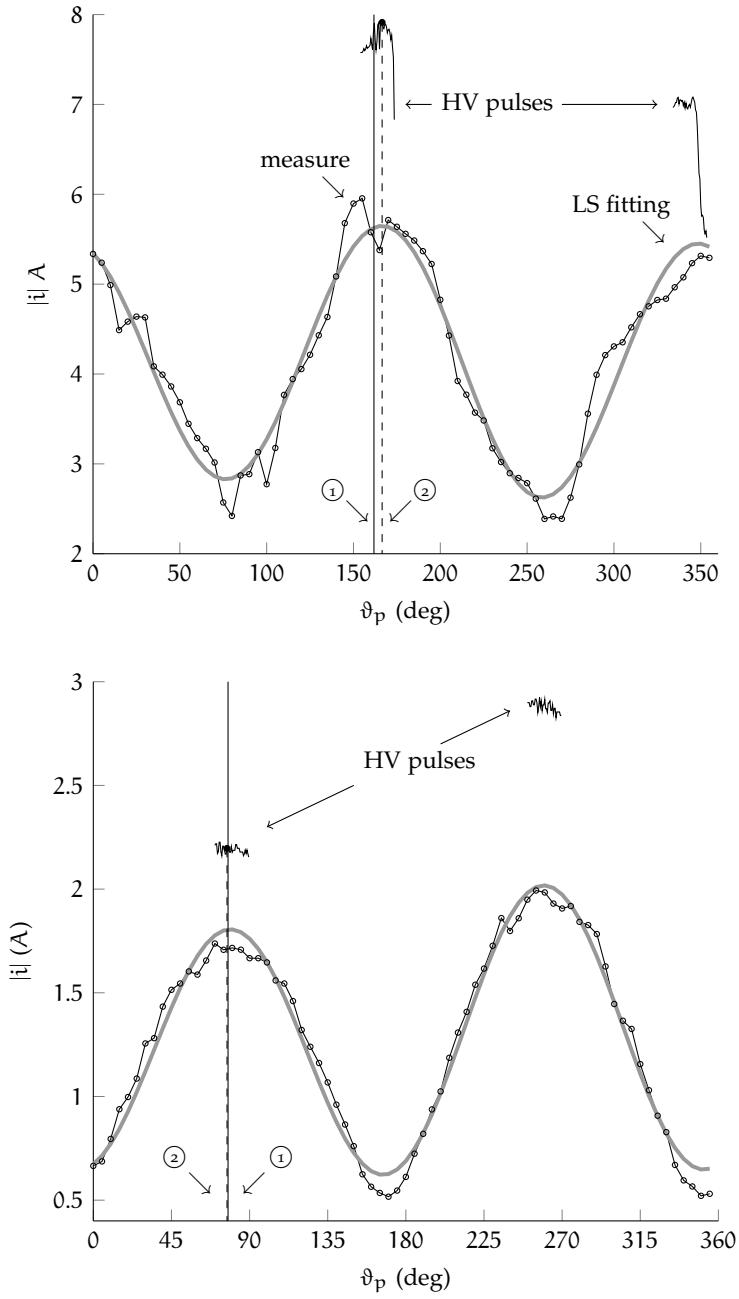

Figure 4.7: Current magnitudes with voltage pulses over an electrical period: (a) PMSM1, (b) PMSM2.

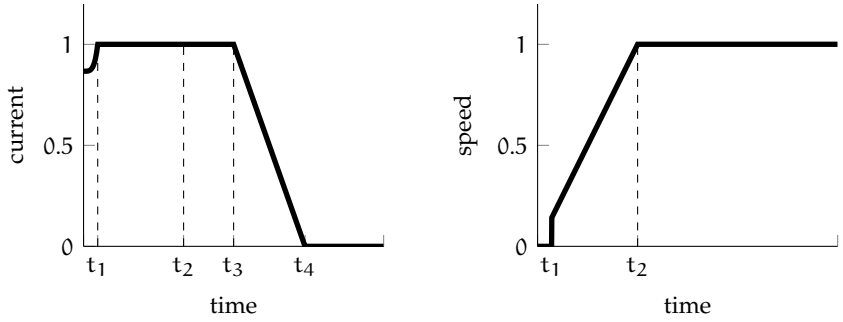

Figure 4.8: Current and speed profile during the EE startup.

The amplitude and duration of the test pulses in each case have been adjusted both to avoid noticeable rotor movements, and to enhance the current peak variations due to saliency. The estimation has been carried out by applying 36 equally spaced pulses in the $[0°, 180°]$ range; for each direction, the positive and negative oriented pulses have been applied in sequence, to reduce the rotor movement. In the procedure of Fig. 4.7, two different pulse levels have been adopted: low voltage (LV) pulses were used to get the current peak profile over an entire electromechanical angle period. Then, higher voltage (HV) pulses in a $\pm 10°$ range around the raw estimate obtained after LS fitting have been applied to potentially improve the estimate of both the rotor position and orientation. A $10\,ms$, $7\,V$ LV–pulse has been chosen for PMSM1, boosted to $7.7\,V$ in the HV case. For the PMSM2, the chosen values are $5\,ms$, $16\,V$ for the LV–pulse, and $24\,V$ for the HV–pulse. The selected values undergo the nominal motor current limit. Note that the estimated position is determined by the location of the largest peak in the PMSM1 case, and the smaller relative peak in the PMSM2. Actually, it has been verified that the saliency due to magnetic saturation is produced by the stator teeth in the former case, and the rotor iron bridge in the latter.

It can be concluded that the voltage measure is effectively exploited to generate uniform amplitude–controlled test pulses, regardless of their direction in the stator reference frame. In this way, inductance variations due to the motor saliency, which are used to infer the rotor position, can be better highlighted compared to a situation where no voltage measure is available. The experimental results confirm that the availability of a precise voltage measurement improves the detection of the PMSM initial position, extending their capability to almost all standard motor topologies.

4.2 STARTUP ALGORITHMS

The open-loop startup proposed by Blaabjerg *et al.* [106] is considered and further improved in this work. The motor is accelerated from standstill till a certain speed by following a ramp frequency or speed command. In order to accelerate the motor, a specific current magnitude, synchronous to the rotor frame, is imposed and maintained, obtaining the so called I-f control. The current and speed profiles are sketched in Figure 4.8a and 4.8b. The I-f control increases the safety in sensorless drives since the current is controlled during the startup process, conversely to the V-f (also called V-Hz control) where the current is uncontrolled.

The startup procedure consists of the following phases:

1. *Initial rotor alignement*: at the startup, the rotor position must be known. There are two possibilities:
   - the rotor is aligned with one of the motor phase axes (typically the a–phase), by applying a DC current to the stator windings;
   - the initial position is estimated, for instance with the technique reported in Sect. 4.1.

2. *Acceleration phase:* denote with d^*q^* a reference frame to be tracked by the actual dq frame (synchronous with the rotor flux). The d^*q^* reference frame is initially set to be lagging the real dq frame by an angle equal to 90° (i.e. its q^* axis is aligned with the rotor d-axis determined through the initial alignment procedure), and it is rotated with a speed ramp reference ω_m^* (Figure 4.9a). During the whole startup procedure, the q^*–axis current is maintained at a constant value, while the d^*–axis current is set to zero. As soon as the the d^*q^* starts to rotate, the (load) angle ϑ_L between the two reference frames becomes smaller, and correspondingly the q–axis current component, given by $i_q = i_q^* \cos\vartheta_L$, grows up. When this current is large enough to overcome the load torque, the rotor starts to rotate, thus following the imposed speed reference. As long as the the d^*q^* frame is lagging the dq frame by a positive load angle ϑ_L, the I–f starting procedure exhibits a self–stabilising capability. In fact, the electromagnetic torque is:

$$\tau = \frac{3}{2} p i_q^* \cos\vartheta_L \left[\Lambda_{mg} + (L_d - L_q) i_q^* \sin\vartheta_L\right] \approx \frac{3}{2} p i_q^* \cos\vartheta_L \quad (4.6)$$

where the last approximation is licit as long as the reluctance torque component is negligible compared to the electromagnetic one, i.e. $\Lambda_{mg} \gg (L_d - L_q) i_q^* \sin\vartheta_L$. Consider the case when the rotor decelerates, for example because of an increased load torque: then, the load angle decreases, and because of (4.6), the

torque increases, thus producing the required acceleration to track the desired speed ramp reference. Note that the self-stabilising mechanism is lost when the d^*q^* frame leads the dq frame, i.e. $\vartheta_L < 0$. This situation can be avoided by imposing a sufficiently large q^*–axis reference current, so that a significant torque can be produced even by maintaining the d^*q^* frame almost in quadrature with the dq one.

3. *Constant speed phase with smooth transition to sensorless control:* when the rotor reaches a sufficiently high speed so that the BEMF can be reliably detected by the position observer described in Sect. 4.3, the control should be switched to the sensorless scheme. A *bumpless* transfer strategy must be implemented, since the current commands provided by the I–f and the sensorless control are typically not matched at the switching instant. This is implemented as follows
   - during the acceleration phase, the position observer is enabled as soon as the BEMF can be reliably detected;
   - at the end of the acceleration phase, i.e. when a desired speed reference value is reached, the speed reference ω_m^* is kept constant;
   - the q^*–axis reference current is slowly decreased, so that the d^*q^* becomes closer and closer to the actual dq frame. In this way, the q^*–axis current approaches the value generated by the conventional FOC, while the d^*–axis current reduces to zero.
   - while the q^*–axis current is slowly decreased, the estimate of the load angle $\hat{\vartheta}_L = \hat{\vartheta}_{me} - \vartheta_{me}^*$ (where $\hat{\vartheta}_{me}$ is the position estimate provided by the observer, and ϑ_{me}^* is the position reference of the d^*q^* frame) is monitored. When $\hat{\vartheta}_L$ is below a certain threshold, i.e. when the d^*q^* is almost aligned with the actual dq frame and the I–f operates almost in the same conditions of a conventional FOC, the transition to the sensorless control can be reliably performed without incurring to excessive current and torque ripples.

In Sect. 4.2.1 and 4.2.2, the isotropic and anisotropic startup design procedures are reported, one after the other.

4.2.1 *SPM*

In case of an SPM motor without load, the following equation holds:

$$J\ddot{\vartheta}_m = K_T i_q \cos(\vartheta_{me} - \vartheta_{me}^*) \tag{4.7}$$

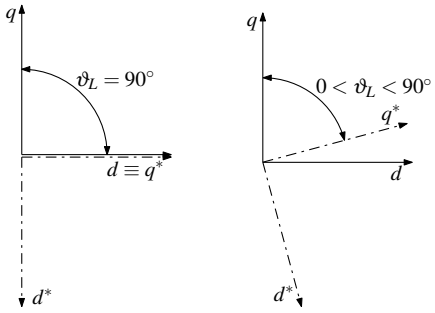

Figure 4.9: Reference frames orientation in I–f control: (a) initial alignment; (b) during acceleration and constant speed phases.

In $t \in [0, t_1]$ of Figure 4.8a, the electromechanical speed reference ω^*_{me} is kept to zero as well as the electromechanical position reference ϑ^*_{me}. On the other hand, the reference current is set to get the desired torque and it is increased till t_1 to compensate the actual rotation of the rotor due to the so produced torque. The acceleration of the motor is a design parameter equal to the speed ramp slope K_ω. Therefore:

$$\ddot{\vartheta}_m = K_\omega$$

It follows that:

$$\omega_m = K_\omega t \qquad \vartheta_m = \frac{1}{2} K_\omega t^2 \tag{4.8}$$

Since K_ω and K_T are known and ϑ^*_{me} is kept to zero, the i^*_q reference is obtained from (4.7) as:

$$i^*_q = \frac{J\ddot{\vartheta}_m}{K_T \cos\left(\frac{p}{2} K_\omega t^2\right)} = \frac{JK_\omega}{K_T \cos\left(\frac{p}{2} K_\omega t^2\right)} \tag{4.9}$$

where p is the number of pole pairs of the motor.

In case of load, (4.7) is revisited as follows:

$$\tau_L + J\ddot{\vartheta}_m = K_T i_q \cos(\vartheta_{me} - \vartheta^*_{me}) \tag{4.10}$$

where τ_L represents the load torque. It may be seen from (4.10) that the nature of the load is not considered. In order to design the speed ramp slope, two assumptions are necessary. First, a known inertia J should be assumed. Second, a maximum load torque $\tau_{L,max}$ should be fixed. It follows that (4.9) becomes:

$$i^*_q = \frac{\tau_{L,max} + J\ddot{\vartheta}_m}{K_T \cos\left(\frac{p}{2} K_\omega t^2\right)} = \frac{\tau_{L,max} + JK_\omega}{K_T \cos\left(\frac{p}{2} K_\omega t^2\right)} \tag{4.11}$$

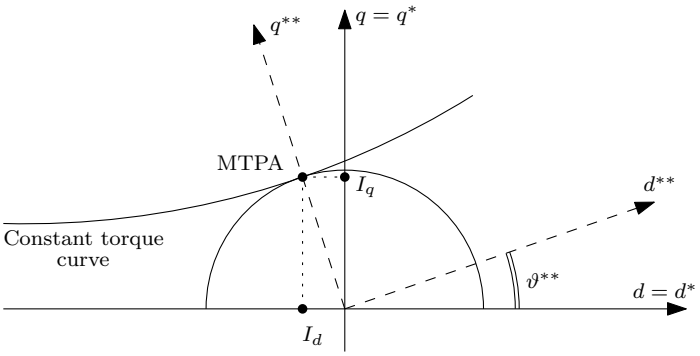

Figure 4.10: Reference frame at the startup and MTPA rotation angle definition.

4.2.2 *IPM*

In case of an IPM motor, both electromagnetic and reluctance torques cooperate to move the rotor. The torque equation at steady state is:

$$T = \frac{3p}{2}\left[\Lambda_{mg} I_q + (L_d - L_q) I_d I_q\right] \tag{4.12}$$

From (4.12), it comes out that infinite solutions of (I_d, I_q) allow to obtain the same desired amount of torque. To overcome this issue, the MTPA is used to get the initial starting value.

The MTPA condition is obtained once the following equation is satisfied:

$$\frac{\partial \tau}{\partial i_d} = 0 \tag{4.13}$$

Therefore, bearing in mind that $I = \sqrt{I_d^2 + I_q^2}$, (4.13) is satisfied by the following I_d:

$$I_d = \frac{\Lambda_{mg} \pm \sqrt{\Lambda_{mg}^2 + 8(L_d - L_q)^2 I^2}}{-4(L_d - L_q)} \tag{4.14}$$

In order to get positive torque from (4.12), the negative solution of (4.14) shall be used. Finally, the I_q value is obtained from the current magnitude I.

The MTPA information can be fruitfully used to get a different start-up design. In fact, in an ideal condition, the estimated reference frame d^*q^* is known and it coincides with the actual one dq , Figure 4.10. The hypothesis is not very far from reality, provided that an initial position estimation algorithm is implemented and it guarantees good results. Thus, once the maximum load $\tau_{L,max}$ is known, it is possible to calculate the current references and the initial position offset ϑ^{**} as defined in Figure 4.10. The motor starts exploiting the maximum torque with the minimum current magnitude.

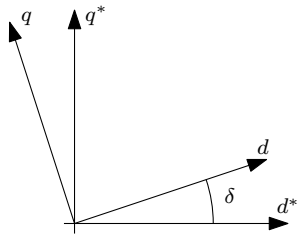

Figure 4.11: Definition of the desired displacement angle

As soon as the motor gathers momentum, though, the hypothesis that the d^*q^* reference frame is aligned with the actual one is not holding any more. The actual rotor position is unknown until the BEMF based position estimator takes over the control. It is desirable to maintain a safety displacement angle δ between the open-loop reference frame and the actual one. Therefore, the current profile is designed in order to compensate the growing misalignment by increasing its magnitude for the first instants, till t_1, Figure 4.8b. In the time interval $[0, t_1]$, it is supposed that the motor accelerates with K_ω. Hence, the displacement angle δ can be described by the law:

$$\delta = \frac{1}{2} K_\omega t^2 \tag{4.15}$$

where t is the time. During this time interval, the speed reference ω^* is kept null, while it shall be calculated from K_ω after the instant t_1, Figure 4.8.

The startup algorithm was tested on an experimental rig equipped with a PMSM motor. Mechanical parameters, estimated as in Sect. 3.2, were used to design the experimental test reported in Figure 4.12. For the sake of simplicity, the motor under test was controlled as an isotropic motor, i.e. only $i_d = 0$. The motor is started with the desired i_q reference and soon the magnitude is changed to get the desired δ, (4.15). During the ramp, the position observer is enabled at 0.3 s and the speed is correctly estimated. When the motor reaches the desired speed reference, the current magnitude is decreased until the position threshold is overpassed. The speed control is enabled at 1 s, where an i_q peak can be observed in Figure 4.12a due to the error between the estimated speed and the reference value. The current peak is thus limited by the speed controller output limitations. The BEMF observer was activated at 250 rpm to guarantee a good signal-to-noise ratio between the voltage measurement and the BEMF magnitude. The experimental tests carried out in the following sections have shown that the latter value could be decreased down to very small speeds when the voltage measurement system is adopted. The observer could be enabled after t_1 (Figure 4.8b), allowing the speed control activation even before the ramp reference has ended.

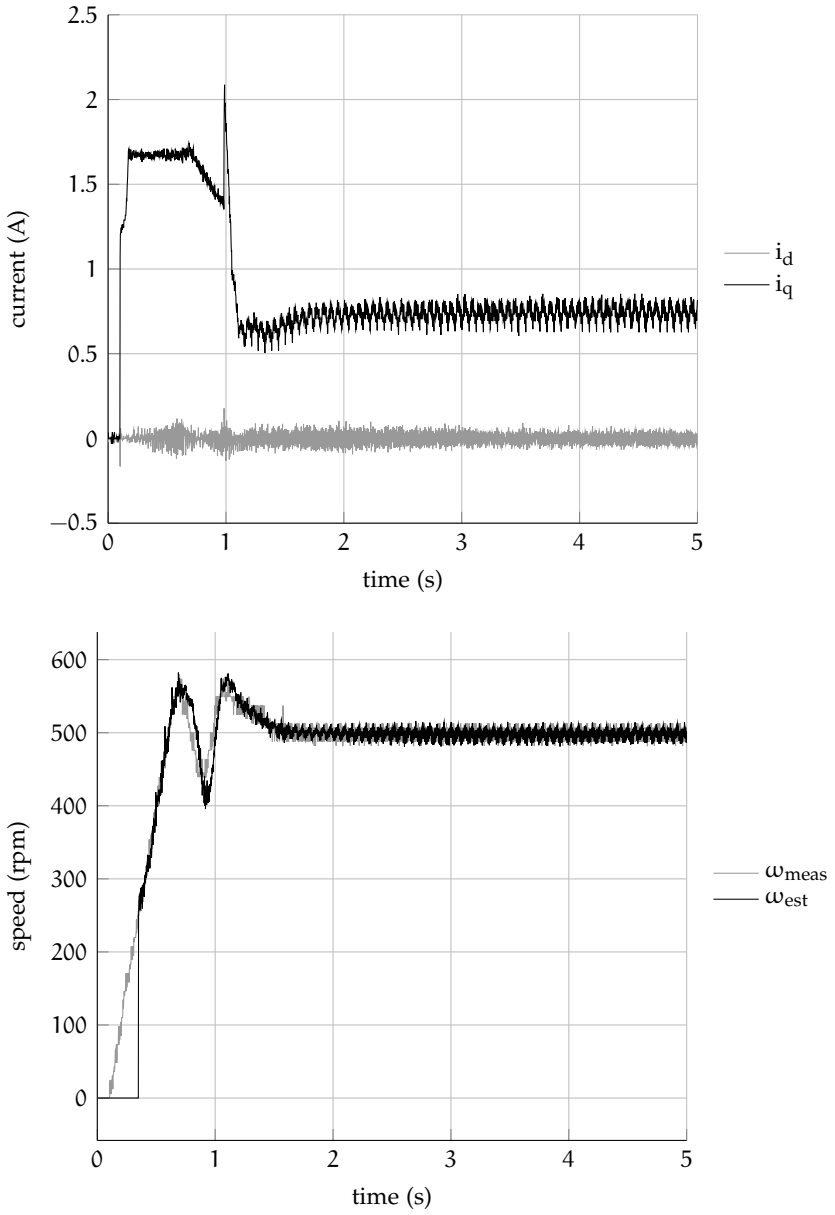

Figure 4.12: Current and speed measurements during the EE startup at no load. The speed control uses the observed speed at 1 s.

4.3 ANALYSIS AND DESIGN OF A PLL-BASED SENSORLESS

The voltage model of the IPM motor is:

$$\begin{aligned} u_d &= Ri_d + \frac{d\lambda_d}{dt} - \omega_{me}\lambda_q \\ u_q &= Ri_q + \frac{d\lambda_q}{dt} + \omega_{me}\lambda_d + \omega_{me}\Lambda_{mg} \end{aligned} \tag{4.16}$$

A first approximation consists on neglecting possible magnetic saturations, i.e. $\lambda(i,t) = Li$, which yields:

$$\begin{aligned} u_d &= Ri_d + L_d\frac{di_d}{dt} - \omega_{me}L_q i_q \\ u_q &= Ri_q + L_q\frac{di_q}{dt} + \omega_{me}L_d i_d + \omega_{me}\Lambda_{mg} \end{aligned} \tag{4.17}$$

Equations (4.16) can be derived from (4.16) by using:

$$\lambda_{dq} = \begin{bmatrix} L_d & 0 \\ 0 & L_q \end{bmatrix} \begin{bmatrix} i_d \\ i_q \end{bmatrix} \tag{4.18}$$

In sensorless techniques, equations (4.17) are widely used thanks to their simplicity. However, many drawbacks arise from their use:

1. reference voltages u_d^* and u_q^* are used instead of the real ones;
2. uncertainty on motor parameter values;

On the other hand, the use of (4.16) is very problematic, because of the λ_d and λ_q characterization. Therefore, let us first analyse the use of (4.17) in a PLL scheme to estimate the BEMF of an IPM motor. For more insights about PLL, please refer to [1].

The PLL proposed in [52] has been adopted in this work and it goes by the name of dq -PLL. However, several differences arise because sensorless operations are quite different from the typical power electronic application. For example, in power converters the frequency of the signals are almost constant and the PLL is required to track this little frequency variations with great precision. Conversely, electric drives applications work on a wide range of frequency. Frequency variations happen all the time in an unpredictable way, especially with load variations. Therefore, the design of a performing PLL is not a trivial task or a mere transposition of the existing one.

4.3.1 *PLL on the Back-Electromotive Force: simplified approach*

In order to effectively use the PLL, (4.17) is written as follows:

$$\begin{aligned} \hat{e}_d &= 0 = \hat{u}_d^* - \hat{R}\hat{i}_d - \hat{L}_d\frac{d\hat{i}_d}{dt} + \hat{\omega}_{me}\hat{L}_q\hat{i}_q \\ \hat{e}_q &= \omega_{me}\Lambda_{mg} = \hat{u}_q^* - \hat{R}\hat{i}_q - \hat{L}_q\frac{d\hat{i}_q}{dt} - \hat{\omega}_{me}\hat{L}_d\hat{i}_d \end{aligned} \tag{4.19}$$

where $\hat{d}\hat{q}$ is the estimated reference frame by the PLL. As it will be shown in the next section, the equations above neglect several terms, while they consider only the projection of the actual BEMF on the estimated $\hat{d}\hat{q}$ reference frame. The relation between dq and $\hat{d}\hat{q}$ is established by:

$$\begin{bmatrix} \hat{d} \\ \hat{q} \end{bmatrix} = \begin{bmatrix} \cos(\tilde{\vartheta}) & -\sin(\tilde{\vartheta}) \\ \sin(\tilde{\vartheta}) & \cos(\tilde{\vartheta}) \end{bmatrix} \begin{bmatrix} d \\ q \end{bmatrix} \tag{4.20}$$

Derivative terms in (4.19) are tricky objects to handle. In fact, the derivative of a measured quantity, i.e. the current, is affected by measurement noise which could cause the derivative to explode. Therefore, the following procedure is proposed instead:

1. get the integrals of (4.19);
2. get the derivatives of the BEMF in $\hat{d}\hat{q}$.

The first integral calculation has a low pass filtering effect which returns a smoother derivative calculation. The first move gives:

$$\begin{aligned} \int \hat{e}_d \, dt &= \int \left(\hat{u}_d^* - \hat{R}\hat{i}_d + \hat{\omega}_{me}\hat{L}_q\hat{i}_q \right) dt - L_d\hat{i}_d \\ \int \hat{e}_q \, dt &= \int \left(\hat{u}_q^* - \hat{R}\hat{i}_q - \hat{\omega}_{me}\hat{L}_d\hat{i}_d \right) dt - L_q\hat{i}_q \end{aligned} \tag{4.21}$$

The BEMF is obtained by derivation of the integrals (4.21). One of the advantages of using the PLL proposed in [52] is that all the quantities are in dq , i.e. constant at steady state operations. A simple integrator can thus be used, remembering that the final implementation requires a discrete algorithm (for more insight please refer to [30]).

4.3.2 *PLL design*

In order to properly design the PLL, a deeper study on the control loop is necessary. In fact, the assumptions made in the previous section neglect many aspects which concern the convergence of the PLL to the right value even in presence of disturbances, large frequency variations and motor anisotropies. The goal is to describe the dq -PLL as similar as possible to the canonic one in Figure 4.13a, in order to take advantage of the control theory widely present in the scientific literature. For instance, the dq -PLL proposed in [52] is sketched in Figure 4.13b. An approach similar to the one proposed in [29] is used. The system to be considered is the one in Figure 4.14. The following points need to be sorted out:

- identify the phase detector strategy;
- define the proper filter;

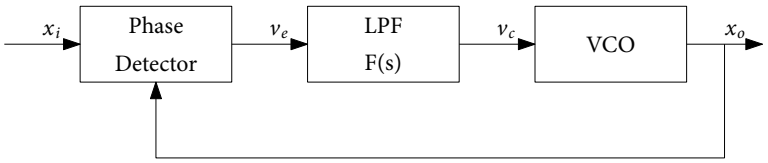

(a) Standard PLL

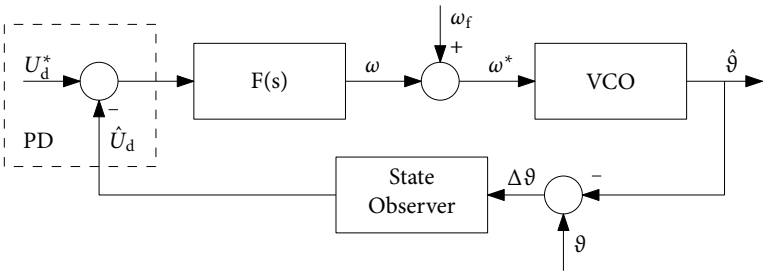

(b) dq-PLL structure proposed by [52]

Figure 4.13: PLL structures.

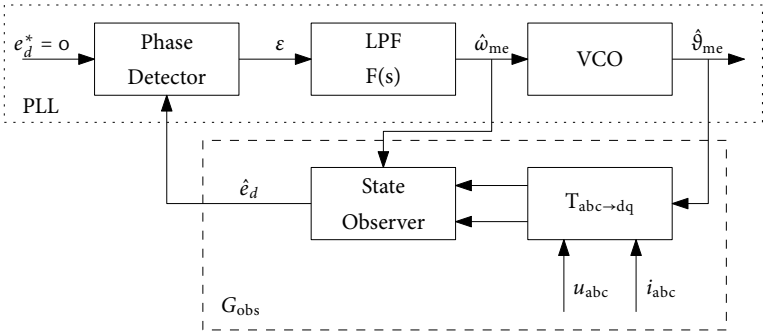

Figure 4.14: dq-PLL for BEMF estimation.

- define the voltage controlled oscillator (VCO);
- describe the transfer function G_{obs}.

The phase detector strategy is simpler than the standard PLL and it is the same one used in [52]. With a dq -PLL, it is possible to implement different regulators. Being in a synchronous reference frame means that, at steady state, all quantities are constant. The d-axis BEMF estimation error is constant, too, and it is proportional to the speed. A proportional gain would be enough to cancel the constant error. A proportional control is not sufficient during transients, though, and also when the motor model is not linear. The transfer function G_{obs} (Figure 4.14) will be defined based on the motor model and differs whether isotropic or anisotropic motors are adopted.

4.3.2.1 *Motor model for BEMF-PLL*

Consider the dynamic equations of a generic PMSM in the dq reference frame synchronous with the rotor flux expressed in vectorial form:

$$u_{dq} = Ri_{dq} + L_{dq}\frac{di_{dq}}{dt} + \omega_{me}\mathbf{S}L_{dq}i_{dq} + e_{dq} \tag{4.22}$$

where

$$\mathbf{S} = \begin{bmatrix} 0 & -1 \\ 1 & 0 \end{bmatrix}$$

While working in sensorless operations, the control is based on the estimated reference frame $\hat{d}\hat{q}$ which rotates accordingly to the current rotor position estimate $\hat{\vartheta}_{me}$. The orientation of the $\hat{d}\hat{q}$ reference frame with respect to the dq one is given by the transformation matrix:

$$\mathbf{T} = \mathbf{T}_{dq/\hat{d}\hat{q}}(\Delta\vartheta) = \begin{bmatrix} \cos\Delta\vartheta & -\sin\Delta\vartheta \\ \sin\Delta\vartheta & \cos\Delta\vartheta \end{bmatrix} \tag{4.23}$$

where $\Delta\vartheta = \vartheta_{me} - \hat{\vartheta}_{me}$ is the difference between the actual and estimated rotor position. The transformation (4.23) can be used to derive the following dynamical equations of the PMSM in the $\hat{d}\hat{q}$ frame:

$$\begin{aligned} \hat{u}_{dq} = R\hat{i}_{dq} + \mathbf{T}L_{dq}\mathbf{T}^{-1}\frac{d\hat{i}_{dq}}{dt} + \dots \\ \left(\mathbf{T}L_{dq}\frac{d\mathbf{T}^{-1}}{dt} + \omega_{me}\mathbf{T}\mathbf{S}L_{dq}\mathbf{T}^{-1}\right)\hat{i}_{dq} + \hat{e}_{dq} \end{aligned} \tag{4.24}$$

By adding:

$$\pm L_{dq}\frac{di_{dq}}{dt} \qquad \pm\hat{\omega}_{me}\mathbf{S}L_{dq}\hat{i}_{dq} \tag{4.25}$$

to (4.24), the following equations is obtained:

$$\hat{u}_{dq} = R\hat{i}_{dq} + L_{dq}\frac{d\hat{i}_{dq}}{dt} + \hat{\omega}_{me}\mathbf{S}L_{dq}\hat{i}_{dq} + \hat{e}'_{dq} \tag{4.26}$$

where

$$\begin{aligned} \hat{e}'_{dq} = \left(\mathbf{T}L_{dq}\mathbf{T}^{-1} - L_{dq}\right)\frac{d\hat{i}_{dq}}{dt} + \dots \\ + \left(\mathbf{T}L_{dq}\frac{d\mathbf{T}^{-1}}{dt} + \omega_{me}\mathbf{T}\mathbf{S}L_{dq}\mathbf{T}^{-1} - \hat{\omega}_{me}\mathbf{S}L_{dq}\right)\hat{i}_{dq} + \hat{e}_{dq} \end{aligned} \tag{4.27}$$

Suppose that the PMSM is operating at steady state with constant speed ω_{me}. Since the currents in dq frame are constant, it holds that:

$$\frac{d\hat{i}_{dq}}{dt} = \frac{d\mathbf{T}_{dq/\hat{d}\hat{q}}(\Delta\vartheta)}{dt}i_{dq} = \frac{\partial\mathbf{T}_{dq/\hat{d}\hat{q}}(\Delta\vartheta)}{\partial\Delta\vartheta}\frac{d\Delta\vartheta}{dt}i_{dq} \tag{4.28}$$

Being at constant speed it holds that:

$$\frac{d\Delta\vartheta}{dt} = \omega_{me} - \hat{\omega}_{me} \tag{4.29}$$

Furthermore, it is straight to get:

$$\frac{\partial \mathbf{T}}{\partial \Delta\vartheta} = \mathbf{TS} \tag{4.30}$$

$$\frac{\partial \mathbf{T}^{-1}}{\partial \Delta\vartheta} = -\mathbf{ST} \tag{4.31}$$

Thus, the equation (4.27) can be rewritten as follows:

$$\begin{aligned}\hat{e}'_{dq} = \left(\mathbf{S}L_{dq}\mathbf{T} - L_{dq}\frac{\partial \mathbf{T}}{\partial \Delta\vartheta}\right)i_{dq}\frac{d\Delta\vartheta}{dt} + \dots \\ + \omega_{me}(\mathbf{TS}L_{dq} - \mathbf{S}L_{dq}\mathbf{T})i_{dq} + \hat{e}_{dq}\end{aligned} \tag{4.32}$$

The matrix products can be worked out as:

$$\mathbf{S}L_{dq}\mathbf{T} - L_{dq}\frac{\partial \mathbf{T}}{\partial \Delta\vartheta} = \Delta L \begin{bmatrix} \sin\Delta\vartheta & \cos\Delta\vartheta \\ \cos\Delta\vartheta & -\sin\Delta\vartheta \end{bmatrix} \tag{4.33}$$

$$\mathbf{TS}L_{dq} - \mathbf{S}L_{dq}\mathbf{T} = \Delta L \begin{bmatrix} -\sin\Delta\vartheta & 0 \\ 0 & \sin\Delta\vartheta \end{bmatrix} \tag{4.34}$$

where $\Delta L = L_d - L_q$, so that (4.32) can be expanded as follows:

$$\begin{aligned}\hat{e}'_d &= \Delta L(i_d \sin\Delta\vartheta + i_q \cos\Delta\vartheta)\frac{d\Delta\vartheta}{dt} - \omega_{me}\Delta L i_d \sin\Delta\vartheta + \hat{e}_d \\ \hat{e}'_q &= \Delta L(i_d \cos\Delta\vartheta - i_q \sin\Delta\vartheta)\frac{d\Delta\vartheta}{dt} + \omega_{me}\Delta L i_q \sin\Delta\vartheta + \hat{e}_q\end{aligned} \tag{4.35}$$

In order to linearise equations (4.35), further approximations have to be imposed. Suppose that both $\Delta\vartheta$ and $\dot{\Delta\vartheta} = d\Delta\vartheta/dt$ are small quantities. It is worth to note that such assumptions hold when the PLL is locked to the actual position of the motor. Then, (4.35) can be linearised as follows:

$$\begin{aligned}\hat{e}'_d &= f_d(0,0) + \frac{\partial f_d(0,0)}{\partial \Delta\vartheta}\Delta\vartheta + \frac{\partial f_d(0,0)}{\partial \dot{\Delta\vartheta}}\dot{\Delta\vartheta} \\ \hat{e}'_q &= f_q(0,0) + \frac{\partial f_q(0,0)}{\partial \Delta\vartheta}\Delta\vartheta + \frac{\partial f_q(0,0)}{\partial \dot{\Delta\vartheta}}\dot{\Delta\vartheta}\end{aligned} \tag{4.36}$$

where $f_d(\Delta\vartheta, \dot{\Delta\vartheta})$ and $f_q(\Delta\vartheta, \dot{\Delta\vartheta})$ are the expressions at the right-hand-side of (4.35). Finally, the linearised equations are:

$$\hat{e}'_d = -\omega_{me}\left(\Delta L i_d + \Lambda_{mg}\right)\Delta\vartheta + (\Delta L i_q)\frac{d\Delta\vartheta}{dt} \tag{4.37}$$

$$\hat{e}'_q = \omega_{me}\Lambda_{mg} + (\omega_{me}\Delta L i_q)\Delta\vartheta + (\Delta L i_d)\frac{d\Delta\vartheta}{dt} \tag{4.38}$$

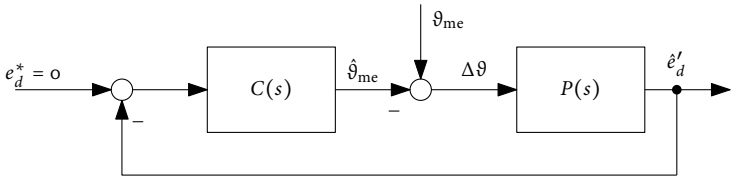

Figure 4.15: Conceptual block diagram of the BEMF-based position observer.

Consider equation (4.37) at steady state. It is important to note that the condition $\hat{e}'_d = 0$ implies that $\Delta\vartheta = 0$. The observer error $\Delta\vartheta$ can be eliminated by controlling the quantity $\hat{e}'_d$ to zero. For this purpose, the control scheme shown in Figure 4.15 can be adopted. To achieve perfect regulation of $\hat{e}'_d$ to zero, the controller $C(s)$ has to reject the disturbance ϑ_{me}. Since ω_{me} is supposed to be constant, the position varies as a ramp:

$$\frac{d\vartheta_{me}}{dt} = \omega_{me} \quad \Rightarrow \quad \vartheta_{me} = \omega_{me} t + \vartheta_{me,o} \tag{4.39}$$

A ramp-varying disturbance can be rejected, for the *internal model principle*, by a double integrator in the controller $C(s)$, which is the model of the disturbance to reject. Therefore, write the controller transfer function as

$$C(s) = \frac{1}{s^2} C'(s) \tag{4.40}$$

where $C'(s)$ represents a possible extra compensation term.

By means of the Laplace operator s, the relation between $\hat{e}'_d(s)$ and $\Delta\vartheta(s)$ can be expressed as:

$$G_{obs} = \frac{\hat{e}'_d(s)}{\Delta\vartheta(s)} = s\Delta L i_q - \omega_{me}(\Delta L i_d + \Lambda_{mg}) \tag{4.41}$$

which has one zero depending on actual speed and current magnitude. The expression of G_{obs} corresponds to the plant transfer function $P(s)$ in Figure 4.15. At first glance, equation (4.41) appears unstable. However, the observer stability involves further considerations that will be explained and evaluated in Sec. 4.3.4.

It is important to note that few hypotheses lead back the (4.41) to the correspondent one in [29]. In particular, it is enough to consider that:

- with SPM motors, the term $\Delta L = L_d - L_q$ is zero;
- with FOC control, i_d is driven to zero;
- $\Delta\vartheta = \vartheta_{me} - \hat{\vartheta}_{me}$.

If this is the case, (4.41) can be simplified into:

$$G_{obs} \approx -\omega_{me}\Lambda_{mg} \tag{4.42}$$

It is worth highlighting that i_d is regulated to zero in FOC based control, while it is negative in MTPA ones. However, the phase behaviour of the frequency response associated with $G_{obs}(s)$ is as follows:

1. case $\Delta L = 0$ (*isotropic PMSM case*): $G_{obs}(s)$ consists in a pure double integrator with positive gain, thus providing a constant $-\pi$ phase;
2. case $\Delta L < 0$ (*anisotropic PMSM case*): in addition to the double integrator, $G_{obs}(s)$ has a zero that can be either a *minimum phase* or a *non-minimum phase* zero, depending upon the i_q sign. The worst case is when $i_q < 0$, which means the zero producing a phase lag of $\pi/2$ at high frequency. Therefore, the phase of $G_{obs}(s)$ is equal to $-\pi$ at low frequency, while, at high frequency, it approaches $-\pi/2$ when $i_q > 0$ or $-3/2\pi$ when $i_q < 0$.

4.3.3 *Robust design for isotopic motors*

In order to carry out a robust design, the worst case should be accounted for the PLL action. For isotropic motors, i.e. motors where both d- and q-axis inductances can be considered equal, the plant transfer function is (4.42). Considering the nature of the disturbance to reject and the plant transfer function, the loop transfer function can be written as[1]:

$$L(s) = -C(s)P(s) = C'(s)\frac{G_{obs}}{s^2} \tag{4.43}$$

where $C'(s)$ is the controller to be defined to get the desired PLL performances. Since the plant and the double integrator introduce a constant phase delay of $-\pi$, the $C'(s)$ has to add a phase lead action to get the desired phase margin at the desired crossover frequency. Therefore, two possibilities arise for achieving the such phase lead action.

- PI^2, i.e. a standard PI with an additional integral action to get the double integral action needed for the IMC control;
- phase-lead compensator to gain the desired phase margin at the design crossover frequency.

4.3.3.1 *Robust PI^2 controller design*

The PI^2 controller is defined as:

$$C(s) = \frac{k_P s + k_I}{s^2} \tag{4.44}$$

1 The - sign in the definition of the loop transfer function (4.43) is due to the fact that the output of C(s) is the estimated angular position $\hat{\vartheta}_{me}$, while input of the plant P(s) is $\Delta\vartheta = \vartheta_{me} - \hat{\vartheta}_{me}$ (see Figure 4.15).

where the double integrator of (4.43) is included into the PI^2 structure. The desired phase margin $\varphi_m \in (0, \pi/2)$ has to be set at the desired gain crossover frequency ω_{gc}. Equation (4.42) has to be considered for the robust control design as it corresponds to the worst case. Then, the following condition must hold:

$$L(j\omega_{gc}) = -P(j\omega_{gc})C(j\omega_{gc}) = (\omega_{me}\Lambda_{mg})\left(\frac{k_P j\omega_{gc} + k_I}{-\omega_{gc}^2}\right) = e^{j(-\pi+\varphi_m)} \tag{4.45}$$

which means that at ω_{gc} the magnitude should be 1 and the phase equal to $(-\pi + \varphi_m)$. That explains the last equality, where the complex exponential is used to represent the desired magnitude and phase of the open-loop transfer function $L(j\omega)$. The desired specifications on the control design yield[2]:

$$k_P = -\frac{\omega_{gc}}{(\omega_{me}\Lambda_{mg})}\sin(-\pi+\varphi_m) \qquad k_I = -\frac{\omega_{gc}^2}{(\omega_{me}\Lambda_{mg})}\cos(-\pi+\varphi_m) \tag{4.46}$$

Equation (4.46) shows that the PI^2 gains depend on the quantity $\omega_{me}\Lambda_{mg}$, so they depend on the BEMF. This quantity is not known a priori and it varies with the motor speed. In order to compute the gains in (4.46), in turn, two options are available:

1. fixed a value for ω_{me} and compute the gains;
2. estimate $\omega_{me}\Lambda_{mg}$ from $\hat{e}'_q$ and use it in (4.46).

The former option implies that the performances of the control loop (bandwidth and robustness) will change with the PMSM speed. The second option, though, allows to obtain the desired performances as long as $\Delta\vartheta$ is small and the approximation $\hat{e}'_q \approx \omega_{me}\Lambda_{mg}$ holds true. If this latter option is adopted, the block diagram of the resulting BEMF-based position observer is that of in Figure 4.16.

From Figure 4.16 it is worth to note that:

- a feedforward term ω_c is introduced to speed up the convergence to zero of the observer error. A mechanical models of both motor and load should be available. In this case, a *full-order observer* is obtained;

2 The complex exponential $\rho e^{j\theta}$ is, by means of Euler's formula, equal to:

$$\rho e^{j\theta} = \rho(\cos(\theta) + j\sin(\theta))$$

the (4.46) can be worked out by re-writing (4.45) as follows:

$$(\omega_{me}\Lambda_{mg})\left(\frac{k_P j\omega_{gc} + k_I}{-\omega_{gc}^2}\right) = -(\omega_{me}\Lambda_{mg})\frac{k_I}{\omega_{gc}^2} - j(\omega_{me}\Lambda_{mg})\frac{k_P}{\omega_{gc}}$$

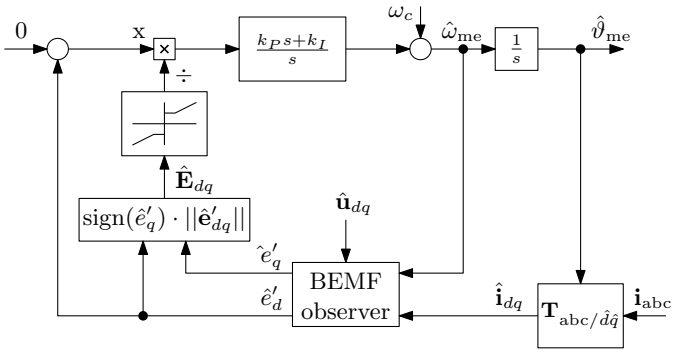

Figure 4.16: PLL with linearisation

- the PI^2 gains are adjusted according to the estimated value $\hat{\tilde{E}}_{dq}$ of the BEMF magnitude (including the speed sign):

$$k_P = k'_P/f(\hat{\tilde{E}}_{dq}), \qquad k_I = k'_I/f(\hat{\tilde{E}}_{dq}) \tag{4.47}$$

where

$$\hat{\tilde{E}}_{dq} = \text{sign}(\hat{e}'_q)\cdot\|\hat{\tilde{e}}'_{dq}\| \tag{4.48}$$

The function $f(\cdot)$ should be selected in order to avoid division by zero. Thus it is defined as:

$$f(x) = \begin{cases} x & \text{if} \quad |x| \geqslant x_0 \\ x_0 & \text{if} \quad 0 \leqslant x < x_0 \\ -x_0 & \text{if} \quad -x_0 < x < 0 \end{cases} \tag{4.49}$$

4.3.3.2 *Design with phase-lead compensator*

A phase-lead compensator suits the specifications, i.e. a ramp disturbance rejection and gain the desired phase margin at the design crossover frequency, and can be easily designed. It does therefore represent another possibility to get the desired phase lead action. Its expression is:

$$C'(s) = k\frac{1+\tau s}{1+\alpha\tau s} \tag{4.50}$$

where k, τ and α are the design parameters. Thus, the controller transfer function is:

$$C(s) = \frac{k}{s^2}\frac{1+\tau s}{1+\alpha\tau s} \qquad \text{with} \qquad k>0,\ \tau>0,\ 0<\alpha<1 \tag{4.51}$$

Compared to (4.44), the controller (4.51) shows an increased attenuation at high frequency, i.e. a $-40\,\text{dB/dec}$ roll-off instead of the $-20\,\text{dB/dec}$ of the PI^2 case. Hence, a better noise rejection capability is expected.

The design specifications are set with a certain phase margin m_ϕ at the desired crossover frequency ω_{gc}. It holds then:

$$\omega_{gc} = \frac{1}{\alpha\tau} \tag{4.52}$$

$$m_\phi = \arcsin\left(\frac{1-\alpha}{1+\alpha}\right) \tag{4.53}$$

from which α can be sorted out as:

$$\alpha = \frac{1-\sin(m_\phi)}{1+\sin(m_\phi)} \tag{4.54}$$

Equation (4.54) allows to sort out τ as well. Last step consists on calculating the gain k of the phase-lead compensator to get $L(j\omega_{gc}) = 1$ Such condition is satisfied by the following equation:

$$k = \frac{\omega_{gc}^2}{\omega_{me}\Lambda_{mg}}\frac{\sqrt{2}}{\sqrt{1+\alpha^{-2}}} = \frac{k'}{\omega_{me}\Lambda_{mg}} \tag{4.55}$$

In practice, the quantity $\omega_{me}\Lambda_{mg}$ changes and it is therefore estimated like in Sec. 4.3.3.1. It is thus defined a variable gain k' as:

$$k' = \omega_{gc}^2\frac{\sqrt{2}}{\sqrt{1+\alpha^{-2}}} \tag{4.56}$$

4.3.4 *Observer stability*

So far, only isotropic motors have been considered in the design of the PLL. The system of Figure 4.15 needs a careful evaluation of the stability aspects when anisotropic motors are used. When the BEMF–based position observer designed for the isotropic PMSM case is applied to an anisotropic motor, the feedback loop upon which the observer is based may become unstable for certain operating conditions (i.e. certain values of the current i_q and speed ω_{me}), due to the presence of a possible non–minimum phase zero in the plant transfer function (4.41). For more insights on non-minimum phase systems, please refer to [42, Chapter 6]. The operating conditions for which the instability arises are discussed below for the two designs presented in previous Sect. 4.3.2. Then, a method to recover robust stability for any possible operating condition is presented in Sect. 4.3.5.

4.3.4.1 *PI^2 controller case*

The PI^2 based controller is considered in the following for the stability discussion. The open loop transfer function of the PLL, with plant (4.41), is equal to:

$$\begin{aligned} L(s) = C(s)P(s) &= \frac{k_P s + k_I}{s^2}\left[-\omega_{me}(\Delta L i_d + \Lambda_{mg}) + \Delta L i_q s\right] \\ &= \frac{k_P s + k_I}{s^2}(b_0 + b_1 s) \end{aligned} \tag{4.57}$$

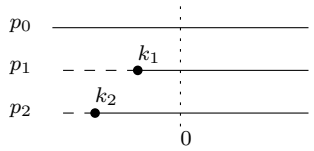

Figure 4.17: Roots of (4.58): continuous line represents positive values, while the dashed line represents negative.

where $b_0 = -\omega_{me}(\Delta L i_d + \Lambda_{mg})$ and $b_1 = \Delta L i_q$ Thus, the characteristic polynomial of the system is equal to:

$$\begin{aligned} 1 + L(s) &= \frac{(1 + k_p b_1)s^2 + (k_i b_1 + k_p b_0)s + k_i b_0}{s^2} \\ &= \frac{p_2 s^2 + p_1 s + p_0}{s^2} \end{aligned} \tag{4.58}$$

where $p_2 = (1 + k_p b_1)$, $p_1 = (k_i b_1 + k_p b_0)$ and $p_0 = k_i b_0$. For the Routh–Hurwitz criterion, a necessary and sufficient condition for the stability is that all the roots have the real part in $\Re^-$. By considering the following hypothesis:

- $\omega_{me} > 0$
- k_p and k_i both negative
- $\Delta L = L_d - L_q \leqslant 0$

the following cases hold:

- $p_0 > 0 \quad \Leftrightarrow \quad i_q \in \Re,\ id \leqslant 0$
- $p_1 > 0 \quad \Leftrightarrow \quad i_q > \dfrac{k_p \omega_{me}\left(\Delta L i_d + \Lambda_{mg}\right)}{k_i \Delta L},\ i_d \leqslant 0$
- $p_2 > 0 \quad \Leftrightarrow \quad i_q > -\dfrac{1}{k_p \Delta L},\ i_d \in \Re$

The roots signs are sketched out in Figure 4.17. It is interesting to note that two values depending on the load and motor parameters, namely k_1 and k_2, can be defined as:

$$k_1 = \frac{k_p \omega_{me}\left(\Delta L i_d + \Lambda_{mg}\right)}{k_i \Delta L} \tag{4.59}$$

$$k_2 = -\frac{1}{k_p \Delta L} \tag{4.60}$$

The condition for observer stability is:

$$i_q > i_{q,min} > \max(k_1, k_2) \tag{4.61}$$

Consider substituting (4.46) in (4.60). The system is only stable when the following equations are satisfied:

$$\frac{i_q}{\omega_{me}} > \frac{\tan(m_\varphi)}{\omega_{gc}}\left(i_d + \frac{\Lambda_{mg}}{\Delta L}\right) \tag{4.62}$$

$$\frac{i_q}{\omega_{me}} > \frac{\Lambda_{mg}}{\omega_{gc}\Delta L \sin(m_\varphi)} \tag{4.63}$$

Depending from the value of m_φ, either (4.62) or (4.63) are used to calculate $i_{q,min}$ Let assume the case $i_d = 0$. Such phase margin is equal to:

$$\bar{m}_\varphi = \arccos\left(\frac{\sqrt{5}-1}{2}\right) \approx 51.83° \tag{4.64}$$

Finally, the (4.61) becomes:

$$i_q > i_{q,min} = \begin{cases} \dfrac{\omega_{me}\Lambda_{mg}}{\omega_{gc}\Delta L}\left(\sin(m_\varphi)\right)^{-1} & 0 < m_\varphi \leqslant \bar{m}_\varphi \\ \dfrac{\omega_{me}\Lambda_{mg}}{\omega_{gc}\Delta L}\tan(m_\varphi) & m_\varphi > \bar{m}_\varphi \end{cases} \tag{4.65}$$

It is worth to note that instability arises only for negative i_q, i.e. when the motor is operating in braking mode. For the case $i_d \leqslant 0$, it is interesting to note that (4.62) decreases even more than the case $i_d = 0$, which means that the latter case represents the worst case scenario for calculating $\bar{m}_\varphi$. In other words, the lower the i_d gets, the higher $\bar{m}_\varphi$ values become.

There is still ω_{gc} that can determine instability for the system. In this case, both ω_{me} and i_q signs should be considered to get robust stability. The goal is to set a maximum crossover frequency, for given values of $\omega_{me,min}$ and $i_{q,max}$, which guarantees stability:

$$\omega_{gc} < \omega_{gc,max} \tag{4.66}$$

where:

$$\omega_{gc,max} = \min\left\{\frac{\omega_{me,min}\Lambda_{mg}}{i_{q,max}|\Delta L|}\tan(m_\phi), \frac{\omega_{me,min}\Lambda_{mg}}{i_{q,max}|\Delta L|}\frac{1}{\sin(m_\phi)}\right\} \tag{4.67}$$

As for the current in (4.65), the phase margin $\bar{m}_\varphi$ makes two cases for the maximum crossover frequency as well:

$$\omega_{gc,max} = \begin{cases} \dfrac{\omega_{me,min}\Lambda_{mg}}{i_{q,max}|\Delta L|}\tan(m_\phi) & 0 < m_\phi \leqslant \bar{m}_\phi \\ \dfrac{\omega_{me,min}\Lambda_{mg}}{i_{q,max}|\Delta L|}\dfrac{1}{\sin(m_\phi)} & m_\phi > \bar{m}_\phi \end{cases} \tag{4.68}$$

It is worth to note that $\omega_{gc,max}$ is bounded by two important values, i.e. the minimum speed $\omega_{me,min}$ and the maximum current $i_{q,max}$, that is the maximum load. Such bounds may force a too low crossover frequency value, which turns out in unacceptable performance. Therefore, other control algorithms should be considered for achieving satisfactory results.

Table 4.2: Routh-Hurwitz table for the phase lead compensator based observer

1^{st} col.	2^{nd} col.
$\alpha\tau$	$\gamma(\tau+\tau_z)$
$1+\gamma\tau\tau_z$	γ
Ψ	0
γ	0

4.3.4.2 *Phase-lead compensator case*

The stability analysis for the phase lead compensator based observer can be carried out in the same fashion as for the PI^2 based one in Sec. 4.3.4.1. By means of (4.51) and (4.41), the loop transfer function is equal to:

$$\begin{aligned} 1+L(s) &= 1+\frac{k}{s^2}\frac{1+\tau s}{1+\alpha\tau s}\left(s\Delta Li_q-\omega_{me}\left(\Delta Li_d+\Lambda_{mg}\right)\right) \\ &= \frac{s^3\alpha\tau+s^2(1+\gamma\tau\tau_z)+s\gamma(\tau+\tau_z)+\gamma}{s^2(1+s\alpha\tau)} \end{aligned} \tag{4.69}$$

where:

$$\tau_z=-\frac{\Delta Li_q}{\omega_{me}(\Delta Li_d+\Lambda_{mg})} \quad \text{and} \quad \gamma=k\omega_{me}(\Delta Li_d+\Lambda_{mg}) \tag{4.70}$$

What decides the stability of the system are the roots of the numerator in (4.69). The numerator can be rewritten as:

$$N(s)=s^3p_3+s^2p_2+sp_1+p_0 \tag{4.71}$$

where:

$$p_3=\tau\alpha \qquad p_2=1+\gamma\tau\tau_z \qquad p_1=\gamma(\tau+\tau_z) \qquad p_0=\gamma \tag{4.72}$$

In order to find out the conditions for the observer stability, the Routh-Hurwitz criterion has to be used, being the equation of third degree. The Routh-Hurwitz table is reported in Table 4.2. The observer stability is obtained if and only if all the coefficients of the first column have the same sign. It stands, by definition, that $\alpha>0$ and $\tau>0$. Therefore, the upper element of the first column is always positive for whichever value of i_q and ω_{me}. All the remaining three elements must be positive to attain stability.

The case $i_d\leqslant 0$ implies that $\gamma>0$. Hence, last element of the first column in Table 4.2 is always positive. The parameter ψ in Table 4.2 is defined as:

$$\Psi=-\frac{1}{1+\gamma\tau\tau_z}\left[\alpha\gamma\tau-\gamma(\tau+\tau_z)(1+\gamma\tau\tau_z)\right] \tag{4.73}$$

For the sake of an easier discussion, the following terms are defined:

$$\begin{aligned}\psi_1 &= \frac{1}{1+\gamma\tau\tau_z} \\ \psi_2 &= \left[\alpha\gamma\tau - \gamma(\tau+\tau_z)(1+\gamma\tau\tau_z)\right]\end{aligned} \tag{4.74}$$

It remains to sort out whether both the second and third elements of the first column in Table 4.2 are positive and at which operative conditions. The second element of the first column is positive only when:

$$1+\gamma\tau\tau_z > 0 \tag{4.75}$$

Inequality (4.75) is satisfied only for:

$$\tau_z > -\frac{1}{\gamma\tau} \tag{4.76}$$

By means of (4.52) and (4.54), condition (4.76) can be rewritten as:

$$\frac{i_q}{\omega_{me}} > \frac{\Lambda_{mg}}{\Delta L \omega_{gc}} \frac{\sqrt{1+\sin^2(m_\varphi)}}{1+\sin(m_\varphi)} \tag{4.77}$$

which relates working conditions to design parameter such as the crossover frequency ω_{gc} and the phase margin m_φ.

The analysis on the third element of the first column in Table 4.2 requires some further considerations. Firstly, it is worth to note that if (4.76) is satisfied, than ψ_1, defined in (4.74), will be consequently always positive. Therefore, ψ_2 must be negative for the third element to be positive. It means that the following condition is required:

$$\alpha\gamma\tau - \gamma(\tau+\tau_z)(1+\gamma\tau\tau_z) < 0 \tag{4.78}$$

By tiding up (4.78) with respect to τ_z it yields:

$$(\gamma^2\tau)\tau_z^2 + \gamma(1+\gamma\tau^2)\tau_z + \gamma\tau(1-\alpha) \tag{4.79}$$

The (4.78) is the equation of a parabola when both roots are real. In order to guarantee two real roots of the polynomial, the discriminant of (4.79) must be positive.

$$\Delta = \gamma^2(1+1+\gamma\tau^2)^2 - 4\gamma^3\tau^2(1-\alpha) > 0 \tag{4.80}$$

(4.80) is positive if and only if:

$$\alpha > 1 - \frac{(1+\gamma\tau^2)^2}{4\gamma\tau^2} = -\frac{(1-\gamma\tau^2)^2}{4\gamma\tau^2} \tag{4.81}$$

which is always a negative number for every $(i_q, \omega_{me}) \in \Re$. By definition, $0 < \alpha < 1$, which automatically satisfies condition (4.81). In

other words, whichever the α, there will always be two real roots for the equation (4.79). The roots are:

$$z_{1,2} = -\frac{(1+\gamma\tau^2)}{2\gamma\tau} \pm \frac{\sqrt{\Delta}}{2\gamma\tau} \tag{4.82}$$

where Δ is the discriminant defined in (4.80). One should note that:

$$\gamma(1+\gamma\tau^2) > \sqrt{\Delta} \tag{4.83}$$

Therefore, both roots lies in the left-half of the plane. In particular, the bigger root is:

$$z_2 = -\frac{(1+\gamma\tau^2)}{2\gamma\tau} + \frac{\sqrt{\Delta}}{2\gamma\tau} \tag{4.84}$$

In order to find out the condition which guarantees stability in terms of ratio i_q/ω_{me}, it is necessary to sort out whether $z_2 > -1/\gamma\tau$ or not. The latter condition can be expressed by the following inequality:

$$-\frac{\gamma(1+\gamma\tau^2)}{2\gamma^2\tau} \pm \frac{\sqrt{\Delta}}{2\gamma^2\tau} > -\frac{1}{\gamma\tau} \tag{4.85}$$

which is always verified when $\alpha > 0$. By definition, $0 < \alpha < 1$ that is z_2 is always bigger than $-1/\gamma\tau$, i.e. the third element of the first column in Table 4.2. Formally, the latter condition can be rewritten as:

$$z_2 > -\frac{1}{\gamma\tau} \qquad \forall(i_q, \omega_{me}) \in \Re \tag{4.86}$$

It is worth to note that z_2 can be expressed in the following way:

$$z_2 = -\frac{\gamma(1+\gamma\tau^2)}{2\gamma^2\tau} + \frac{\sqrt{(1-\gamma\tau^2)^2 + 4\alpha\gamma\tau^2}}{2\gamma\tau} \tag{4.87}$$

Bearing in mind the triangle inequality[3], it holds that:

$$\sqrt{(1-\gamma\tau^2)^2 + 4\alpha\gamma\tau^2} \leqslant \sqrt{(1-\gamma\tau^2)^2} + \sqrt{4\alpha\gamma\tau^2} \tag{4.88}$$

That is:

$$z_2' = -\frac{\gamma(1+\gamma\tau^2)}{2\gamma\tau} + \frac{(1-\gamma\tau^2)}{2\gamma^2\tau} + \frac{2\sqrt{\tau}\alpha\gamma}{2\gamma\tau} \geqslant z_2 \tag{4.89}$$

Thus, if it holds that $\tau_z \geqslant z_2'$, robust stability is achieved. Finally, the robust stability condition is expressed as:

$$\frac{i_q}{\omega_{me}} \geqslant \frac{\Delta L i_d + \Lambda_{mg}}{\Delta L}\left(\frac{1}{\omega_{gc}\alpha} - \sqrt{\frac{\Lambda_{mg}(\Delta L i_d + \Lambda_{mg})}{k'}\frac{1-\sin(m_\phi)}{1+\sin(m_\phi)}}\right)$$

3 The triangle inequality states that:

$$\|x+y\| \leqslant \|x\| + \|y\|$$

(4.90)

Finally, in case where i_d is controlled to zero, the proposed analysis allows to determine that:

- for a given speed ω_{me}, the feedback system is stable if and only if

$$i_q > i_{q,min} = \frac{\omega_{me}\Lambda_{mg}}{\Delta L \omega_{gc}} \frac{\sqrt{1+\sin^2(m_\varphi)}}{1+\sin(m_\varphi)} \tag{4.91}$$

  Even in this case, note that $i_{q,min} < 0$ (because, in particular, $\sin(m_\varphi) > 0$), so that the instability arises only when the motor operates in braking mode.

- to make the design stable for any current i_q and speed ω_{me}, the gain crossover frequency should be chosen smaller than

$$\omega_{gc} < \omega_{gc,max} = \frac{\omega_{me,min}\Lambda_{mg}}{i_{q,max}|\Delta L|} \frac{\sqrt{1+\sin^2(m_\varphi)}}{1+\sin(m_\varphi)} \tag{4.92}$$

  As in the previous case, this upper bound might impose an excessively small bandwidth, making the design useless in practical applications. Hence, a different approach for a robustly stable design must be pursued.

4.3.5 *PLL design for the anisotropic PMSM case*

As highlighted in previous Sect. 4.3.4, the unstable behaviour of the BEMF–based position observer arising in the anisotropic PMSM case is caused by the presence of a possible non–minimum phase zero in the plant transfer function (4.41). Since this zero pertains to the BEMF observer dynamics (4.27), it makes sense to modify it in order to have possibly no zero in the plant transfer function. In this way, the control design proposed for the isotropic PMSM case is immediately applicable, with no further modifications, to the anisotropic PMSM case, guaranteeing robust stability against any current or speed variation.

On the basis of these premises, consider the following modified BEMF observer equation:

$$\hat{\mathbf{e}}'_{dq} = \hat{\mathbf{u}}_{dq} - R\hat{\mathbf{i}}_{dq} - \mathbf{L}_{qd}\frac{d\hat{\mathbf{i}}_{dq}}{dt} - \hat{\omega}_{me}\mathbf{S}\mathbf{L}_{dq}\hat{\mathbf{i}}_{dq} \tag{4.93}$$

where

$$\mathbf{L}_{qd} = \begin{bmatrix} L_q & 0 \\ 0 & L_d \end{bmatrix} \tag{4.94}$$

By proceeding similarly to what done in Sect. 4.3.2, the following relationship can be derived between the true and estimated BEMF space vector on the $\hat{d}\hat{q}$ frame:

$$\hat{e}'_{dq} = (\mathbf{S}L_{dq}\mathbf{T} - L_{qd}\mathbf{S}\mathbf{T})\mathbf{i}_{dq}\frac{d\Delta\vartheta}{dt} + \dots + \omega_{me}(\mathbf{T}\mathbf{S}L_{dq} - \mathbf{S}L_{dq}\mathbf{T})i_{dq} + \hat{e}_{dq} \quad (4.95)$$

Given (4.94), it is immediate to verify that:

$$\mathbf{S}L_{dq}\mathbf{T} - L_{qd}\mathbf{S}\mathbf{T} = \begin{bmatrix} 0 & 0 \\ 0 & 0 \end{bmatrix} \quad (4.96)$$

so that (4.95) can be expanded as follows:

$$\begin{aligned} \hat{e}'_d &= \omega_{me}\Delta L i_d \sin\Delta\vartheta + \hat{e}_d \\ \hat{e}'_q &= \omega_{me}\Delta L i_q \sin\Delta\vartheta + \hat{e}_q \end{aligned} \quad (4.97)$$

The linearised equations for small angle errors are:

$$\begin{aligned} \hat{e}'_d &= \omega_{me}(\Delta L i_d + \Lambda_{mg})\Delta\vartheta \\ \hat{e}'_q &= \omega_{me}\Lambda_{mg} + (\omega_{me}\Delta L i_q)\Delta\vartheta \end{aligned} \quad (4.98)$$

so that the new plant transfer function is

$$P(s) = \frac{\hat{e}'_d(s)}{\Delta\vartheta(s)} = -\omega_{me}(\Delta L i_d + \Lambda_{mg}) \quad (4.99)$$

which has no zero. In practice, it coincides with that of the isotropic PMSM case when operating under standard FOC conditions (i.e. $i_d = 0$).

4.4 SENSORLESS ENHANCED BY VOLTAGE MEASUREMENT

The goal of this Section is to report experimental evidence of the sensorless algorithm proposed in Sect. 4.3. In order to carry out comparison evaluations, different voltage measurements method were considered:

- voltage references without inverter non idealities compensation;
- voltage references with compensation (ramp, Sect. 2.2.1.2, and LUT, Sect. 2.2.1.3);
- voltage measurements with the voltage measurement system proposed in Sect. 2.3.

The motor under test is the isotropic motor whose data are reported in Table 3.3. The q-axis flux is affected by magnetic saturation, as proven by the FEA analysis in Sect. 1.2, and the polynomial approximation (3.7) was used in the observer model. To get a simple evaluation of the sensorless drive, an FOC control was implemented, so that effects of magnetic saturation on the q-axis path, stator resistance and permanent magnet flux variations could be considered separately and their influence on the sensorless drives performances be evaluated.

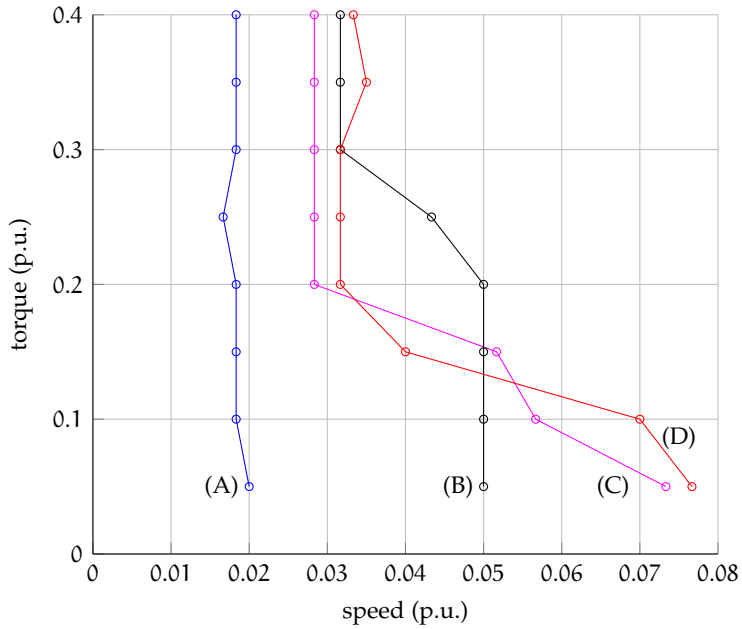

Figure 4.18: Sensorless minimum speeds with different voltage measurements: (A) with voltage measurement, (B) references without compensation, (C) references with LUT compensation and (D) references with ramp compensation

4.4.1 *Pullout curve*

During experimental activities, it has been noted that the worst working conditions for the sensorless drive were at low speed and small loads. Tests were carried out as follows:

1. load τ_L fixed at a certain level;
2. speed reference ω_m^* is slowly decreasing until motor operations are still valid.

The so obtained speed values are reported in Figure 4.18 with difference voltage measurements feeding the position observer. It is immediate to notice the superior performances obtained with the voltage measurements above all other cases.

The no load case at low speed is the worst working condition for the sensorless drive due to the really small amplitude of the voltage signals. The phase currents are small too, such that the resistance voltage drop is almost null. In case of voltage references feedback, the case with non idealities compensation suffer of the highly non linear behaviour induced by the parasitic capacitances, as explained in Sect. 2.1. The voltage references are usually ill-compensated in this region and the over (or sub) compensation turns out in a position estimation error. The voltage error, though, may be almost of the same magnitude as the signal itself, so that the introduced error can even destabilise the control. On the other hand, the use of actual voltage

measurement is insensitive to the small current magnitude effects on inverter non idealities. The bottleneck of the measurement system is represented by the accuracy as described by (2.23), which is function of the duty cycle, sampling frequency of the measurement system and DC bus voltage

4.4.2 *Load steps*

The second batch of tests carried out for the sensorless performances evaluation is the application of load steps at steady state operation. The results are reported in Figure 4.19 at a constant speed of 350 rpm, which was the lowest value allowing the sensorless operations even with a full load step. The results show that the use of voltage measurement instead of voltage references is superior in all cases.

When the compensated voltages are over-compensated, they introduce a position over-estimation error. Therefore, the estimated $\hat{d}\hat{q}$ reference frame is leading the actual one (Figure 4.20). The projections of a constant and positive $\hat{i}_q$ current in the actual dq reference frame results in a positive i_q and in a negative i_d. For an anisotropic motor, the presence of a negative i_d implies a positive contribution to the torque production. The slightly better results, in terms of dynamic performances, of Figure 4.19 are ascribable to this over-torque production, since the motor was controlled in FOC although it was anisotropic. Nonetheless, the LUT compensation works well as the current gets higher in magnitude, as confirmed by the experimental results, where the position estimation error is very close to the one obtained with the VMS.

The ramp compensation returns fairly good results till medium loads. At higher loads, the compensation fails slightly during transients due to the poor compensation. Better results can be obtained by tuning the parameter k (Sect. 2.2.1.2), by means of trial and error experiments as suggested in [50].

As expected, the results with no compensation are visibly worst than all other curves. It is important to use, at least, a simple compensation strategy as the ramp one (Sect. 2.2.1.2) to guarantee better results.

4.4.3 *Speed steps*

The performances obtained with speed step variations are reported in Figure 4.21. It is worth to highlight the superior performances of the sensorless algorithm where the position observer is fed by voltage measurement instead of compensated or non compensated voltage references. The speed steps were performed at different load conditions. As proven by the results in Figure 4.21, the sensorless algorithm bears speed steps in load condition with good results.

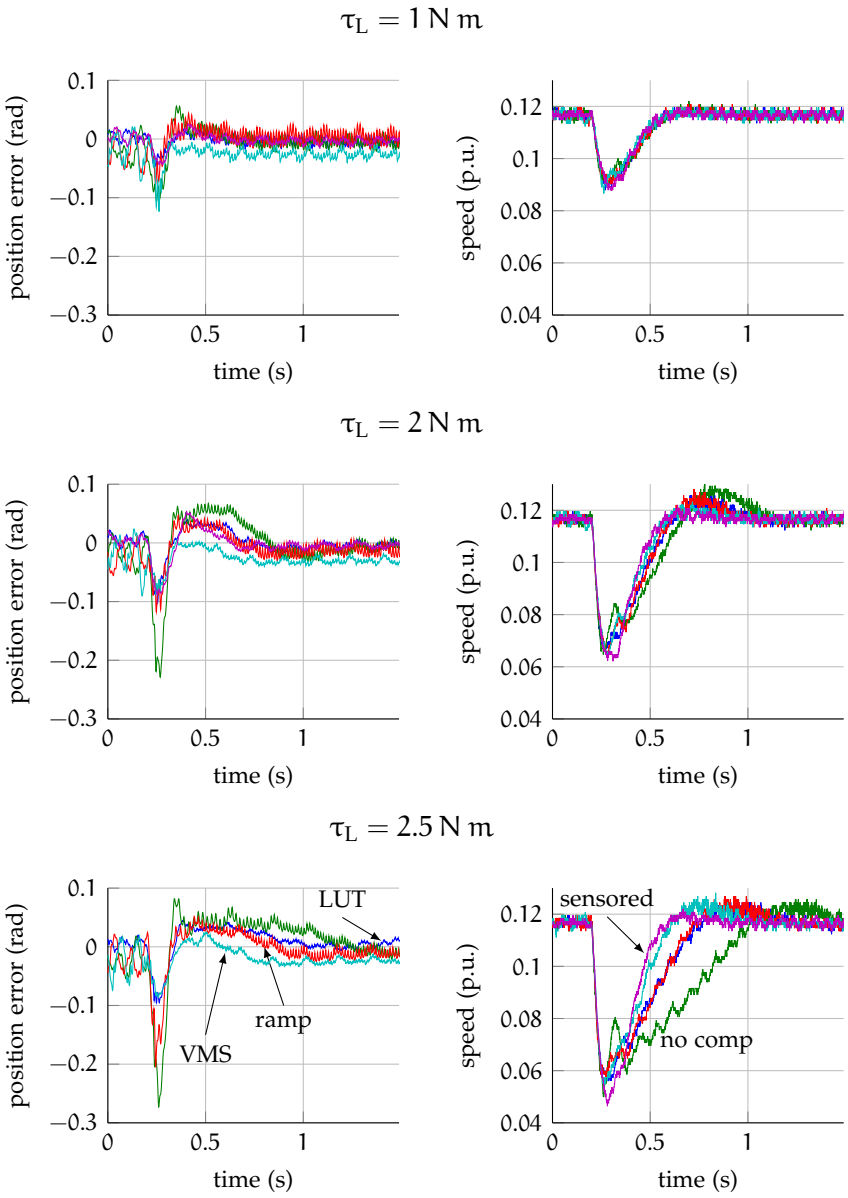

Figure 4.19: Performances of the sensorless algorithms at different load steps and different voltage feedbacks: position errors on the left column, measured speed on right column.

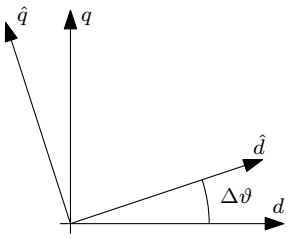

Figure 4.20: Reference frame $\hat{d}\hat{q}$ leading the actual one dq by an angle $\Delta\vartheta$ equal to the position estimation error.

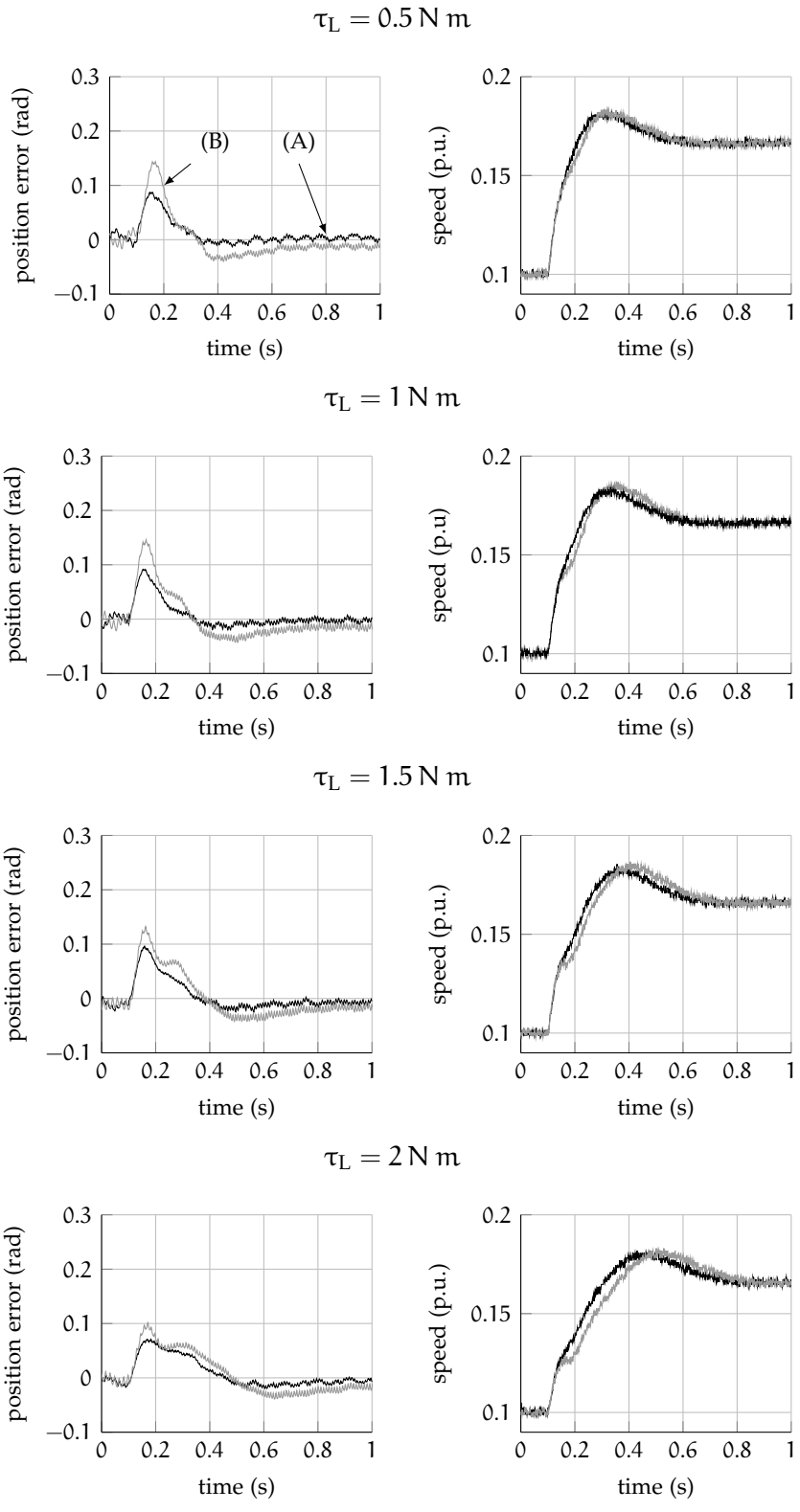

Figure 4.21: Performances of the sensorless algorithms at different speed steps from 300 rpm to 500 rpm with (A) VMS and (B) no inverter non idealities compensation

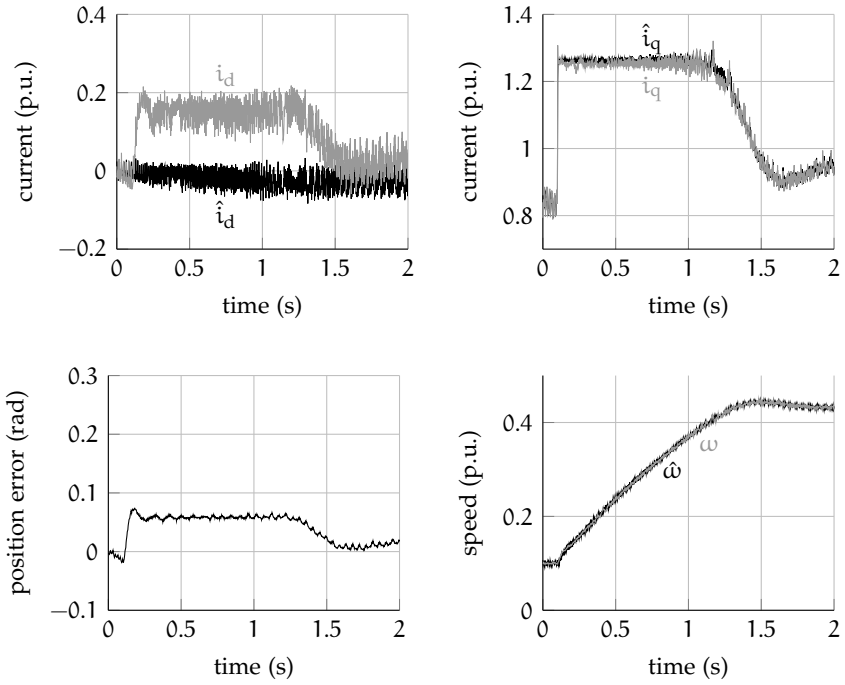

Figure 4.22: Performances of the sensorless algorithms at 80% of load and a 1000 rpm speed step.

In order to highlight the drive behaviour with a speed step in load conditions, the last test of Figure 4.21 was repeated with a larger speed step value. The results are reported in Figure 4.22, where currents in the dq reference frame are shown, too. The current magnitude[4] were limited for safety reasons at $1.25I_n$. The speed control requires the maximum available torque, thus saturating the current demand. The speed ramps up with a constant slope, being the motor producing a constant (maximum) torque to accelerate the motor. The position estimation error is constant and non null: this is in accordance with the PI^2 controller adopted in the sensorless drive, which returns a constant and finite error to type 2 inputs. The position estimation error is steered towards zero at the end of the speed ramp, once the current saturation is overcome.

4.4.4 *Parameter sensitivity*

The tests performed in Sect. 4.4.2 and 4.4.3 were repeated with errors in the motor parameters used in the BEMF observer. The errors were introduced manually during the motor operations. All tests were performed with different voltage feedbacks, as in the previous sections. The highest sensitivity was observed for λ_q polynomial coefficients er-

4 The current magnitude is computed as the squared root of the measured currents in the $\hat{d}\hat{q}$ reference frame, i.e. $\sqrt{\hat{i}_d^2 + \hat{i}_q^2}$

Table 4.3: Parameter sensitivity considerations of the sensorless drive

Sensitivity	R	λ_d	λ_q
load	low	null	very high
speed	medium	null	null

rors. In particular, the position error gets bigger as the load increases and this behaviour is repeated at all speeds. At low speed, sensorless operations are strongly affected by the voltage signals. It has been noted that resistance errors have consequences in this region of operations, although sensorless operations were not completely compromised. Far worst consequences come from the voltage signals used to fed the BEMF observer. The latter aspect has been already discussed in Sect. 4.4.1. It is interestingly to note that resistance error effects can be considered as equivalent voltage measurement errors [26].

4.4.5 *Future works*

The sensitivity analysis of the sensorless drive were only evaluated experimentally and with few tests. The analysis carried out in Sect. 4.3 shows how PMSM motor parameters knowledge are important not only for the performances, but for the stability of the BEMF observer itself. Future works will be oriented towards a mathematical analysis of the motor parameter and measurement sensitivity. The experimental evaluation of all the proposed controllers in Sect. 4.3 will be considered as well, for the final goal of defining a general PLL-based controller for both isotropic and anisotropic motors PM synchronous motors. Finally, a general framework to the experimental assessment of the sensorless algorithms will be considered.

5 CONCLUSIONS

The call for the reduction of energy consumption has manifolds reflections on the mechatronics applications. Electric motors represent one of the biggest electric energy consumers in the world, due to their wide utilisation both in industrial and domestic applications. There is, in turn, a need of more efficient drives that implement energy efficient control techniques for all kind of electric motors. Advanced control paradigms rely on mathematical model of the motor characterised by several parameters that have to be estimated. Therefore, a big effort is spent for the realisation of smart estimation techniques that can work even without the need of specific tests.

In this thesis work, all the aspects involving the development of an advance sensorless drive based on the BEMF estimation have been considered, discussed and experimentally evaluated. The research started with the definition of a new technique for the inverter non idealities compensation in Chapter 2, combined with a detailed analysis of the techniques presented so far in scientific literature. In the same frame, a new equipment to measure the voltage output of an inverter was designed and realised, too. The latter device is meant to be implemented in the next generation of electric drives, allowing the implementation of new techniques for both parameter estimation and control. It represents one of the most intriguing argument of this thesis, since the voltage measurement is one of the major bottleneck of the electric drives development. The proposed solutions is reliable, fast (since it is based on an FPGA) and quite cheap in drives already featuring FPGA on board.

The work presented in Chapter 3 regards the parameter estimation of all quantities involved in the mathematical model of the electric motor, whose basis are reported in Chapter 1. A polynomial approximation of the magnetic flux linkages has been presented and validated through experimental tests. The coefficients of the polynomial functions were retrieved by exploiting the informations in the MTPA operating conditions, merged with a simple LS algorithm. The use of such informations represents a novelty in the scientific research panorama and they do not require any specific test. The obtained flux linkages approximations allows to perform a fast and effective on-line estimation of the electromagnetic torque in an effective way. The same LS algorithm mentioned for the flux linkages approximation was used in an experiment to get the mechanical parameters as well. The latter ones were used to get a precise comparison of the es-

timated electromagnetic torque with the measured one, obtained by means of a torsiometer.

All the results obtained in Chapter 2 and 3 were used to developed a complete sensorless drive, from standstill up to the nominal speed, presented in Chapter 4. The initial position estimation problem, which is necessary in all sensorless techniques, was solved by developing a new technique based on the voltage measurement system presented in Chapter 2. The proposed procedure turned out to be effective for different PMSM motors of different levels of anisotropy, in particular the isotropic motor. The latter aspect represents quite an improvement compared with the available techniques. A BEMF based sensorless drive for medium/high speed applications was considered in this thesis, combined with a revised startup algorithm refined for the application to anisotropic motors. A detailed analysis of a *dq*-PLL for robust stability is presented, with different controller structures and for motors with anisotropy, too. Finally, the influence of motor parameter variations was investigated too. The results confirmed the validity of the proposed parameter estimation techniques as well as the need of precise parameters for the mathematical motor model implemented in the sensorless drive. The precision of the position estimate, and thus the efficiency of the motor, relies on the motor parameter accuracy. In fact, advance control techniques for the energy consumption reduction, such as the MTPA control, are based upon the precise knowledge of the rotor position.

The sensorless drive presented in this thesis can be implemented in many mechatronics applications, such as washing machines, dryers and so forth. All this applications require reliability and high efficiency, which can be both guaranteed by relying on a very precise position estimation strategy, without the need of additional mechanical sensors. Future activities will focus on the sensitivity analysis of position estimation algorithms with different motor observers to the motor parameters and measurements. Furthermore, the sensorless algorithms and the parameter estimation techniques developed in this thesis will be considered for other motor types, such as the synchronous reluctance motors.

Part III

APPENDIX

A

THE GOERTZEL ALGORITHM

At steady state, a frequency component of the current signal i is provided by the Goertzel algorithm, synchronised to the applied voltage signal. The Goertzel algorithm is a computationally-efficient discrete Fourier transformation that is particularly suitable for the on-line detection of one or few harmonics ([73], [53]). It is obtained from the normalised definition of the DFT, as detailed in [82]. For a given sample period T_c, a single-tone component at frequency f in the i current is detected by applying, in succession, a *IIR* and a *FIR* filter. In details, for each of the first $(N-1)$ sample times, the algorithm computes the intermediate IIR filter sequence

$$s(n) = i(n) + 2\cos(2\pi k/N)\, s(n-1) - s(n-2), \tag{A.1}$$

where $k = fNT_c$, $0 \leqslant n \leqslant (N-1)$ and N is the total number of samples per period of the input signal.

The phasor $\dot{I} = Ie^{j\varphi}$ of the current component (at frequency f) is computed in rectangular coordinates by applying the FIR filter to $s(N)$ and $s(N-1)$, that must be previously stored [82]:

$$\begin{aligned} I\cos(\varphi) &= s(N) - \cos(2\pi k/N)\, s(N-1) \\ I\sin(\varphi) &= -\sin(2\pi k/N)\, s(N-1). \end{aligned} \tag{A.2}$$

The described algorithm is resumed in Figure A.1.

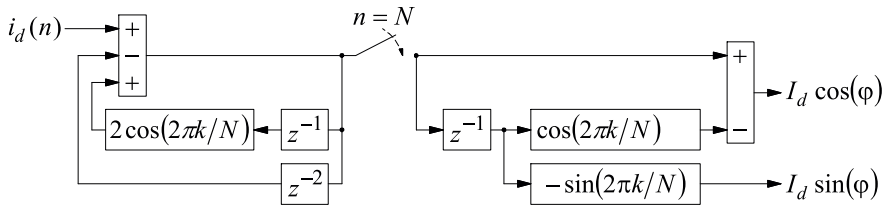

Figure A.1: Goertzel detection of current harmonic at frequency $f = k/NT_c$.

Altogether, the Goertzel algorithm yields a net computational saving, when compared to the conventional DFT [73]. However, the real advantage of the Goertzel algorithm for single harmonic analysis resides in its recursive definition (A.1). The required $N+2$ multiplications and $2N+1$ additions are spread over the whole NT_c time window, and $s(n)$ is updated with only one multiplication and two additions for each sample period. Moreover, the value of N can be increased as needed with no effect on the computational time requirements, obtaining a very high DFT selectivity [82].

B

MTPA CURVES OF THE MOTOR UNDER TEST

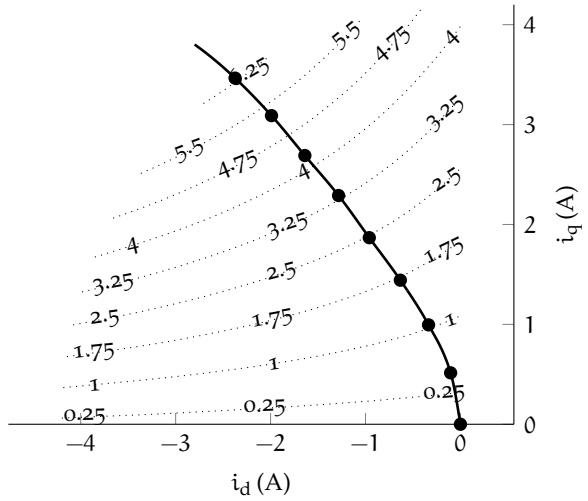

(a) Cartesian coordinates

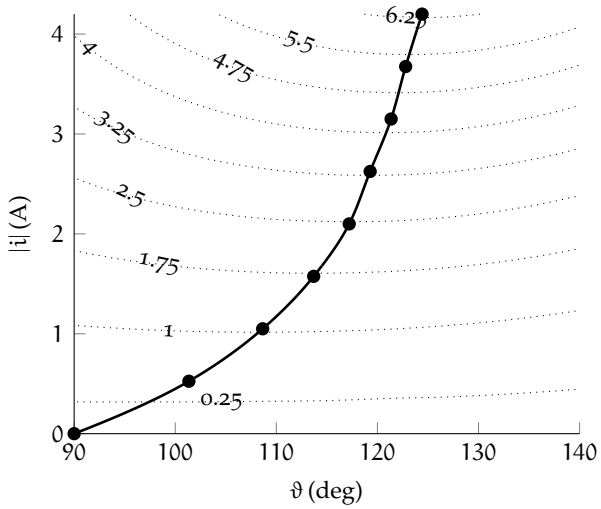

(b) Polar coordinates

Figure B.1: Experimental MTPA curve in Cartesian and polar coordinates.

The MTPA curve for the motor under test was measured with two different methods. The first one is based on the actual measurement on a laboratory test rig of the curve, as mentioned in Sect. 1.3.4.

BIBLIOGRAPHY

[1] Daniel Abramovitch. "Phase-locked loops: a control centric tutorial." In: *American Control Conference, 2002. Proceedings of the 2002*. Vol. 1. 2002, 1–15 vol.1. DOI: 10.1109/ACC.2002.1024769.

[2] P.P. Acarnley and J.F. Watson. "Review of position-sensorless operation of brushless permanent-magnet machines." In: *Industrial Electronics, IEEE Transactions on* 53.2 (Apr. 2006), 352-362. ISSN: 0278-0046. DOI: 10.1109/TIE.2006.870868.

[3] R. Antonello et al. "Maximum-Torque-Per-Ampere Operation of Anisotropic Synchronous Permanent-Magnet Motors Based on Extremum Seeking Control." In: *Industrial Electronics, IEEE Transactions on* 61.9 (Sept. 2014), pp. 5086–5093. ISSN: 0278-0046. DOI: 10.1109/TIE.2013.2278518.

[4] R. Antonello et al. "Benefits of Direct Phase Voltage Measurement in the Rotor Initial Position Detection for Permanent-Magnet Motor Drives." In: *Industrial Electronics, IEEE Transactions on* 62.11 (Nov. 2015), pp. 6719–6726. ISSN: 0278-0046. DOI: 10.1109/TIE.2015.2448514.

[5] E. Armando et al. "Accurate Modeling and Performance Analysis of IPM-PMASR Motors." In: *Industry Applications, IEEE Transactions on* 45.1 (Jan. 2009), pp. 123–130. ISSN: 0093-9994. DOI: 10.1109/TIA.2008.2009493.

[6] E. Armando et al. "Experimental Identification of the Magnetic Model of Synchronous Machines." In: *Industry Applications, IEEE Transactions on* 49.5 (Sept. 2013), 2116-2125. ISSN: 0093-9994. DOI: 10.1109/TIA.2013.2258876.

[7] M. Barcaro et al. "Remarks on Torque Estimation Accuracy in Fractional-Slot Permanent-Magnet Motors." In: *Industrial Electronics, IEEE Transactions on* 59.6 (2012), pp. 2565–2572. ISSN: 0278-0046. DOI: 10.1109/TIE.2011.2160517.

[8] T.D. Batzel and Mihai Comanescu. "Instantaneous voltage measurement in PWM voltage source inverters." In: *Electrical Machines and Power Electronics, 2007. ACEMP '07. International Aegean Conference on*. Sept. 2007, pp. 168–173. DOI: 10.1109/ACEMP.2007.4510497.

[9] N. Bedetti et al. "Self-Commissioning of Inverter Dead-Time Compensation by Multiple Linear Regression Based on a Physical Model." In: *Industry Applications, IEEE Transactions on* 51.5 (Sept. 2015), pp. 3954–3964. ISSN: 0093-9994. DOI: 10.1109/TIA.2015.2436882.

[10] L. Ben-Brahim. "On the compensation of dead time and zero-current crossing for a PWM-inverter-controlled AC servo drive." In: *Industrial Electronics, IEEE Transactions on* 51.5 (Oct. 2004), 1113-1118. ISSN: 0278-0046. DOI: 10.1109/TIE.2004.834940.

[11] M. Bertoluzzo et al. "Self-Commissioning of RFO IM Drives: One-test Identification of the Magnetization Characteristic of the Motor." In: *Industry Applications, IEEE Transactions on* 37.6 (Nov. 2001), pp. 1801–1806. ISSN: 0093-9994. DOI: 10.1109/28.968194.

[12] F. Betin et al. "Trends in Electrical Machines Control: Samples for Classical, Sensorless, and Fault-Tolerant Techniques." In: *Industrial Electronics Magazine, IEEE* 8.2 (June 2014), pp. 43–55. ISSN: 1932-4529. DOI: 10.1109/MIE.2014.2313752.

[13] N. Bianchi. *Electrical Machine Analysis Using Finite Elements*. CRC Press, June 2005. ISBN: 9780849333996.

[14] N. Bianchi. "Synchronous reluctance and interior permanent magnet motors." In: *Electrical Machines Design Control and Diagnosis (WEMDCD), 2013 IEEE Workshop on*. Mar. 2013, pp. 75–84. DOI: 10.1109/WEMDCD.2013.6525167.

[15] N. Bianchi and S. Bolognani. "Influence of Rotor Geometry of an IPM Motor on Sensorless Control Feasibility." In: *Industry Applications, IEEE Transactions on* 43.1 (Jan. 2007), pp. 87–96. ISSN: 0093-9994. DOI: 10.1109/TIA.2006.887317.

[16] N. Bianchi and S. Bolognani. "Sensorless-Oriented Design of PM Motors." In: 45.4 (July 2009), pp. 1249–1257. ISSN: 0093-9994. DOI: 10.1109/TIA.2009.2023387.

[17] N. Bianchi and T.M. Jahns. *Design, Analysis, and Control of Interior PM Synchronous Machines: Tutorial Course Notes ;* Seattle: CLEUP, Oct. 2004. ISBN: 9788871788982.

[18] N. Bianchi et al. "Comparison of PM Motor Structures and Sensorless Control Techniques for Zero-Speed Rotor Position Detection." In: 22.6 (Nov. 2007), pp. 2466–2475. ISSN: 0885-8993. DOI: 10.1109/TPEL.2007.904238.

[19] N. Bianchi et al. "Effect of Stator and Rotor Saturation on Sensorless Rotor Position Detection." In: 49.3 (May 2013), 1333-1342. ISSN: 0093-9994. DOI: 10.1109/TIA.2013.2253437.

[20] R. Bojoi et al. "Sensorless control of PM motor drives - A technology status review." In: *Electrical Machines Design Control and Diagnosis (WEMDCD), 2013 IEEE Workshop on*. Mar. 2013, pp. 168–182. DOI: 10.1109/WEMDCD.2013.6525177.

[21] R. Bojoi et al. "Methodology for the IPM motor magnetic model computation based on finite element analysis." In: *Industrial Electronics Society, IECON 2014 - 40th Annual Conference of the IEEE*. Oct. 2014, pp. 722–728. DOI: 10.1109/IECON.2014.7048580.

[22] S. Bolognani and M. Zigliotto. "Self-commissioning compensation of inverter non-idealities for sensorless AC drives applications." In: *Power Electronics, Machines and Drives, 2002. International Conference on (Conf. Publ. No. 487)*. June 2002, pp. 30–37. DOI: 10.1049/cp:20020085.

[23] S. Bolognani et al. "Sensorless full-digital PMSM drive with EKF estimation of speed and rotor position." In: *Industrial Electronics, IEEE Transactions on* 46.1 (Feb. 1999), pp. 184–191. ISSN: 0278-0046. DOI: 10.1109/41.744410.

[24] S. Bolognani et al. "Repetitive-Control-Based Self-Commissioning Procedure for Inverter Nonidealities Compensation." In: *Industry Application, IEEE Transactions on* 44.5 (Sept. 2008), 1587-1596. ISSN: 0093-9994. DOI: 10.1109/TIA.2008.2002280.

[25] S. Bolognani et al. "Automatic Tracking of MTPA Trajectory in IPM Motor Drives Based on AC Current Injection." In: *Industry Applications, IEEE Transactions on* 47.1 (Jan. 2011), pp. 105–114. ISSN: 0093-9994. DOI: 10.1109/TIA.2010.2090842.

[26] S. Bolognani et al. "Design Issues and Estimation Errors Analysis of Back-EMF-Based Position and Speed Observer for SPM Synchronous Motors." In: *Emerging and Selected Topics in Power Electronics, IEEE Journal of* 2.2 (June 2014), pp. 159–170. ISSN: 2168-6777. DOI: 10.1109/JESTPE.2013.2296974.

[27] M. Boussak. "Implementation and experimental investigation of sensorless speed control with initial rotor position estimation for interior permanent magnet synchronous motor drive." In: 20.6 (Nov. 2005), pp. 1413–1422. ISSN: 0885-8993. DOI: 10.1109/TPEL.2005.854014.

[28] F. Briz and M.W. Degner. "Rotor Position Estimation." In: *Industrial Electronics Magazine, IEEE* 5.2 (June 2011), pp. 24–36. ISSN: 1932-4529. DOI: 10.1109/MIE.2011.941118.

[29] R.P. Burgos et al. "Design and Evaluation of a PLL-Based Position Controller for Sensorless Vector Control of Permanent-Magnet Synchronous Machines." In: *IEEE Industrial Electronics, IECON 2006 - 32nd Annual Conference on*. Nov. 2006, pp. 5081–5086. DOI: 10.1109/IECON.2006.347863.

[30] Simone Buso and Paolo Mattavelli. *Digital Control in Power Electronics*. Vol. 1. United States: Morgan&Claypool Publishers, 2006.

[31] M. Carraro and M. Zigliotto. "Automatic Parameter Identification of Inverter-Fed Induction Motors at Standstill." In: *Industrial Electronics, IEEE Transactions on* 61.9 (Sept. 2014), pp. 4605–4613. ISSN: 0278-0046. DOI: 10.1109/TIE.2013.2289903.

[32] M. Carraro et al. "A novel approach to torque estimation in IPM synchronous motor drives." In: *IECON 2012 - 38th Annual Conference on IEEE Industrial Electronics Society*. Oct. 2012, pp. 4637–4641. DOI: 10.1109/IECON.2012.6389499.

[33] M. Carraro et al. "Estimation of the direct-axis inductance in PM synchronous motor drives at standstill." In: *Industrial Technology (ICIT), 2013 IEEE International Conference on*. Feb. 2013, pp. 313–318. DOI: 10.1109/ICIT.2013.6505691.

[34] Song Chi et al. "Sliding-Mode Sensorless Control of Direct-Drive PM Synchronous Motors for Washing Machine Applications." In: *Industry Applications, IEEE Transactions on* 45.2 (Mar. 2009), pp. 582–590. ISSN: 0093-9994. DOI: 10.1109/TIA.2009.2013545.

[35] T.-H. Chin et al. "Accurate measurement of instantaneous values of voltage, current and power for power electronics circuits." In: *Power Electronics Specialists Conference, 1998. PESC 98 Record. 29th Annual IEEE*. Vol. 1. May 1998, 302–307 vol.1. DOI: 10.1109/PESC.1998.701915.

[36] Jong-Woo Choi and Seung-Ki Sul. "Inverter output voltage synthesis using novel dead time compensation." In: *Power Electronics, IEEE Transactions on* 11.2 (Mar. 1996), pp. 221–227. ISSN: 0885-8993. DOI: 10.1109/63.486169.

[37] A Cichowski and J. Nieznanski. "Self-tuning dead-time compensation method for voltage-source inverters." In: *Power Electronics, IEEE Transactions on* 3.2 (June 2005), pp. 72–75. ISSN: 1540-7985. DOI: 10.1109/LPEL.2005.851310.

[38] A. Consoli et al. "Range extended efficiency optimization technique for scalar IPMSM drives." In: *Power Electronics and Motion Control Conference (EPE/PEMC), 2010 14th International*. Sept. 2010, DOI: 10.1109/EPEPEMC.2010.5606644.

[39] D. G. Dorrell et al. "Analysis and Design Techniques Applied to Hybrid Vehicle Drive Machines- Assessment of Alternative IPM and Induction Motor Topologies." In: *Industrial Electronics, IEEE Transactions on* 59.10 (Oct. 2012), pp. 3690–3699. ISSN: 0278-0046. DOI: 10.1109/TIE.2011.2165460.

[40] W.C. Duesterhoeft et al. "Determination of Instantaneous Currents and Voltages by Means of Alpha, Beta, and Zero Components." In: *American Institute of Electrical Engineers, Transactions of the* 70.2 (July 1951), pp. 1248–1255. ISSN: 0096-3860. DOI: 10.1109/T-AIEE.1951.5060554.

[41] A. E. Fitzgerald et al. *Electric Machinery 6th edition*. The McGraw-Hill Companies, Inc., 1221 Avenue of the Americas, New York, NY 10020.: McGraw-Hill, 2003. ISBN: 0-07-366009-4.

[42] G.F. Franklin et al. *Feedback Control of Dynamic Systems*. 4th. Upper Saddle River, New Jersey 07458: Prentice Hall, 2002.

[43] C. French and P. Acarnley. "Control of permanent magnet motor drives using a new position estimation technique." In: *Industry Applications, IEEE Transactions on* 32.5 (Sept. 1996), 1089-1097. ISSN: 0093-9994. DOI: 10.1109/28.536870.

[44] F. Genduso et al. "Back EMF Sensorless-Control Algorithm for High-Dynamic Performance PMSM." In: *Industrial Electronics, IEEE Transactions on* 57.6 (June 2010), pp. 2092–2100. ISSN: 0278-0046. DOI: 10.1109/TIE.2009.2034182.

[45] J.M. Guerrero et al. "Inverter nonlinearity effects in high-frequency signal-injection-based sensorless control methods." In: *Industry Application, IEEE Transactions on* 41.2 (Mar. 2005), pp. 618–626. ISSN: 0093-9994. DOI: 10.1109/TIA.2005.844411.

[46] P. Guglielmi et al. "Cross-Saturation Effects in IPM Motors and Related Impact on Sensorless Control." In: *Industry Applications, IEEE Transactions on* 42.6 (Nov. 2006), pp. 1516–1522. ISSN: 0093-9994. DOI: 10.1109/TIA.2006.882646.

[47] J. Holtz. "Acquisition of Position Error and Magnet Polarity for Sensorless Control of PM Synchronous Machines." In: 44.4 (July 2008), pp. 1172–1180. ISSN: 0093-9994. DOI: 10.1109/TIA.2008.921418.

[48] J. Holtz and Juntao Quan. "Sensorless vector control of induction motors at very low speed using a nonlinear inverter model and parameter identification." In: *Industry Applications, IEEE Transactions on* 38.4 (July 2002), pp. 1087–1095. ISSN: 0093-9994. DOI: 10.1109/TIA.2002.800779.

[49] A Imura et al. "Dead-time compensation in model predictive instantaneous-current control." In: *IECON 2012 - 38th Annual Conference on IEEE Industrial Electronics Society*. Oct. 2012, 5037-5042. DOI: 10.1109/IECON.2012.6388981.

[50] Y. Inoue et al. "Effectiveness of Voltage Error Compensation and Parameter Identification for Model-Based Sensorless Control of IPMSM." In: *Industry Applications, IEEE Transactions on* 45.1 (Jan. 2009), pp. 213–221. ISSN: 0093-9994. DOI: 10.1109/TIA.2008.2009617.

[51] Ji-Hoon Jang et al. "Sensorless drive of surface-mounted permanent-magnet motor by high-frequency signal injection based on magnetic saliency." In: *Industry Applications, IEEE Transactions on* 39.4 (July 2003), pp. 1031–1039. ISSN: 0093-9994. DOI: 10.1109/TIA.2003.813734.

[52] V. Kaura and V. Blasko. "Operation of a phase locked loop system under distorted utility conditions." In: *Industry Applications, IEEE Transactions on* 33.1 (Jan. 1997), pp. 58–63. ISSN: 0093-9994. DOI: 10.1109/28.567077.

[53] R.J. Kerkman et al. "A frequency-based determination of transient inductance and rotor resistance for field commissioning purposes." In: *Industry Applications, IEEE Transactions on* 32.3 (May 1996), pp. 577–584. ISSN: 0093-9994. DOI: 10.1109/28.502169.

[54] Hyunbae Kim et al. "A novel method for initial rotor position estimation for IPM synchronous machine drives." In: 40.5 (Sept. 2004), pp. 1369–1378. ISSN: 0093-9994. DOI: 10.1109/TIA.2004.834091.

[55] Hyun-Soo Kim et al. "On-line dead-time compensation method based on time delay control." In: *Control Systems Technology, IEEE Transactions on* 11.2 (Mar. 2003), pp. 279–285. ISSN: 1063-6536. DOI: 10.1109/TCST.2003.809251.

[56] Hyun-Soo Kim et al. "On-line dead-time compensation method using disturbance observer." In: *Power Electronics, IEEE Transactions on* 18.6 (Nov. 2003), pp. 1336–1345. ISSN: 0885-8993. DOI: 10.1109/TPEL.2003.818833.

[57] Sungmin Kim et al. "Maximum Torque per Ampere (MTPA) Control of an IPM Machine Based on Signal Injection Considering Inductance Saturation." In: *Power Electronics, IEEE Transactions on* 28.1 (Jan. 2013), pp. 488–497. ISSN: 0885-8993. DOI: 10.1109/TPEL.2012.2195203.

[58] R. Leidhold. "Position Sensorless Control of PM Synchronous Motors Based on Zero-Sequence Carrier Injection." In: 58.12 (Dec. 2011), pp. 5371–5379. ISSN: 0278-0046. DOI: 10.1109/TIE.2011.2112323.

[59] Werner Leonhard. *Control of Electrical Drives 3rd edition*. Berlin; Heidelberg; New York; Barcelona; Hong Kong; London; Milan; Paris; Singapore; Tokyo: Springer-Verlag, 2001. ISBN: 3-540-41820-2.

[60] N. Limsuwan et al. "Design and evaluation of a variable-flux flux-intensifying interior permanent magnet machine." In: *ECCE, 2012 IEEE*. 2012, pp. 3670–3677. DOI: 10.1109/ECCE.2012.6342480.

[61] Kan Liu and Z.Q. Zhu. "Online Estimation of the Rotor Flux Linkage and Voltage-Source Inverter Nonlinearity in Permanent Magnet Synchronous Machine Drives." In: *Power Electronics, IEEE Transactions on* 29.1 (Jan. 2014), pp. 418–427. ISSN: 0885-8993. DOI: 10.1109/TPEL.2013.2252024.

[62] Kan Liu and Z.Q. Zhu. "Mechanical Parameter Estimation of Permanent-Magnet Synchronous Machines With Aiding From Estimation of Rotor PM Flux Linkage." In: *Industry Applications, IEEE Transactions on* 51.4 (July 2015), pp. 3115–3125. ISSN: 0093-9994. DOI: 10.1109/TIA.2015.2399615.

[63] Kan Liu et al. "Influence of Nonideal Voltage Measurement on Parameter Estimation in Permanent-Magnet Synchronous Machines." In: 59.6 (June 2012), pp. 2438–2447. ISSN: 0278-0046. DOI: 10.1109/TIE.2011.2162214.

[64] Mengesha Mamo et al. "Novel rotor position extraction based on carrier frequency component method (CFCM) using two reference frames for IPM drives." In: 52.2 (Apr. 2005), pp. 508–514. ISSN: 0278-0046. DOI: 10.1109/TIE.2005.844234.

[65] D. C. Meeker. *Finite Element Method Magnetics*. URL: http://www.femm.info.

[66] Y.A.-R.I. Mohamed and T.K. Lee. "Adaptive self-tuning MTPA vector controller for IPMSM drive system." In: *Energy Conversion, IEEE Transactions on* 21.3 (Sept. 2006), pp. 636–644. ISSN: 0885-8969. DOI: 10.1109/TEC.2006.878243.

[67] S. Morimoto et al. "Loss minimization control of permanent magnet synchronous motor drives." In: *Industrial Electronics, IEEE Transactions on* 41.5 (Oct. 1994), pp. 511–517. ISSN: 0278-0046. DOI: 10.1109/41.315269.

[68] S. Morimoto et al. "Sensorless control strategy for salient-pole PMSM based on extended EMF in rotating reference frame." In: *Industry Applications, IEEE Transactions on* 38.4 (July 2002), pp. 1054–1061. ISSN: 0093-9994. DOI: 10.1109/TIA.2002.800777.

[69] AR. Munoz and T.A Lipo. "On-line dead-time compensation technique for open-loop PWM-VSI drives." In: *Power Electronics, IEEE Transactions on* 14.4 (July 1999), pp. 683–689. ISSN: 0885-8993. DOI: 10.1109/63.774205.

[70] G. El-Murr et al. "Online cross-coupling and self incremental inductances determination of salient Permanent Magnet Synchronous Machines." In: *Power Electronics, Machines and Drives (PEMD 2010), 5th IET International Conference on*. Apr. 2010, pp. 1–4. DOI: 10.1049/cp.2010.0111.

[71] B. Nahid-Mobarakeh et al. "Mechanical sensorless control of PMSM with online estimation of stator resistance." In: *Industry Applications, IEEE Transactions on* 40.2 (Mar. 2004), pp. 457–471. ISSN: 0093-9994. DOI: 10.1109/TIA.2004.824490.

[72] S.A. Odhano et al. "Identification of the Magnetic Model of Permanent-Magnet Synchronous Machines Using DC-Biased Low-Frequency AC Signal Injection." In: *Industry Applications, IEEE Transactions on* 51.4 (July 2015), pp. 3208–3215. ISSN: 0093-9994. DOI: 10.1109/TIA.2015.2413383.

[73] A. V. Oppenheim and R. W. Schafer. *Discrete-Time Signal Processing, Third Edition*. Upper Saddle River, NJ, USA: Prentice-Hall, Inc., 2009.

[74] S. Ostlund and M. Brokemper. "Sensorless rotor-position detection from zero to rated speed for an integrated PM synchronous motor drive." In: *Industry Applications, IEEE Transactions on* 32.5 (1996), pp. 1158–1165. ISSN: 0093-9994. DOI: 10.1109/28.536878.

[75] F. Parasiliti et al. "Sensorless speed control of a PM synchronous motor based on sliding mode observer and extended Kalman filter." In: *Industry Applications Conference, 2001. Thirty-Sixth IAS Annual Meeting. Conference Record of the 2001 IEEE*. Vol. 1. Sept. 2001, 533–540 vol.1. DOI: 10.1109/IAS.2001.955472.

[76] Dong-Min Park and Kyeong-Hwa Kim. "Parameter-Independent Online Compensation Scheme for Dead Time and Inverter Nonlinearity in IPMSM Drive Through Waveform Analysis." In: *Industrial Electronics, IEEE Transactions on* 61.2 (Feb. 2014), 701-707. ISSN: 0278-0046. DOI: 10.1109/TIE.2013.2251737.

[77] Yongsoon Park and Seung-Ki Sul. "A Novel Method Utilizing Trapezoidal Voltage to Compensate for Inverter Nonlinearity." In: *Power Electronics, IEEE Transactions on* 27.12 (Dec. 2012), pp. 4837–4846. ISSN: 0885-8993. DOI: 10.1109/TPEL.2012.2192451.

[78] G. Pellegrino et al. "Accurate Inverter Error Compensation and Related Self-Commissioning Scheme in Sensorless Induction Motor Drives." In: *Industry Applications, IEEE Transactions on* 46.5 (Sept. 2010), pp. 1970–1978. ISSN: 0093-9994. DOI: 10.1109/TIA.2010.2057395.

[79] G. Pellegrino et al. "Magnetic Model Self-Identification for PM Synchronous Machine Drives." In: *Industry Applications, IEEE Transactions on* 51.3 (May 2015), pp. 2246–2254. ISSN: 0093-9994. DOI: 10.1109/TIA.2014.2365627.

[80] P.D.C. Perera et al. "A sensorless, stable V/f control method for permanent-magnet synchronous motor drives." In: *Industry Applications, IEEE Transactions on* 39.3 (May 2003), pp. 783–791. ISSN: 0093-9994. DOI: 10.1109/TIA.2003.810624.

[81] L. Peretti and M. Zigliotto. "FPGA-based voltage measurements in AC drives." In: *Electrical Machines (ICEM), 2010 XIX International Conference on*. Sept. 2010, pp. 1–6. DOI: 10.1109/ICELMACH.2010.5608153.

[82] L. Peretti and M. Zigliotto. "Automatic procedure for induction motor parameter estimation at standstill." In: *Electric Power Applications, IET* 6.4 (Apr. 2012), 214-224. ISSN: 1751-8660. DOI: 10.1049/iet-epa.2010.0262.

[83] L. Peretti et al. "Self-commissioning of flux linkage curves of synchronous reluctance machines in quasi-standstill condition." In: *Electric Power Applications, IET* 9.9 (2015), pp. 642–651. ISSN: 1751-8660. DOI: 10.1049/iet-epa.2015.0070.

[84] K.M. Rahman and S. Hiti. "Identification of machine parameters of a synchronous motor." In: *Industry Applications, IEEE Transactions on* 41.2 (Mar. 2005), pp. 557–565. ISSN: 0093-9994. DOI: 10.1109/TIA.2005.844379.

[85] M.A. Rahman. "Recent Advances of IPM Motor Drives in Power Electronics World." In: *Power Electronics and Drives Systems, 2005. PEDS 2005. International Conference on*. Vol. 1. -0 2005, pp. 24–31. DOI: 10.1109/PEDS.2005.1619655.

[86] M. Rashed et al. "Sensorless Indirect-Rotor-Field-Orientation Speed Control of a Permanent-Magnet Synchronous Motor With Stator-Resistance Estimation." In: *Industrial Electronics, IEEE Transactions on* 54.3 (June 2007), pp. 1664–1675. ISSN: 0278-0046. DOI: 10.1109/TIE.2007.895136.

[87] R. Raute et al. "Analysis and Compensation of Inverter Nonlinearity Effect on a Sensorless PMSM Drive at Very Low and Zero Speed Operation." In: 57.12 (Dec. 2010), pp. 4065–4074. ISSN: 0278-0046. DOI: 10.1109/TIE.2010.2044116.

[88] D.D. Reigosa et al. "Measurement and Adaptive Decoupling of Cross-Saturation Effects and Secondary Saliencies in Sensorless Controlled IPM Synchronous Machines." In: *Industry Applications, IEEE Transactions on* 44.6 (Nov. 2008), pp. 1758–1767. ISSN: 0093-9994. DOI: 10.1109/TIA.2008.2006335.

[89] M. Ruff and H. Grotstollen. "Identification of the Saturated Mutual Inductance of an Asynchronous Motor at Standstill by Recursive Least Squares Algorithm." In: *Power Electronics and Applications, 1993., Fifth European Conference on*. Sept. 1993, 103–108 vol.5.

[90] G. Scarcella et al. "High performance sensorless controls based on HF excitation: A viable solution for future AC motor drives?" In: *(WEMDCD), 2015*. Mar. 2015, pp. 178–187. DOI: 10.1109/WEMDCD.2015.7194527.

[91] P.B. Schmidt et al. "Initial rotor angle detection of a nonsalient pole permanent magnet synchronous machine." In: *Industry Applications Conference, 1997. Thirty-Second IAS Annual Meeting, IAS '97., Conference Record of the 1997 IEEE*. Vol. 1. Oct. 1997, 459–463 vol.1. DOI: 10.1109/IAS.1997.643063.

[92] M. Schroeder. "Synthesis of low-peak-factor signals and binary sequences with low autocorrelation (Corresp.)" In: *Information Theory, IEEE Transactions on* 16.1 (Jan. 1970), pp. 85–89. ISSN: 0018-9448. DOI: 10.1109/TIT.1970.1054411.

[93] R.B. Sepe and Jeffrey H. Lang. "Real-time observer-based (adaptive) control of a permanent-magnet synchronous motor without mechanical sensors." In: *Industry Applications, IEEE Transactions on* 28.6 (Nov. 1992), pp. 1345–1352. ISSN: 0093-9994. DOI: 10.1109/28.175287.

[94] Jorge Solsona et al. "Nonlinear control of a permanent magnet synchronous motor with disturbance torque estimation." In: *Energy Conversion, IEEE Transactions on* 15.2 (June 2000), pp. 163–168. ISSN: 0885-8969. DOI: 10.1109/60.866994.

[95] Y.-C. Son et al. "Sensorless operation of permanent magnet motor using direct voltage sensing circuit." In: *Industry Applications Conference, 2002. 37th IAS Annual Meeting. Conference Record of the*. Vol. 3. Oct. 2002, 1674–1678 vol.3. DOI: 10.1109/IAS.2002.1043759.

[96] B. Stumberger et al. "Evaluation of saturation and cross-magnetization effects in interior permanent-magnet synchronous motor." In: *Industry Applications, IEEE Transactions on* 39.5 (Sept. 2003), 1264-1271. ISSN: 0093-9994. DOI: 10.1109/TIA.2003.816538.

[97] Tianfu Sun et al. "Maximum Torque Per Ampere (MTPA) Control for Interior Permanent Magnet Synchronous Machine Drives Based on Virtual Signal Injection." In: *Power Electronics, IEEE Transactions on* 30.9 (Sept. 2015), pp. 5036–5045. ISSN: 0885-8993. DOI: 10.1109/TPEL.2014.2365814.

[98] M. Tursini et al. "Initial rotor position estimation method for PM motors." In: 39.6 (Nov. 2003), pp. 1630–1640. ISSN: 0093-9994. DOI: 10.1109/TIA.2003.818977.

[99] N. Urasaki et al. "An accurate modeling for permanent magnet synchronous motor drives." In: *Applied Power Electronics Conference and Exposition, 2000. APEC 2000. Fifteenth Annual IEEE*. Vol. 1. 2000, 387–392 vol.1. DOI: 10.1109/APEC.2000.826132.

[100] N. Urasaki et al. "A novel calculation method for iron loss resistance suitable in modeling permanent-magnet synchronous motors." In: *Energy Conversion, IEEE Transactions on* 18.1 (Mar. 2003), pp. 41–47. ISSN: 0885-8969. DOI: 10.1109/TEC.2002.808329.

[101] N. Urasaki et al. "Relationship of parallel model and series model for permanent magnet synchronous motors taking iron loss into account." In: *Energy Conversion, IEEE Transactions on* 19.2 (June 2004), pp. 265–270. ISSN: 0885-8969. DOI: 10.1109/TEC.2004.827291.

[102] N. Urasaki et al. "Adaptive Dead-Time Compensation Strategy for Permanent Magnet Synchronous Motor Drive." In: *Energy Conversion, IEEE Transactions on* 22.2 (June 2007), pp. 271–280. ISSN: 0885-8969. DOI: 10.1109/TEC.2006.875469.

[103] T.L. Vandoorn et al. "Generation of Multisinusoidal Test Signals for the Identification of Synchronous-Machine Parameters by Using a Voltage-Source Inverter." In: *Industrial Electronics, IEEE Transactions on* 57.1 (Jan. 2010), pp. 430–439. ISSN: 0278-0046. DOI: 10.1109/TIE.2009.2031135.

[104] Gaolin Wang et al. "Self-Commissioning of Permanent Magnet Synchronous Machine Drives at Standstill Considering Inverter Nonlinearities." In: *Power Electronics, IEEE Transactions on* 29.12 (Dec. 2014), 6615-6627. ISSN: 0885-8993. DOI: 10.1109/TPEL.2014.2306734.

[105] G. Wang et al. "Self-Commissioning of Permanent Magnet Synchronous Machine Drives at Standstill Considering Inverter Nonlinearities." In: *Power Electronics, IEEE Transactions on* 29.12 (Dec. 2014), pp. 6615–6627. ISSN: 0885-8993. DOI: 10.1109/TPEL.2014.2306734.

[106] Zihui Wang et al. "A Simple Startup Strategy Based on Current Regulation for Back-EMF-Based Sensorless Control of PMSM." In: *Power Electronics, IEEE Transactions on* 27.8 (Aug. 2012), pp. 3817–3825. ISSN: 0885-8993. DOI: 10.1109/TPEL.2012.2186464.

[107] A.R. Weber and G. Steiner. "An accurate identification and compensation method for nonlinear inverter characteristics for ac motor drives." In: *Instrumentation and Measurement Technology Conference (I2MTC), 2012 IEEE International*. May 2012, 821-826. DOI: 10.1109/I2MTC.2012.6229666.

[108] B.A Welchko et al. "Effects and Compensation of Dead-Time and Minimum Pulse-Width Limitations in Two-Level PWM Voltage Source Inverters." In: *Industry Applications Conference, 2006. 41st IAS Annual Meeting. Conference Record of the 2006 IEEE*. Vol. 2. Oct. 2006, pp. 889–896. DOI: 10.1109/IAS.2006.256630.

[109] C. Winterhalter et al. "The effect of circuit parasitic impedance on the performance of IGBTs in voltage source inverters." In: *Applied Power Electronics Conference and Exposition, 2001. APEC 2001. Sixteenth Annual IEEE*. Vol. 2. 2001, 995–1001 vol.2. DOI: 10.1109/APEC.2001.912488.

[110] Ge Xie et al. "Permanent Magnet Flux Online Estimation Based on Zero-Voltage Vector Injection Method." In: *Power Electronics, IEEE Transactions on* 30.12 (Dec. 2015), pp. 6506–6509. ISSN: 0885-8993. DOI: 10.1109/TPEL.2015.2439718.

[111] Wei Xu and R.D. Lorenz. "High-Frequency Injection-Based Stator Flux Linkage and Torque Estimation for DB-DTFC Implementation on IPMSMs Considering Cross-Saturation Effects." In: *Industry Applications, IEEE Transactions on* 50.6 (Nov. 2014), 3805-3815. ISSN: 0093-9994. DOI: 10.1109/TIA.2014.2322134.

[112] G. Zanuso et al. "Stator reference frame approach for DC injection-based stator resistance estimation in electric drives." In: *Power Electronics and Drive Systems (PEDS), 2015 IEEE 11th International Conference on*. June 2015, pp. 867–872. DOI: 10.1109/PEDS.2015.7203391.

[113] X. Zhang and Z. Li. "Sliding Mode Observer-Based Mechanical Parameter Estimation for Permanent-Magnet Synchronous Motor." In: *Power Electronics, IEEE Transactions on* PP.99 (2015), pp. 1–1. ISSN: 0885-8993. DOI: 10.1109/TPEL.2015.2495183.

[114] Hengbing Zhao et al. "An accurate approach of nonlinearity compensation for VSI inverter output voltage." In: *Power Electronics, IEEE Transactions on* 19.4 (July 2004), pp. 1029–1035. ISSN: 0885-8993. DOI: 10.1109/TPEL.2004.830072.

[115] Guchuan Zhu et al. "A nonlinear state observer for the sensorless control of a permanent-magnet AC machine." In: *Industrial Electronics, IEEE Transactions on* 48.6 (Dec. 2001), pp. 1098–1108. ISSN: 0278-0046. DOI: 10.1109/41.969388.